MASSEY UNIVERSITY

DOCTOR OF PHILOSOPHY IN PHYSICS

Biophysical investigations of cells focusing on the utility of Optical Tweezers

---

Author:
Susav Pradhan

Supervisor:
Prof. Martin Williams

Co-supervisor:
A/Prof. Catherine Whitby

A thesis presented in partial fulfillment of the requirements for the degree of Doctor of Philosophy in Physics

at

Biophysics and Soft Matter Group
School of Fundamental Science

PhD Duration : 2017 - 2021

Declaration of Authorship

I, Susav Pradhan, declare that this thesis titled, “Biophysical investigations of cells focusing on the utility of Optical Tweezers” and the work presented in it are my own. I confirm that:

- This work was done wholly or mainly in candidature for a research degree at this University.
- Where any part of this thesis has previously been submitted for a degree or any other qualification at this University or any other institution, this has been clearly stated.
- Where I have consulted the published work of others, this is always clearly attributed.
- Where I have quoted from the work of others, the source is always given. Except for such quotations, this thesis is entirely my own work.
- I have acknowledged all main sources of help.
- Where the thesis is based on work done by myself jointly with others, I have made clear exactly what was done by others and what I have contributed myself.

Signed:

Date:

Abstract

The aim of this thesis was to explore the utility of different biophysical techniques, particularly optical tweezers (OT), in the investigation of the mechanical properties and interactions of biological samples. Specifically, MCF7 cells and their extracted nuclei were investigated mechanically, while the adhesion property of selected bacteria to the milk fat globule was also used as an exemplar. Biological cells have the ability to actively respond to external mechanical forces exerted by the microenvironment. The cellular response can be viscous, elastic, or viscoelastic in nature depending on the nature of the applied forces and the mechanical stresses applied. Changes in the mechanical properties of cells and nuclei have emerged as a prominent hallmark of many human diseases, particularly in neurodegenerative and metastatic diseases.

In this thesis, to understand the application of these techniques to biological systems better, bulk rheology and microrheology studies were first performed on a model viscoelatic fluid (PEO). Particularly, the passive and active microrheology of this model viscoelastic material was characterized using optical tweezers and video particle tracking to develop the prerequisite experimental and analytical methods.

Using the experimental knowledge gained from applying optical tweezers to standard materials, a mechanistic approach was developed in order to better understand how the mechanical properties of MCF7 cells change when the amount of heterochromatin protein (HP1α) present inside the nuclei was reduced. (HP1α) is an architectural protein that establishes and maintains heterochromatin, ensuring genome fidelity and nuclear integrity. While the mechanical effects of changes in the relative amount of euchromatin and heterochromatin brought about by inhibiting chromatin modifying enzymes have been studied previously, here we measure how the material properties of the cells are modified following the knockdown HP1α. Indentation experiments using optical tweezers revealed that the knockdown cells have apparent Young's modului significantly lower than control cells. Similarly, tether experiments performed using optical tweezers revealed that the membrane tensions of knockdown cells were lower than those of control cells. This assay led to further work on studying the mechanical properties of nuclei extracted from MCF7 cells.

A combination of atomic force microscopy, optical tweezers, and techniques based on micropipette aspiration was used to characterize the mechanical properties of nuclei extracted from HP1α knockdown or matched control cells. Similar to the previous finding on cells, local indentation performed using atomic force microscopy and optical tweezers found that the knockdown nuclei have apparent Young's modului significantly lower than control nuclei. In contrast, results from pipette-based techniques in the spirit of microaspiration, where the whole nuclei were deformed and aspirated into a conical pipette, showed considerably less variation between HP1α knockdown and control, consistent with previous studies reporting that it is predominantly the lamins in the nuclear envelope that determine the mechanical response to large whole-cell deformations. The differences in chromatin organisation observed by various microscopy techniques between the MCF7 control and HP1α knock-down nuclei correlated well with the results of our measured mechanical responses and our hypotheses regarding their origin.

Finally, not just the mechanical properties of the cells but also their interactions (an interaction between the milk fat globule membrane and two bacterial strains - *Lactobacillius fermentum strains - 1487 and 1485*) was explored as a side project by probing with optical tweezers. The difference in bacterial cell surface properties of these two strains and its effects on intestinal epithelial barrier integrity has already been studied. This study focuses on measuring the adhesion force between membrane and bacteria using optical tweezers. The results suggested that L. fermentus AGR1487 strongly interacts with MFGM compared to AGR1485. All in all, this thesis demonstrates how biophysical techniques can provide valuable insights into understanding biological systems.

Acknowledgements

First of all, I would like to thank my main supervisor Bill Williams for his constant support and guidance. I have learned a lot from you not only academically but also on living life in general (most of it acquired in our epic hiking adventures). In your supervision, I have certainly broadened my scientific thinking to the problems that I had or will have in the future, and for this I will be forever indebted to you. I would like to thank my co-supervisor Catherine Whitby for her constant guidance and perfectly timed motivation and making sure that I meet all my deadlines in time. I have certainly improved my way of approaching scientific writing under your supervision. Tracy Hale and Raoul Solomon from chromatin research group at Massey, collaborating with both of you was the best I had until now, thank you both for being patient and always motivating. Thanks Geoff Wilmott from University of Auckland and Gleb Yakubov from University of Queensland for having me in your lab and for your kind hospitality. Our Biophysics and Soft matter group for sharing with me their invaluable experiences which helped me immensely. Special thanks to our postdocs Allan Raudsepp and Rob Ward who always helped me in overcoming technical glitches in the lab. To my friends and family, thank you all for support, encouragement and kindness. Thanks to all the support staff of Massey University for always fulfilling my needs. Lastly, thank you New Zealand for the amazing experience I had in the past years (a hiking paradise), especially in this Covid phase where I could complete my work without any disruptions.

This project would not have been possible without funding from the MacDiarmid Institute, New Zealand (which included additional 3 months funding due to Covid-19).

Contents

List of Figures

List of Tables

List of Abbreviations

GSER	**G**eneralized **S**tokes **E**instein **R**elationship
PEO	**P**oly**e**thelene **O**xide
AFM	**A**tomic **F**orce **M**icroscopy
OT	**O**ptical **T**weezers
MA	**M**icropipette **A**spiration
MSD	**M**ean **S**quared **D**isplacement
SLM	**S**patial **L**ight **M**odulator
MPT	**M**ultiple **P**article **T**racking
QPD	**Q**uadrant **P**hoto **D**iode
CCD	**C**harged **C**oupled **D**evice
SD	**S**tage **D**isplacement
BD	**B**ead **D**isplacement
KD	**K**nock **D**own
MFG	**M**ilk **F**at **G**lobule
SEM	**S**canning **E**electron **M**microscope
SE	**S**tandard **E**rror
MFGM	**M**ilk **F**at **G**lobule **M**embrane

Physical Constants

Boltzmann constant	$k_B = 1.380\,648\,52 \times 10^{-23}\,\mathrm{m^2 s^{-2} K^{-1}}$

List of Symbols

r	radius	m
f_c	corner frequency	Hz
T_{msr}	total measurement time	s
A_p	particle amplitude	m
A_s	stage amplitude	m
m	mass of particle	kg
x_p^{dr}	position of trapped particle during stage driving	m
x_s	position of stage	m
τ	lag time	s
κ	stiffness	Nm^{-1}
ω	driving frequency	rad
γ	friction coefficient	Nm^{-1}
ϕ	phase difference	rad

Chapter 1

Background

1.1 Introduction

In the last couple of decades, there has been increased attention paid to interdisciplinary sciences. Researchers from the fields of physics, chemistry, and engineering are working closely with biologists to better understand biological systems. The main reason behind this movement is the development of quantitative techniques to probe biological samples at the cellular and molecular levels. One such growing field has emerged to be known as mechanobiology and considers how cells respond to and transduce mechanical forces.

In this thesis, the mechanical properties of MCF7 cells and their nuclei, and the adhesion of bacterial cells to milk fat globules has been studied. Polyethylene oxide solutions were studied as a prelude as a model viscoelastic material. Rheological properties were studied at the microscale and compared. These techniques have certain advantages over the use of conventional rheometers as they can measure at very high frequencies, require smaller sample volumes, probe the sample locally, and are relatively inexpensive to setup. This introductory chapter firstly reviews basic concepts in rheology and microrheology. Secondly, cell mechanics is introduced and different biophysical techniques are explained in detail to understand the mechanical measurements that have been performed on the biological samples.

1.2 Rheology and Microrheology

Rheology, from the ancient Greek words, rheo (flow) + logy (study of), is the study of the deformation and flow of matter. In general, rheology can be described as the study of the deformation and flow of a material in response to applied stress. Simple solids store energy and provide a spring-like elastic response, whereas simple liquids dissipate energy through viscous flow. For complex fluids, rheological measurements reveal both solid and fluid-like responses and the results generally depend on the time scale at which the sample is probed (Larson, 1999). The rheological properties of a material can be characterized by measuring the shear modulus as a function of frequency. Materials can experience different kinds of stress. Shear stress is the most commonly studied in the field of rheology. The resultant shear strain is defined as the deformation induced by the relative motion of two parallel surfaces seperated by a constant distance between which the material is held, as shown in Fig. 1.1.

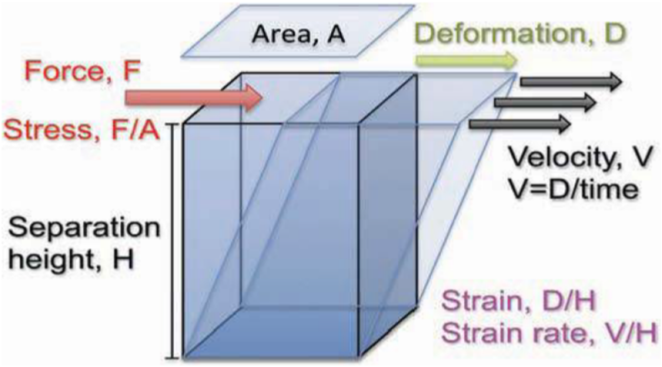

FIGURE 1.1: Shear flow schematic. Extract from (Tassieri, 2016)

The shear stress (σ) is defined as: $\sigma = \frac{F}{A}$. The deformation or shear strain (ϵ) of the material is described by the ratio between the relative displacement of the two parallel surfaces in the direction of flow and the relative distance between them, given by: $\epsilon = \frac{D}{H}$ for the sample shown in Fig. 1.1. The ratio between the shear stress and shear strain is termed as the Shear Modulus (analogous to the more commonly known Young's modulus for tensile stress and strain). The biophysical techniques which are described later in section 1.3.2 are based on the concepts of rheology. Most of the biophysical techniques deform the material and extract physical properties such as elasticity and viscosity. Fig. 1.2 shows the response of the material to creep and dynamic tests. A creep test consists in the application of a constant shear stress (σ) over time and recording of the resulting deformation ϵ(t) of the sample (left). For a dynamic test, the applied force oscillates, thereby resulting in an oscillatory deformation of the sample (right).

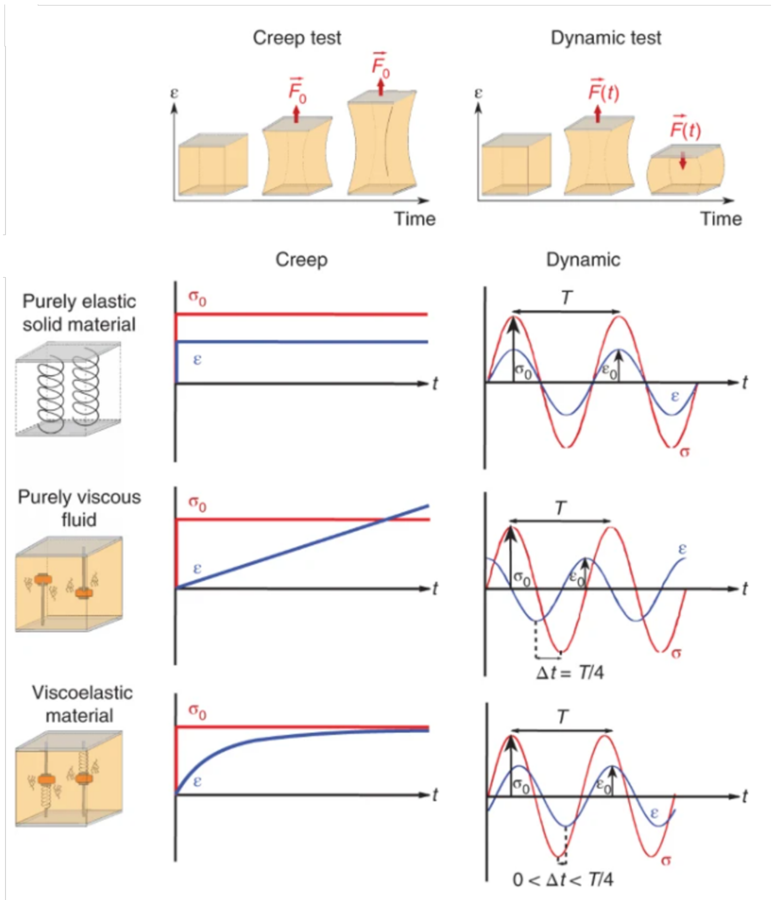

FIGURE 1.2: Illustration of material responses for a creep test and a dynamic test for a purely elastic material, a purely viscous fluid, and a viscoelastic material. T is the period of oscillation. Figure extracted from Wu et al (Wu et al., 2018).

Different biophysical techniques deform the material locally (smaller area) or globally (larger area). Traditionally, these measurements have been performed on several millilitres of material in a mechanical rheometer by applying a small amplitude oscillatory shear strain, $\epsilon = \epsilon_o sin(\omega t)$ and measuring the resultant shear stress, where ϵ_o is the amplitude and ω is the frequency of oscillation. The rate of deformation (shear rate) is then described by: $\dot{\epsilon} = \frac{d\epsilon}{dt}$. Conventional rheometers probe frequencies up to tens of Hz. Higher frequencies are limited by the onset of inertial effects. If the strain amplitude is small so that the fluid structure is not significantly perturbed then the time-dependent stress is given by:

$$\sigma(t) = \epsilon_o[G'(\omega)sin(\omega t) + G''(\omega)cos(\omega t)] \tag{1.1}$$

where $G'(\omega)$ is the response in phase with the applied strain, called the storage or elastic modulus, which describes the energy stored in the system when the strain is applied. $G''(\omega)$ is the response out of phase to the applied strain, called the loss or viscous modulus and is a measure of the viscous dissipation of the energy. The complex shear modulus is defined as: $G^* = G' + iG''$.

Conventional rheology measurements have given valuable insights into the structural and mechanical response of a variety of materials (Larson, 1999). However, it is not suited for all types of materials, as it typically requires tens of milliliter sample volumes. Hence probing rare samples is commonly not possible with a conventional rheometer. This makes microrheology ideal for costly or rare samples, since it requires sample volume in the order of microlitres. The microrheology technique can also provide insight about the local heterogeneity of the sample and reveal greater information about the structure of complex materials in the higher frequency regime (MacKintosh and Schmidt, 1999).

There are two types of microrheology: passive microrheology and active microrheology. Passive measurements rely on measuring the internal motion of probes (added or extant) within a system caused by thermal fluctuations. Active microrheology relies on inducing controlled external stresses on internalised probes, usually stronger than those resulting from thermal forces. Passive microrheology is described in this section. Active microrheology is described in section 3.3.2. Passive microrheology techniques typically use embedded micron-sized particles to locally deform the sample. The particles undergo Brownian motion due to thermal fluctuations from the environment, which are linked directly to the mechanical properties of the sample (Mason and Weitz, 1995).

Over the years there has been a growing use of microrheology techniques on food and biological systems which is discussed in appendix A and reviewed in an article in the Encyclopedia of Food Chemistry (Pradhan, Whitby, and Williams, 2018).

1.3 Cell Mechanics

While there is a growing use of microrheology in food systems, researchers, particularly with a background of soft matter physics, immediately found a strong implementation in a whole raft of biological materials. While the first experiments using the GSER (Generalised Stokes Einstein Relation) approach were performed on synthetic complex fluids, it was immediately clear that the sample volumes needed would be a particular advantage in biological systems. When one attempts to reproduce certain biological structures in vitro, the material has to be painstakingly extracted and purified from the biological matter. Hence, this field of probing biological samples using soft matter techniques is also termed as 'Cell Mechanics' or 'Biomechanics'. Cell biologists and physicists are currently working in tandem to bridge the gap of understanding the mechanics of cellular processes such as cell division, proliferation, differentiation, and cell motility.

1.3.1 Mechanical Properties

Every organism has the ability to detect, sustain, and interact with physical forces within its environment. For example, skin provides a protective barrier against bacteria and microbes that can cause infections. The skeleton provides the structural support needed to withstand gravity. Even respiration requires the generation of forces so we can breathe in and out. Bio-mechanics research in the past decades has focused on detecting and understanding the force generated at the organism level.

It is only in recent years that studies are being carried out at the cellular level. This is because of the development of new biophysical experimental methods to detect and measure physical forces at the cellular level. How a cell responds to a mechanical stimulus, that is, how it deforms in response to applied stress, and how this deformation evolves over time can be broadly termed as the 'mechanical properties' of the cell. In an elastic material, the constant of proportionality is called the modulus (Youngs, Shear or Bulk), with the unit of Pascals. Cells show both elastic and viscous properties and should strictly be referred to as viscoelastic materials. When a viscoelastic material is deformed, it simultaneously stores and dissipates the mechanical energy.

Therefore, the choice of a suitable experimental tool for mechanical measurements depends on the timescale, lengthscales, and elastic modulus of the material under study as shown in Fig. 1.3. This figure illustrates how the lengthscales, timescales, and the magnitude of the elastic modulus measured change with the size of the biological materials being probed.

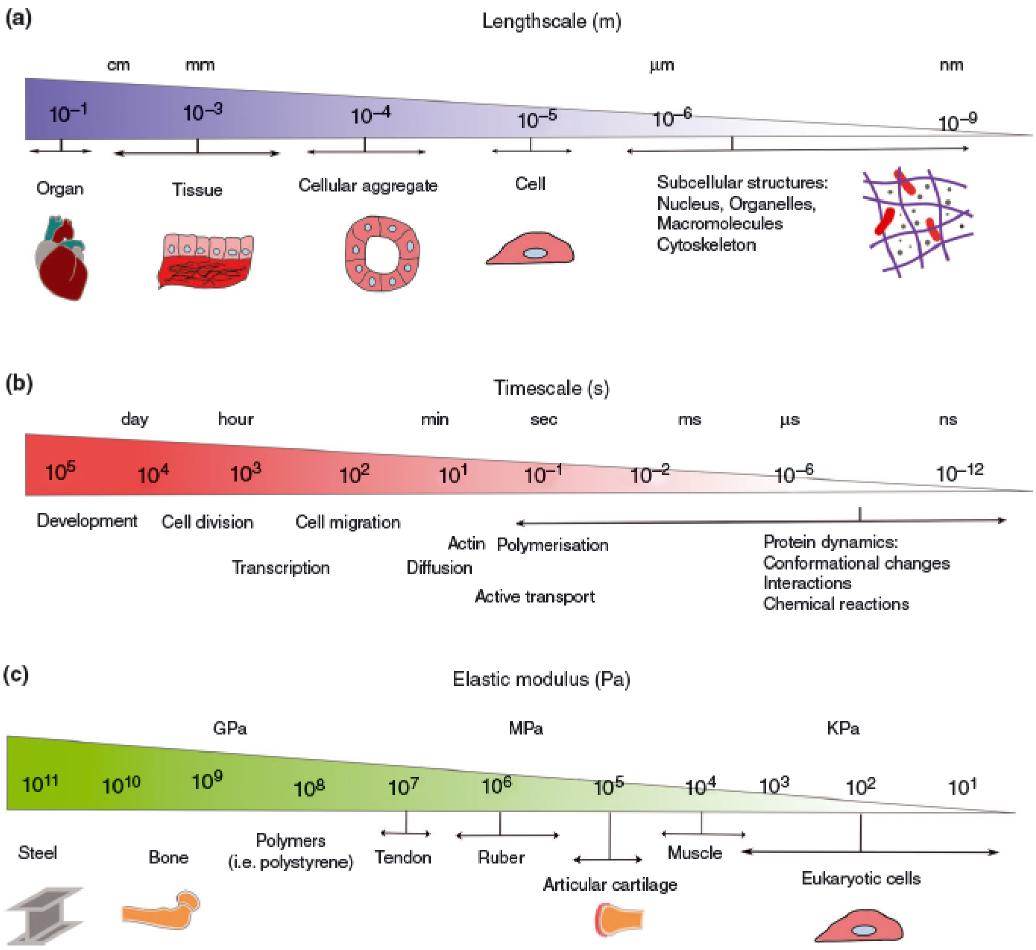

FIGURE 1.3: Parameters involved in choosing the right biophysical tool depending on (a) the lengthscale, (b) the timescale of the measurement and (c) elasticity of the sample). Figure extracted from (Moeendarbary and Harris, 2014)

1.3.2 Mechanical measurement techniques

As illustrated in Fig. 1.3, the choice of the experimental tool depends on three factors. Here in this thesis, we focus particularly on measuring mechanical properties at the cellular level using the techniques as shown in Fig. 1.4.

Fig. 1.5 (Left side) shows the local deformation applied to the cells using AFM (atomic force microscopy), MTC (magnetic twist cytometry), OT (optical tweezers),

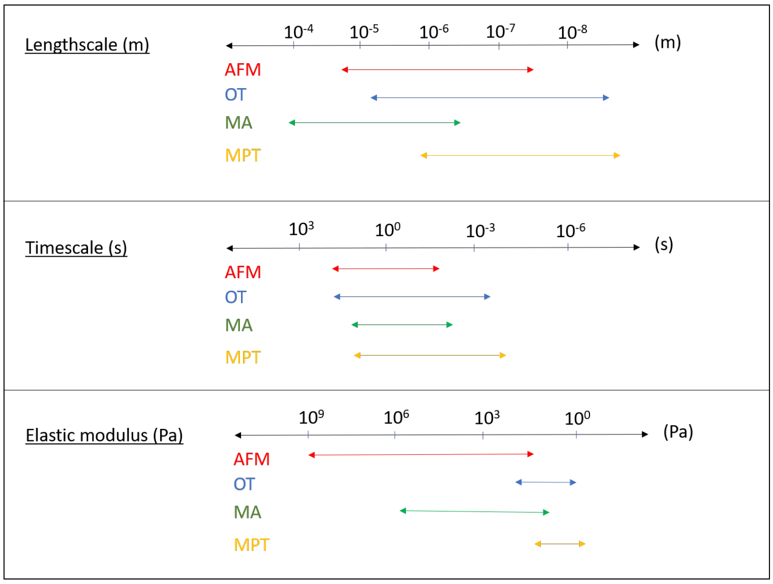

FIGURE 1.4: Comparison of approximate lengthscales, timescales and elastic modulus for AFM, OT, MA and MPT. This figure is just a general representation of the three parameters. The parameters can be different across different setups.

and MPT (multiple particle tracking) techniques, whereas Fig. 1.5 (Right side) shows the global deformation applied to cells using MA (Micropipette Aspiration), OS (optical stretcher), Microfludic assay and MS (Microplate stretcher).

AFM is a scanning probe microscopy which can be used for imaging and force spectroscopy at a sub micron resolution. AFM comprises of piezo controlled cantilever movement, a laser, and a detector. The tip of the cantilever is deflected in contact with the sample surface and this deflection is quantified using the deflection of a laser from the cantilever tip onto a photodiode (Müller et al., 2020; Li and Lim, 2010; Pimenta-Lopes et al., 2019).

OT uses a focused laser light to trap and manipulate dielectric particles using a high numerical aperture microscope objective. Particles near the focused trap feel the restoring force towards the center of the trap leading to particles getting trapped. Once the particle is trapped, the trapped particle can be used as a handle to deform the sample (as in AFM, but lower forces are applied) or to pull out a membrane tether from cells (Ashkin, 1992).

MA uses a micropipette with a controlled suction pressure to deform biological samples such as eukaryotic cells. As the cell is aspirated, the pipette radius, cell radius, and the length of the aspirated cell are quantified (Hochmuth, 2000; Hochmuth et al., 1996).

MPT uses a high-speed CCD camera to track the Brownian motion of several probe particles. A tracking algorithm is used to extract the coordinates of the particles from image sequence which ultimately gives the mean squared displacements of the particles (Crocker and Grier, 1996; Waigh, 2005a).

MTC uses an electromagnet to generate magnetic fields, which are then used to manipulate the magnetic beads. These magnetized beads can generate forces which can be used to probe biological samples. A twisting torque is applied to the magnetic field by a sinusoidal oscillating magnetic field which is perpendicular to the magnetic moment of the ferromagnetic beads. This rotates or twists the beads in the required direction (Zhang et al., 2017; Puig-De-Morales et al., 2001).

OS uses a dual beam optical trap to trap and deform biological samples (usually micron sized samples) in suspension Guck et al., 2001; Yang, Bragheri, and Minzioni, 2016.

Microfluidic devices consist of different sizes of micro channels which can be used to pass and deform the samples. Since the flow of fluid is controlled, microfluidic assays can also be used to deliver drugs and other chemicals inside the chamber to the subject of interest (Ito and Kaneko, 2020; Vanapalli, Duits, and Mugele, 2009).

MS consists of two microplates, one rigid and the other flexible with varied stiffness. The biological sample is attached to the two ends of the microplates, which can then be compressed and stretched by moving the flexible microplate (Wu et al., 2018; Kamble et al., 2016).

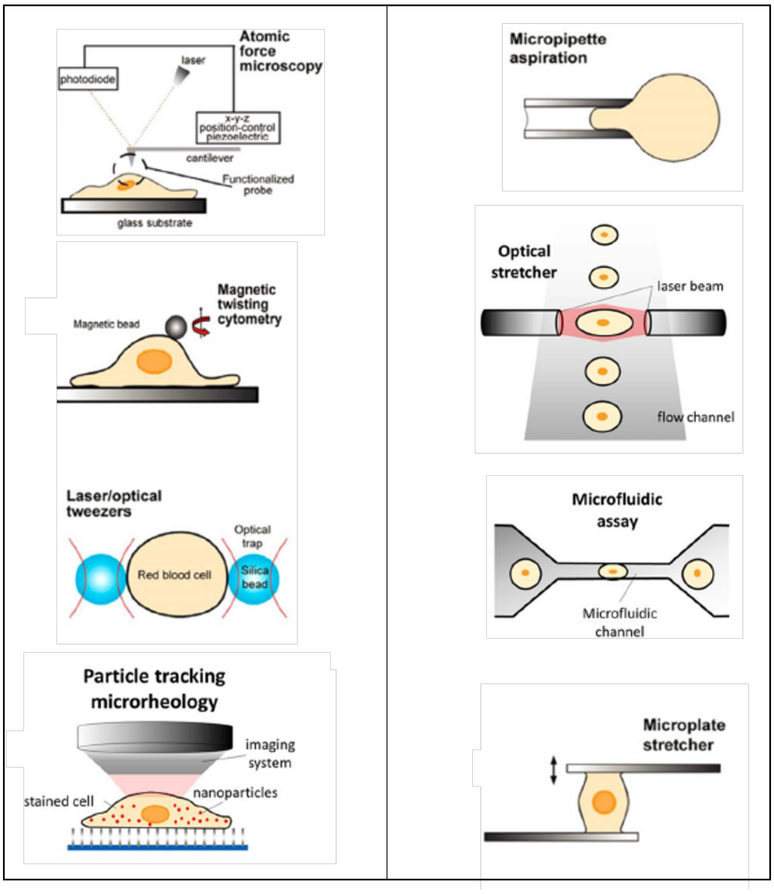

FIGURE 1.5: Major techniques for cell mechanics study. Left side of the image shows local deformation and the right side of the image shows global deformation applied on the cells. Figure extracted and rearranged from Unal et al., 2014

1.3.3 Applications and comparison of techniques

An important target in the field of cell mechanics is to understand how cells respond to forces. Past studies (Alberts, 2008) postulated that the mechanical environment of the cells impacts cellular processes. Hence, understanding the cell stiffness and cell membrane tension are important parameters that give insights into cellular and extra-cellular mechanical properties. For example, malignant cells are accompanied by specific changes in the mechanical properties of cells and their surrounding extra-cellular environment. These cancerous cells are less stiff compared to their healthy counter parts (Suresh, 2007). This decrease in cell stiffness with malignant transformation has been observed in a variety of cancers such as breast cancer, lung cancer, renal cancer, prostate cancer, oral cancer, skin cancer, and so on (Katira, Bonnecaze, and Zaman, 2013). Understanding the mechanical properties of axons in neurons can also give insight into neurodegenerative diseases (Dubey et al., 2020; Datar et al., 2015). This is done by depleting microtubules in neurons (loss of microtubules is associated with neurodegenerative diseases) and measuring the significantly altered mechanical properties. Microtubules were depleted by inhibiting polymerisation using Nocodozole.

The techniques shown in Fig. 1.5 have their own advantages and disadvantages in terms of spatial and temporal resolution as well as the range of forces that can be applied to samples. Table 1.1 gives a comparison of some common force spectroscopy techniques.

TABLE 1.1: Comparison of force spectroscopy techniques.

	OT	MTC	AFM	MPT	MA	OS	MS
Force range (N)	$10^{-11} - 10^{-14}$	$10^{-10} - 10^{-12}$	$10^{-7} - 10^{-11}$	$10^{-7} - 10^{-11}$	$10^{-7} - 10^{-10}$	$10^{-7} - 10^{-11}$	$10^{-7} - 10^{-9}$
Deformation type	local	local	local	local	global	global	global
Features	Low-noise and low-drift dumbbell geometry	Force clamp; Bead rotation; Specific interactions	High-resolution imaging.	It provides insight into intracellular dynamics and structure; Tracking multiple organelles in cells.	Real time correlation of pressure and whole cell deformation.	High throughput; Cells can be suspended to eliminate mechanical contact	Sufficient to induce significant deformation on entire cell; low drift.
Limitations	Photodamage; Sample heating; Nonspecific	No manipulation (Force hysteresis)	Large high-stiffness probe; Large minimal force.	Computationally Intensive; Limited by frame rate of camera	Computational or Analytical model assumptions are sometimes harder to validate.	Requires higher laser power which can damage the cells.	Low throughput; Time consuming; Only applicable to strongly adherent cells. Nonspecific.

1.4 Overview and aims of the thesis

This thesis aims to apply biophysical techniques to study the mechanical properties of viscoelastic systems, cancer cells and their nuclei, and the interactions of different bacterial strains with milk fat globule membranes (MFGM). **Chapter 2** introduces the techniques, which are mainly used to understand the mechanical aspects of the system using a general soft matter physics approach. This thesis has four main experimental chapters.

Chapter 3: The goal of this chapter was to implement and understand the use of microrheological techniques to a model viscoelastic system (Polyethylene oxide (PEO)) using MPT and OT. This chapter describes the use of passive (MPT) and active microrheology (OT) techniques to deduce viscoelastic properties such as viscosity and elastic modulus. Understanding the calibration of OT in a viscoelastic environment is also one of the highlights of this chapter.

The main aim of this chapter was to investigate the viscoelastic properties of model viscoelastic systems (PEO) using OT, as most of the biological systems are viscoelastic in nature. This chapter also strengthened my understanding of OT technique, which gave me confidence in the experiments related to biological systems.

Chapter 4 moves from a model viscoelatic system to a biological system where OT techniques are used to investigate the mechanical properties of MCF7 breast cancer cells following the depletion of the protein HP1α from inside the nucleus. This chapter introduces the use of OT : i) to produce indentation on cells and extract an elastic modulus, ii) to pull a membrane tether from the cells and extract membrane tension.

Heterochromatin protein 1α is an architectural protein and contributes to the sequestration of heterochromatin at the nuclear periphery through its interactions with proteins embedded in the lamina and nuclear membrane. We hypothesise that due to the physical coupling of the nucleus and the cytoskeleton through linkers of nucleoskeleton and cytoskeleton (LINC) complexes, it is expected that changes within the heterochromatin and the lamina that lines the inner nuclear membrane, not only modify the structural integrity to the nucleus, but also influence cytoskeletal dynamics. Since the loss of HP1α is associated with metastatic potential and its knock-down

(KD) increases the invasive potential of MCF7 cells though a three dimensional extracellular matrix in vitro (Norwood et al., 2006), this suggests that the depletion of HP1α also affects the mechanical properties of the cell as a whole. This chapter (chapter 4) uses an OT-based method for tether extension and compares the membrane mechanical properties of MCF7 cells with HP1α KD to MCF7 control cells.

Chapter 5 introduces nuclei mechanics. Here, the nuclei were isolated from both wild type MCF7 cells and HP1α depleted cells. This chapter highlights : i) the use of AFM, OT and techniques based on Micropipette Aspiration (MA) to characterize the mechanical properties of these nuclei, ii) and the differences in chromatin organisation of wild type and HP1α knockdown MCF7 cells that were observed by microscopy techniques and biological assays.

The previous chapter (chapter 4) indicated that the mechanical properties of whole MCF7 cells were altered by the depletion of HP1α, here in chapter 5, we measure how the material properties of the extracted nuclei are modified following the knockdown HP1α. We hypothesise that given the role of HP1α in heterochromatin organisation, this raises the possibility that reduction of HP1α aids malignant cell invasion, not only by disrupting gene silencing but also by altering the mechanical properties of the nucleus. As reported in the literature (Stephens et al., 2017b; Norwood et al., 2006; Stephens et al., 2018), interconnected filament networks such as A-type lamin and B-type lamin proteins have different mechanical properties and could respond accordingly to the range of forces applied. Therefore, we have used a combination of OT (low force - local deformation), AFM (high force - local deformation), and MA (global deformation).

Chapter 6 introduces a study that developed a method to measure the interaction force between two Lactobacillus strains and the MFGMs using OT techniques. Interaction between MFGMs and bacteria is an adhesion phenomenon driven primarily by the bacterial surface properties (proteins). Therefore, we hypothesise that the two strains which have different surface proteins will interact differently with the MFGMs.

Chapter 7 provides the summary of the thesis and discusses possible future work.

Chapter 2

Method and Calibration

This chapter describes the biophysical techniques used in this thesis to understand the mechanical properties of the micro scale environments and the results of some exemplar experiments carried out to characterize the limits of the techniques in terms of spatial and temporal resolution. These techniques operate at the micron level and can be broadly categorized as microrheology techniques. Microrheological techniques are classified into passive and active. Passive microrheology is the study of the system properties under the influence of only thermal fluctuations. However, active microrheology is concerned with observing how the system responds to externally applied forces.

2.0.1 Obtaining the complex modulus from the MSD

To obtain the complex modulus of the material, the first step is to extract the mean square displacement, MSD ($\langle \Delta r^2(t) \rangle$) of the microscopic probes, in the simplest case from the imaged position of the tracer particles using:

$$< \Delta r^2(\tau) >=< [x(t+\tau) - x(t)]^2 + [y(t+\tau) - y(t)]^2 + [z(t+\tau) - z(t)]^2 > \tag{2.1}$$

where τ is the lag time and x,y,z represents the position data in 3-D. If the material is completely viscous, the MSD of the particles will increase linearly with the lag time (τ) having a slope of one on a logarithmic scale. The MSD of a purely elastic material will not increase with time and will show a slope of zero, whereas a viscoelastic material will have a slope between zero and one, which can be different on different time scales.

To derive a relationship between MSD and G^* (complex modulus), Mason and Weitz (Mason and Weitz, 1995) employed a generalized Langevin equation:

$$m\dot{v}(t) = f_R(t) - \int_0^t \zeta(t-\tau)v(\tau)d\tau \tag{2.2}$$

where m is the mass of the particle, $v(t)$ its velocity and f_R is the resultant of all random forces acting on the particle. The integral term with $\zeta(t)$ is associated with the viscous damping of the fluid. The equation can be solved in the Laplace domain (s - complex variable) giving rise to Generalized Stokes Einstein Relationship (GSER) which connects the probe particle's MSD to the shear modulus of a generic surrounding viscoelastic fluid:

$$\tilde{G}(s) = \frac{k_B T}{\pi a s < \Delta r^2(s) >} \tag{2.3}$$

where k_B is Boltzmann constant, T is the temperature, a is the radius of the probe particle, s is the complex variable (transformation of time domain to Laplace domain s) and $< \Delta r^2(s) >$ is the MSD in Laplace domain. An equivalent GSER representation in the frequency domain (ω) can be written as:

$$G^*(\omega) = \frac{k_B T}{\pi a i \omega \mathscr{F} < \Delta r^2(t) >} \tag{2.4}$$

In order to determine $\tilde{G}(s)$, the Laplace transform of the experimentally measured MSD is needed. MSD measurements are generally known at discrete times over a limited temporal range, where transforming to the frequency domain introduces errors in the moduli. The numerical Laplace transform is typically implemented by selecting a Laplace frequency 's', multiplying the MSD ($< \Delta r^2(s) >$) by a decaying exponential and integrating using the trapezoid rule. While this method is accurate within frequency extremes, it introduces errors near the frequency extremes due to truncation of data.

To overcome these errors, Mason et. al. (Mason, 2000) estimated transforms algebraically by expanding the MSD locally around the frequency of interest, ω, and retaining the leading term:

$$< \Delta r^2(t) >=< \Delta r^2(1/\omega) > (wt)^{\alpha(\omega)} \tag{2.5}$$

where $< \Delta r^2(1/\omega) >$ is the magnitude of MSD at $t = 1/\omega$ and

$$\alpha(\omega) = \frac{d \ln < \Delta r^2(t) >}{d \ln t}\Big|_{t=1/s} \tag{2.6}$$

is the power law exponent describing the logarithmic slope of MSD ($< \Delta r^2(t) >$) at *t* = *1/s*. For thermally driven spheres, this slope must lie between one and zero, corresponding to elastic confinement and viscous diffusion, respectively. The Fourier transform $\mathscr{F} < \Delta r^2(t) >$, of the power law is directly evaluated as follows:

$$i\omega\mathscr{F} < \Delta r^2(t) >\approx< \Delta r^2(1/w) > \Gamma[1+\alpha(\omega)]i^{-\alpha(\omega)} \tag{2.7}$$

where Γ is the gamma function which is represented by: $\Gamma[1+\alpha] \approx 0.457(1+\alpha)^2 - 1.36(1+\alpha) + 1.90$ for this range of α. Substituting in equation 2.4 and using Euler's equation, we obtain:

$$G'(\omega) = |G^*|(\omega)cos(\pi\alpha(\omega)/2) \tag{2.8}$$

$$G''(\omega) = |G^*|(\omega)sin(\pi\alpha(\omega)/2) \tag{2.9}$$

where

$$|G^*(\omega)| \approx \frac{k_B T}{\pi a < \Delta r^2(1/\omega) > \Gamma[1+\alpha(\omega)]} \tag{2.10}$$

These relations provide a way to extract elastic and loss moduli from the MSD, which is the primary quantity measured.

2.1 Multiple Particle Tracking (MPT)

Multiple particle tracking (MPT) is used in a passive microrheology technique to track the Brownian motion of several probe particles in a single field of view. A tracking algorithm is used to extract the x-y coordinates of the particles from recorded image sequences. (Crocker and Grier, 1996). This gives the trajectory of the probe particles (Waigh, 2005b). The combination of fluorescent probe particles and fluorescence microscopy gives a better signal to noise ratio when compared to using bright field microscopy. This also makes it easier for the tracking algorithm to detect the particles. Since Brownian motion is stochastic in nature, it is the fluctuations of particles or the mean squared displacement (MSD) of the probe particles that is of interest. The mobility of the tracer particles reflects the mechanical properties of the micro- scale environment in which they move.

The advantages of using MPT are: i) It requires small volumes of samples. ii) It can probe spatially heterogeneous systems or multiphase solutions. iii) Good statistics can be gathered to get the best estimate of the MSD of probe particles. iv) Biological cells and membranes can also be probed. It can also track organelles inside cells.

The disadvantages are: i) It is limited by the frame rate of the camera. ii) The data typically has to be analyzed off-line, which is computationally intensive (Cicuta and Donald, 2007a) (although real time particle tracking has been demonstrated (Huang et al., 2013)).

2.1.1 Experimental method

An inverted microscope (Nikon Eclipse TE2000-U) on an air damped table with a mercury fluorescent lamp (X-cite Series 120PC EXFO), a 60x 1.2 NA (Nikon, Plan Apo VC 60x WI) water immersion objective lens and CCD Camera (Andor Neo) were used to image and track the particles. Fluorescent Polystyrene spheres with diameter of 1μm (Poly Sciences Polystyrene 2.6% Solids-Latex) were used unless stated. This methods was tested using standard solutions of known viscosity. Image series were acquired for 10 seconds and x-y coordinates of the particles were extracted using polyparticle tracker algorithm (Rogers et al., 2007). A frame rate of 100 fps was used for all the measurements. Particle tracking algorithms were implemented in different programming platforms as given at the URL: `http://www.physics.emory.edu/faculty/weeks//idl/`.

2.1.2 Demonstrations using Glycerol-water solution : The MSD recovers the viscosity

Glycerol-water solutions were used as viscous solutions to test the accuracy of the viscosities extracted from MPT. Well-mixed water-glycerol mixtures are close to purely viscous homogeneous media and are well characterized at various concentrations.

Solutions were made to glycerol concentrations of 80 vol%. The solutions were made by mixing glycerol (99.9%, Ajax Laboratory Chemicals), milliQ water and 1 μm fluorescent particles (0.05 vol%) in diameter using a magnetic stirrer for 2 hours.

The motion of probe particles in solution can be described by the MSD ($< \Delta r^2 >$) of the particles as a function of time interval (τ), where $\tau = t - t_0$, and t_0 is the initial observation time.

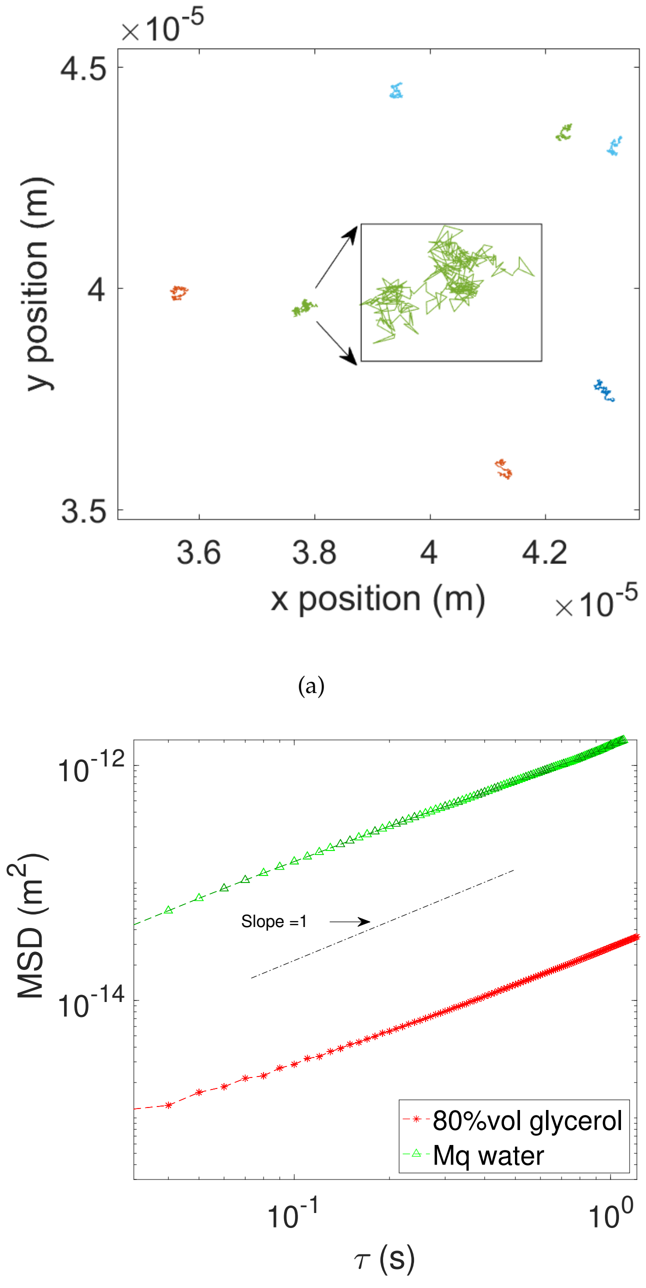

(a)

(b)

FIGURE 2.1: a) Brownian motion of particles in milli-Q water (inset shows the zoomed Brownian motion of a single particle), b) MSD (τ) of particles in milliQ water (*green*) and glycerol-water mixture (*red*).

As seen in Fig.2.1, individual tracks appear stochastic and (a) the MSD of particles show a diffusive behavior with a slope close to one on a log-log scale. (b) As glycerol is added, the amplitude of the MSD decreases. Since the glycerol-water solution is Newtonian fluid (i.e, a fluid with a constant velocity η), the MSD and τ are predicted to be proportional to each other:

$$< \Delta r^2 >= 4D\tau \tag{2.11}$$

in 2-dimensions, where D is the diffusion coefficient of the probe particles. As the particle size is known, one can directly measure the viscosity of the medium from the diffusion coefficient at a particular temperature (T) using Stokes-Einstein relation:

$$D = \frac{k_b T}{6\pi\eta a} \tag{2.12}$$

where a is the radius of the particle and k_b is the Boltzmann constant.

Using equations 2.11 and 2.12, the viscosity of 80 vol% was found to be (0.0602 ± 0.0007) Pa.s respectively at 20 °C. This is in fair comparison with literature values 0.0601 Pa.s at 20 °C (Segur and Oderstar, 1951).

2.1.3 Van Hove distribution

To extract information about the heterogeneity of a sample, one can plot a distribution (or histogram) of the displacements at a specific lag time. This distribution is known as the Van Hove distribution. For a homogeneous solution, the distribution has a Gaussian shape which implies that the differences in the distance traveled by different particles is purely due to the thermal fluctuations. The Van Hove plot for the 80% glycerol-water solution shows a Gaussian shape at two different time lags selected, as shown in Fig. 2.2. The variance of this distribution corresponds to the MSD of the probe particles at the relevant times. If the system is heterogeneous, the Van Hove plot will have a non-Gaussian shape reflecting the presence of different micro environments.

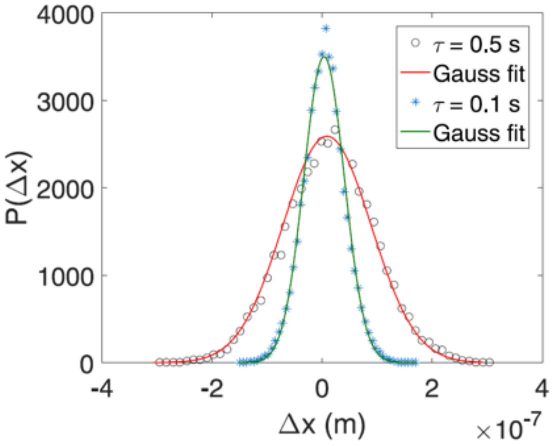

FIGURE 2.2: Van Hove distribution at different lag times for 80 vol% Glycerol.

Having described passive microrheology using MPT, we now describe active methods where external forces over and above those imparted by thermal fluctuations are applied. The force that needs to be applied is very small (≈ pN). Hence an Optical Tweezers (OT) setup are used and this technique is described in the following section.

2.2 Optical Tweezers (OT)

Optical Tweezers (OT), also known as optical traps, are formed by a highly focused laser beam. The laser beam is typically focused using a microscope objective with a high numerical aperture to maximise gradient forces. When focused on a specimen plane, this beam can manipulate and capture micron sized dielectric particles (Ashkin, 1992; Ashkin, 1999). The forces felt by the particles consist of light scattering, gradient forces and absorption due to momentum transfer of light. The focused laser acts as an attractive potential well for particles whose refractive index is higher than the surrounding medium (Neuman and Block, 2004). A schematic of the OT setup in our lab is shown in Fig.2.3.

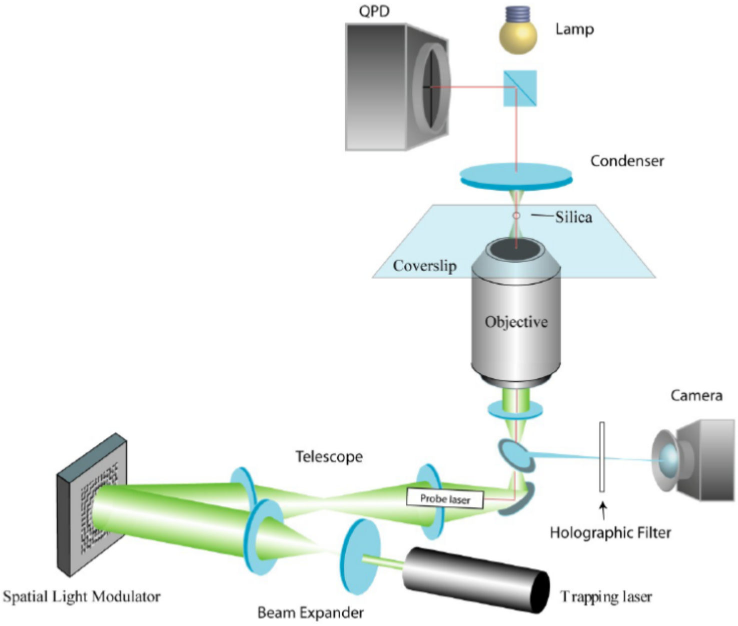

FIGURE 2.3: Optical Tweezer schematic. Optical Tweezer setup consists of a) Two trapping laser of 2W (for SLM) and 5W (high power trap) with a wavelength of 1064 nm, b) Spatial light modulator, c) Beam expander and beam steering lens, d) CCD Camera (Tracking particles) and e) Quadrant Photodiode (QPD) (Tracking particles).

When the diameter of the trapped particle is equal to or greater than the wavelength of light, a simple ray optics model can be used to explain the forces as shown in Fig. 2.4.

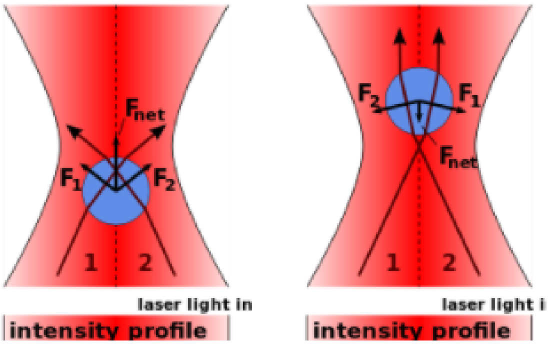

FIGURE 2.4: Ray optics explanation for focused laser. The momentum change of the focused rays causes a force towards the laser focus, both when the bead is in front (left image) or behind (right image) the laser focus. So, the bead will stay slightly behind the focus, where this force compensates the scattering force. Image extracted from wikipedia.

Fig. 2.4 shows that the individual rays of light (1 and 2) emitted from the focused laser are refracted as they enter and exit the dielectric particle resulting in a change of momentum of the light. As a result, there should be an equal and opposite change in momentum of the particle due to Newton's third law. If the particle is slightly displaced from the center of the trap, then there will be a net force (F_{net}) acting on the particle to return it to the center of the trap, which is also called a restoring force. If the particle is located at the center of the beam, then the individual rays of light are refracted through the particle symmetrically, resulting in a stably trapped particle. All the above criteria is valid considering that a particle minimally reflects the light. However, the particle does reflect the light in small amount, pushing the particle slightly above the trap focus.

2.2.1 Particle detection

In addition to using a CCD camera as described in section 2.1.1, a QPD (quadrant photodiode) can also be used to detect a single particle moving in an optical trap. A QPD has the advantage of higher sampling rate and temporal resolution compared to a CCD camera. However, it can only track one particle at a time unlike MPT. All the comparison were done with particles suspended in mQ water.

2.2.1.1 Optical Tweezers measurements using QPD

Quadrant photodiodes (QPDs) are discrete components consisting of four optically active areas separated by a small gap (around 10s of μm). In an optical tweezer system, a QPD is typically placed at the back focal plane of the condenser as shown in Fig. 2.5.

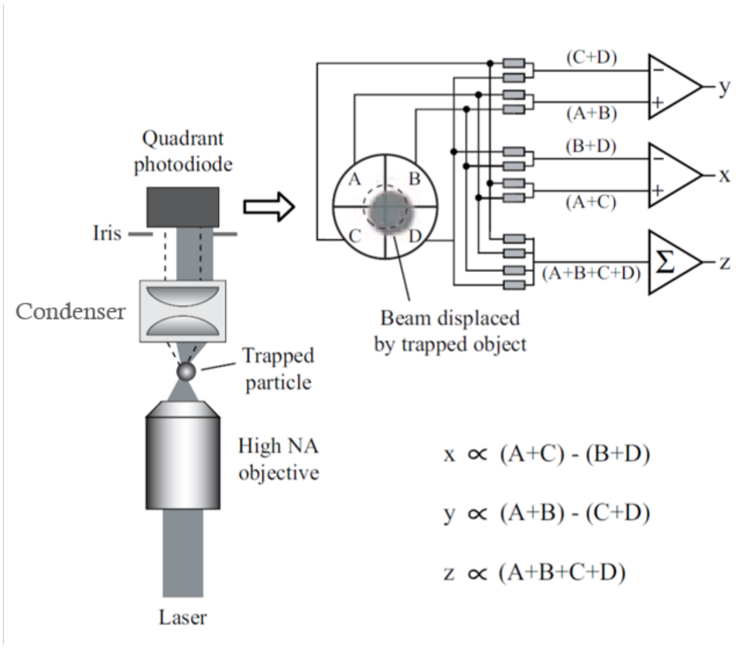

FIGURE 2.5: QPD Schematic Layout. Figure from (Tassieri, 2016).

In this setup the probe laser with a wavelength of 670 nm and laser power of 2.5 mW was used. The probe laser is focused onto the QPD using the condensing lens of the microscope (back focal plane) to monitor the position of the trapped bead. Translations of a trapped bead within the probe laser cause translations of the scattering pattern at the back-focal plane, which is then detected by the QPD. A QPD produces an output in volts and a calibration factor must be measured to relate voltage to displacement. To calibrate the QPD, a particle adhered to the coverslip is typically used. Moving the adhered particle a set distance using a piezo electric stage deflects the probe laser light, creating a voltage change from the output of QPD. This gives a calibration constant, as shown in Fig 2.6.

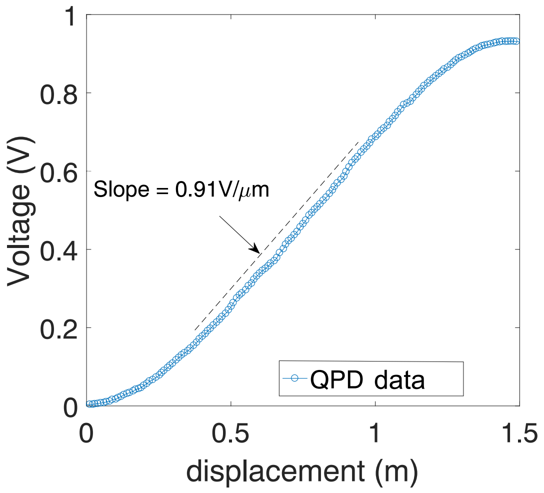

FIGURE 2.6: Voltage to distance conversion in QPD.

2.2.2 Manipulating traps using Spatial Light Modulators

Spatial light modulators (SLM) are diffractive optical elements (DOE), where a voltage applied to each pixel of the device changes the local refractive index of the liquid crystal layer as shown in Fig.2.7.

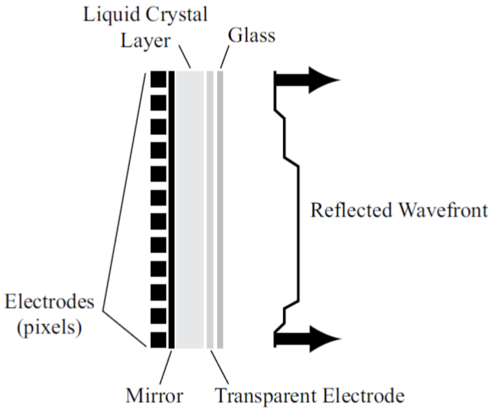

FIGURE 2.7: A Liquid crystal spatial light modulator. Extract from (Tassieri, 2016)

When the SLM is illuminated by the laser beam as shown in Fig.2.3, the phase fronts of the reflected beams from each pixel are shifted by an amount between 0 and 2π due to the spatially varying refractive index. This spatial variation is controllable which splits a single collimated laser beam into several separate beams, each of which is focused in an optical tweezer by a strongly converging lens (Dufresne and Grier, 1998). The interference pattern between the different phase fronts generates the required intensity profile in the image plane. This can be manipulated and can trap multiple objects in real time allowing the movement of multiple traps to be coordinated, as shown in Fig. 2.8.

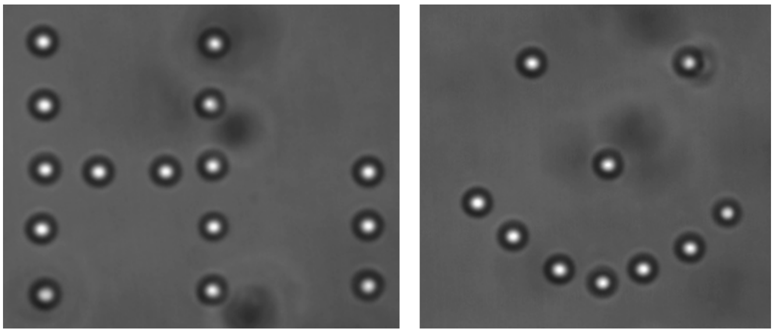

FIGURE 2.8: Multiple traps using a SLM, trapping 1 μm beads (1 W - SLM Trap, 1064nm).

2.2.3 Experimental setup

In the OT setup, a Nd:YAG laser (Spectra Physics) of power 2 W and wavelength of 1064 nm is used to trap particles. Particle displacements are recorded using a QPD (50 kHz) (FMS-D, Arryx) and a CCD (500 Hz) (Andor Neo). For QPD detection, which has the advantage of higher sampling rate compared to CCD camera, a 2.5 mW probe laser (Thorlabs S1-FC-675) which is focused at the QPD using the back focal plane of the condenser detects the translations of a particle in a trap. A piezo electric stage is used for precise stage displacements as described in appendix (B.1).

2.2.4 Comparison between CCD Camera and QPD

Data Acquisition on the movement of probe particles can be performed using a CCD Camera or a QPD. Each has its own advantages and disadvantages. Data recorded using a CCD/CMOS camera has the advantage of tracking multiple particles simultaneously. The latest CCD/CMOS cameras are only able to record data at rates in the order of kilo hertz, whereas a QPD can record intensity fluctuations in the order of $\sim$ 100 kHz.

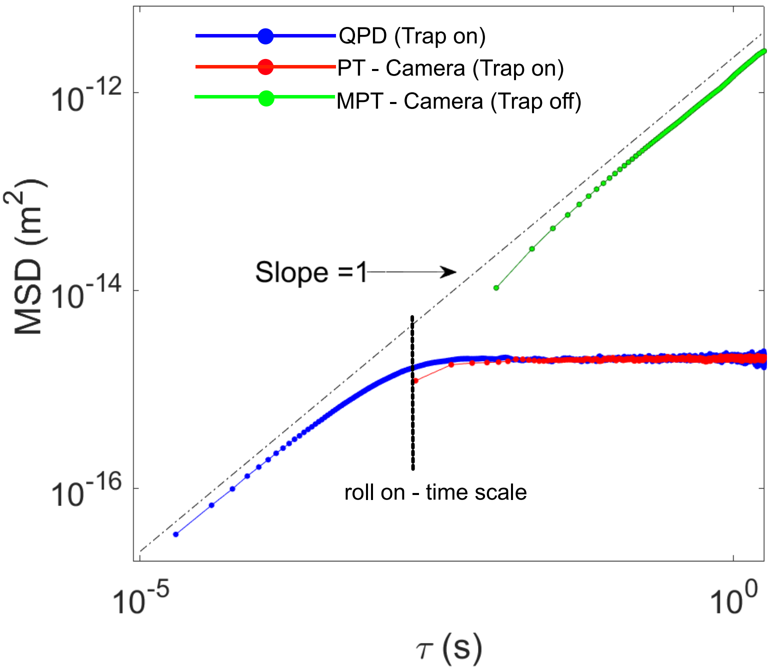

FIGURE 2.9: Plot showing comparison of MSD of a freely diffusing and an optically trapped 1um polystyrene bead in milliQ water measured using QPD measurement (50 kHz) and CCD Camera (500 Hz). PT- particle tracking using CCD camera, MPT- multiple tracking using CCD camera. Thin black line shows slope of 1 and thick black line shows roll on time scale when a particle moves from a diffusive to elastic behaviour.

Fig. 2.9 shows that MSD data recorded using a QPD and particle tracking of an optically trapped bead. They have approximately similar 'roll on' characteristic times. The QPD reveals that even in the trap, at short time scales, the MSD is diffusive. At long time scales, it reaches a plateau due to trap confinement. For a free particle, the MSD is diffusive at all - time scales which is shown by the slope of 1 (dotted lines). The behavior is described in more detail in the following section 2.2.5. As shown in Fig. 2.9, the camera data at short time scales do not agree well with QPD data, this could be due to the finite bandwidth and exposure time of the CCD camera (Loosemore and Forde, 2017).

2.2.5 Calibration of Optical Tweezers in MilliQ water

The main idea of using an OT in this work is to apply forces to biological samples. To quantify the force, we need to calibrate the strength of the trap. This is typically done by monitoring the average response to thermal fluctuations, which have a known magnitude at a particular temperature.

Optical tweezers exert force on dielectric particles within the range of pN to 100pN. This makes them an ideal force transducer to understand various biological systems as most of the cellular biological processes involve forces within this range. The motion of a trapped dielectric particle exhibits the form of over-damped harmonic oscillator in a viscous solution. The trapping forces can be modeled as a Hookean spring for displacements smaller than a particle radius.

$$f = -kx \tag{2.13}$$

where k is the spring constant and x is the distance from the center of the trap to the center of the trapped particle.

2.2.5.1 Equipartition method

An optically trapped bead in thermal equilibrium moves randomly within the trap. Due to the optical force, the natural Brownian movement is confined in the trap region, near the objective focus. The average energy of the Brownian motion of the trapped particle, from thermal energy in the environment in one dimension, is $\frac{1}{2}k_BT$. The average energy the trap exerts on the particle is related to energy of a Hookean spring: $\frac{1}{2}k < x^2 >$. On equating the two relations, the trap stiffness (k) can be calculated:

$$k = \frac{k_BT}{< x^2 >} \tag{2.14}$$

Fig. 2.10 shows the position histogram of a particle of 1 μm in diameter trapped using OT. The Gaussian shape indicates that the particle spends more time at the center of the trap. The full width at half maximum (FWHM) of the Gaussian fit is related to the variance $< x^2 >$ of the position fluctuations and these fluctuations are related to the trap strength in the plateau (the flat region of QPD and camera data in Fig.2.9).

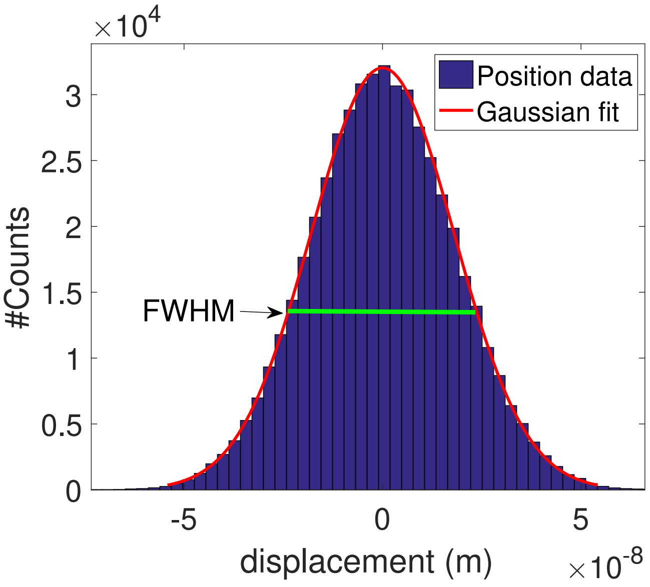

FIGURE 2.10: Position Histogram of trapped particle. Red curve shows the Gaussian fit to the position data and the green line shows the full width at half maximum (FWHM).

Equation 2.14 can be very useful for quickly estimating the trap parameters in real time (Berg-Sørensen and Flyvbjerg, 2004). However it becomes less accurate for noisier data sets because the harmonic model (and thus the Gaussian probability distribution) fails for particle positions far from the centre. The MSD of a particle in a trap measured using a QPD is shown in Figs. 2.9 and 2.11 (for different laser powers).

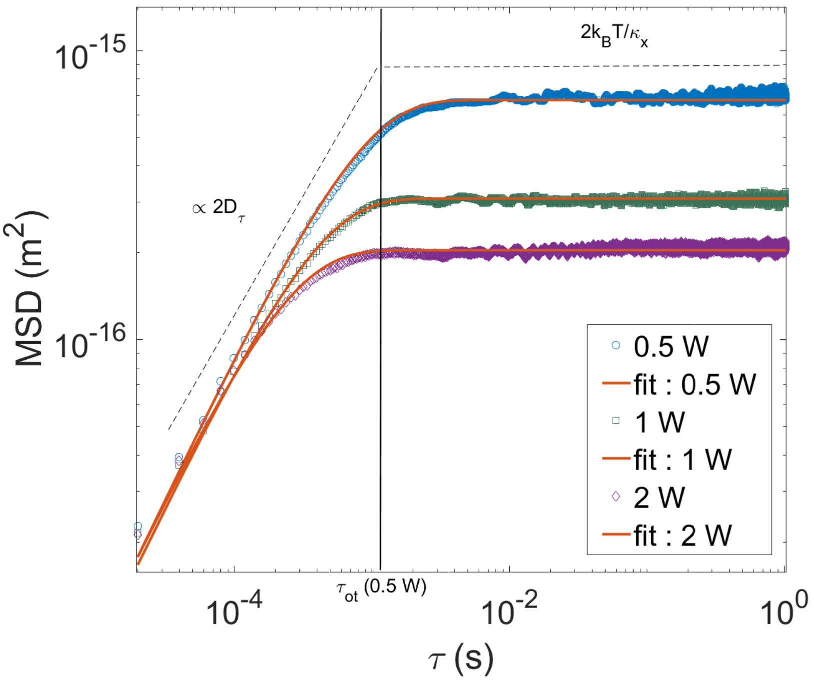

FIGURE 2.11: MSD of trapped particle at different laser powers. The red curves shows the fit to MSD data. The back line shows the roll on time scale for 0.5 W.

At short time scales, the MSD is diffusive (increases as a linear function of τ) as the particle displacement is very small and it does not feel the trap. At long times scales, the MSD plateaus are due to the trap confinement. In this region the MSD of the particle at different laser powers is directly related to the strength of the trap. The stronger the trap, the sooner the plateau is reached. The MSD transition from linear growth to plateau (due to confinement) occurs at a characteristic time τ_{ot}. The MSD of an optically trapped bead is given by:

$$MSD_x(\tau) =< [x(t+\tau) - x(t)]^2 >= 2\frac{k_BT}{\kappa_x}[1 - e^{-\frac{|\tau|}{\tau_{ot}}}] \tag{2.15}$$

where κ_x is the trap stiffness and $\tau_{ot} = \frac{\gamma}{\kappa_x}$ is the trap characteristic time. $\gamma = 6\pi\eta a$ is the friction coefficient and 'a' is the radius of particle. $MSD_x(\tau)$ features a transition from a linear growth corresponding to free diffusion behavior at short time scales ($\tau << \tau_{ot}$) to a plateau due to confinement at long time scales ($\tau >> \tau_{ot}$). This equation is derived from the solution to the Langevin equation (2.18) which is described in the next section.

TABLE 2.1: Measurement of stiffness (8 measurements at each laser power) at 3 different laser powers (SLM) using Equipartition method and MSD method (Bead diameter - 1 μm, Laser wavelength -1064 nm)

Laser Power (W)	**Equipartition (k (pN/μm))**	**MSD - fit method (k (pN/μm))**
0.5	7.5 ± 0.5	8.6 ± 0.4
1	15.2 ± 0.4	16.4 ± 0.3
2	29.1 ± 0.3	31.2 ± 0.4

2.2.5.2 Power Spectrum Method

The power spectrum analysis of the position of the trapped bead is another alternative method to calibrate optical tweezers and is considered to be the most reliable option (Berg-Sørensen and Flyvbjerg, 2004). The main idea here is that the frequency of the motion of the bead in a trap is related to the strength of the trap. It has the advantage of working in the frequency domain, so it gives an indication of the sources of noise which can be removed by notch filtering if required.

The thermal forces can be balanced against the optical force, the Stokes drag force and the inertial force to give the Langevin equation for 1-D:

$$m\ddot{x}(t) + \gamma\dot{x}(t) + \kappa_x x(t) = \xi(t) \tag{2.16}$$

where m is the mass of the particle, $x(t)$ is the trajectory of the particle, κ_x is the trap stiffness and ξ is the stochastic force exerted on the particle. γ is the friction coefficient given by

$$\gamma = 6\pi\eta a \tag{2.17}$$

where η is viscosity and a is the radius of the particle. In the low Reynolds number regime, it is possible to drop the inertial term in equation 2.16, and obtain the over-damped Langevin equation:

$$\dot{x}(t) + \frac{\kappa_x}{\gamma}x(t) = \xi(t) \tag{2.18}$$

Here, $\kappa_x x(t)$ is the harmonic force contribution of the trap. $\langle \xi(t) \rangle$ is the random force with zero mean, i.e.,$\langle \xi(t) \rangle = 0$, uncorrelated with the actual particle position, i.e, $\langle \xi(t)\xi(t+\tau) \rangle = 2D\delta(\tau)$, where $D = k_B T/\gamma$. Using these properties, $\xi(t) = \sqrt{2D}W(t)$, where $W(t)$ is a white noise. $W(t)$ is characterized by following properties:

- $\langle W(t) \rangle = 0$;
- $\langle W(t)^2 \rangle = 1$;
- $\langle W(t_1) \rangle$ and $\langle W(t_2) \rangle$ are independent of each other for $t_1 \neq t_2$.

The solution of the differential equation 2.18 in time is the MSD of particle in trap as represented in equation 2.15.

Introducing a corner frequency:

$$f_c = \frac{\kappa_x}{2\pi\gamma} \tag{2.19}$$

Equation 2.16 can be written as

$$\dot{x}(t) + 2\pi f_c x(t) = \sqrt{2D}W_x(t) \tag{2.20}$$

and the Fourier transform of equation 2.20 is

$$2\pi(f_c - if)\tilde{X}(f) = \sqrt{2D}\tilde{W}_x(f) \tag{2.21}$$

where $\tilde{X}(f)$ and $\tilde{W}_x(f)$ are the Fourier transforms of $x(t)$ and $W_x(t)$ respectively. Taking the square modulus of both sides of equation 2.21 gives the power spectral density (PSD) of the particle motion at a total time interval of T,

$$P_x(f) = \frac{|\tilde{X}(f)|^2}{T} = \frac{D/2\pi^2}{f_c^2 + f^2} \tag{2.22}$$

which is the form of a Lorentzian function. By fitting the PSD of an optically trapped particle to the above Lorentzian, one can obtain the corner frequency (f_c) or the roll off frequency as shown in Fig. 2.12. Once the corner frequency (f_c) is known, stiffness (k) can be calculated using equation 2.19 (Result for a single trap using SLM is shown in table 2.2 for 1 μm particles).

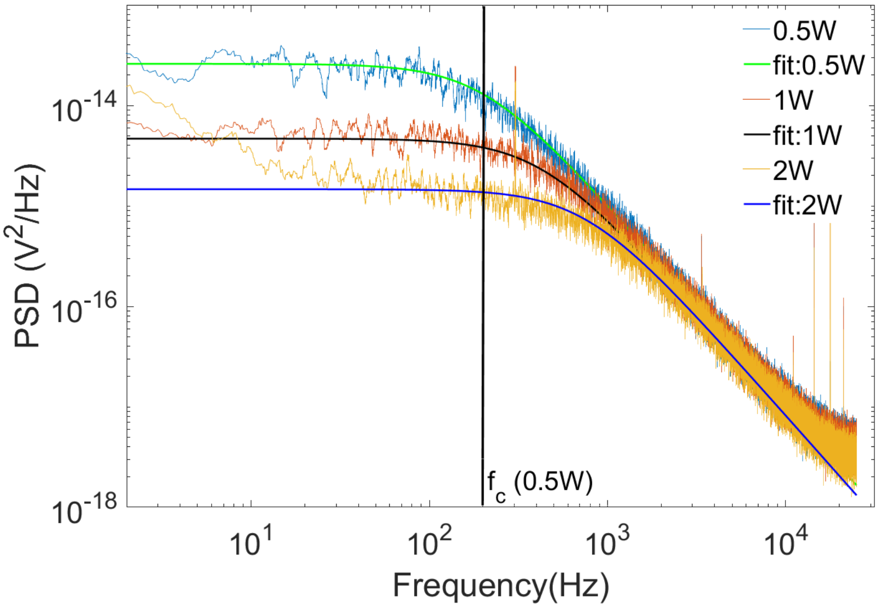

FIGURE 2.12: Power spectral density of 1μm trapped particle using 3 different laser powers.

TABLE 2.2: Measurement of stiffness (5 measurements at each laser power) at 3 different laser powers (SLM) using corner frequency (Bead diameter - 1 μm, Laser wavelength -1064 nm).

Laser Power (W)	**Corner frequency (f_c (Hz))**	**Stiffness (k (pN/μm))**
0.5	200 ± 7	10.5 ± 0.4
1	420 ± 4	22.1 ± 0.2
2	750 ± 9	39.3 ± 0.5

Similar calibration experiments were carried out for 2μm beads using a different higher laser power (Arryx, 5W laser). This high powered laser with higher stiffness is used to trap beads and make an indentation on cells and nuclei. The calibration protocol was similar to that described above. Table 2.3 shows the stiffness as a function of laser power.

TABLE 2.3: Measurement of stiffness (5 measurements at each laser power) at 3 different laser powers (High power trap) using corner frequency.(Bead diameter - 2 μm, Laser wavelength -1064 nm)

Laser Power (W)	**Corner frequency (f_c (Hz))**	**Stiffness (k (pN/um))**
0.5	431 ± 4	34.1 ± 0.5
1	683 ± 6	48.5 ± 0.9
2	1100 ± 2	69.3 ± 0.3

The stiffness values obtained from Power spectrum method (Table. 2.2) for the same laser power is higher compared to that of Equipartition and MSD method (Table. 2.1). This shows that Power spectrum is the ideal choice for calibrating OT as any noise in the system can be isolated and does not affect the stiffness measurement whereas for Equipartition and MSD method the noise is embedded in the data at all time scales, which is the reason for lower values of stiffness.

2.3 Atomic Force Microscopy (AFM)

AFM experiments were conducted at the Physics department of the University of Queensland, Australia. AFM measurements were performed using a JPK Nanowizard II (JPK Instruments, Bruker) mounted on an inverted fluorescent optical microscope (LSM 710, Zeiss) as shown in Fig. 2.13.

FIGURE 2.13: AFM Setup

The Nanowizard II machine was equipped with the CellHesion module that enabled extension of the cantilever movement in the Z direction up to 100 μm. Fig. 2.14(a) shows schematics of the AFM set up to scale, in order to highlight the size of the cantilever relative to the colloidal probe and the sample. The microscope was equipped with a double illumination optical setup, which enables illumination of the top and bottom of the sample at the same time. This allows observation of the sample in a high contrast mode under illumination from above, whilst being able to observe the sample and colloidal probe hidden under the cantilever from below (Bonilla et al., 2015; Yakubov et al., 2016). This enables accurate positioning of the colloidal probe above the centre of the sample. Indentation measurements were performed using long cantilevers (PNP-TR-TL 200 μm), with SiO_2 spheres of 2 μm diameter (Polysciences AG) mounted using a 2 component epoxy glue (UHU Schnellfest, UHU).

Spherical beads were used here instead of a sharp tip to apply a force over a larger surface area with a well-defined contact geometry. The sample was placed in a Petri dish with the culture media and mounted on the temperature-controlled AFM stage. The cantilever was first positioned above the cell surface using a mechanical XY stage, and then the position was further adjusted using an XY piezo stage operated by a manipulation control option in the contact mode. Once positioned, the illumination was switched off to minimise temperature fluctuations. Indentation curves were recorded using driving speeds of about 0.5 μm/s to minimize the impact of hydrodynamic drag that at all times was <5 Å in the deflection equivalent (Vinogradova et al., 2001).

The force measurements were performed at three values of force set point, 300, 500 and 1000 pN, operated in the closed loop mode to minimise hydrodynamic contributions (Vinogradova et al., 2001). Immediately before use, the probes were cleaned in oxygen plasma for 5 min and then mounted and immersed in the experimental cuvette with buffer. The spring constant (k) was determined using the Asylum Research GetReal$^{\text{TM}}$ routine that utilizes a combination of the thermal noise and the Sader methods (Higgins et al., 2006). A glass Petri dish was coated with poly-L-lysine to retain the samples (cells and extracted nuclei - as detailed in the forthcoming experimental chapters) in situ during the indentation. The typical values of spring constant were 0.04 N/m. In a typical experiment, the cantilever was positioned in close proximity to the sample, and a set of force–indentation curves were then recorded. It was also important to control the position of the AFM tip over the samples' apex to ensure that the indentation is normal to the sample surface (Dufrêne, 2001).

Raw force versus distance curves were recorded as a function of the voltage output from the position-sensitive device versus the calibrated z-position of the piezotranslator. The output voltage of the position-sensitive device was converted into the deflection by calculating the slope of the constant compliance line measured against a glass substrate in the same buffer used to record the force indentation curve on sample. The force was calculated by multiplying deflection by the cantilever spring constant. The zero position was determined as the cross-section point of the baseline and the tangent line corresponding to the onset of the indentation curve, where cantilever deflection started to deviate from the baseline. Positive values were attributed to the indentation section of the curve. The apparent separation was calculated by subtracting cantilever deflection from the z-position of the piezotranslator.

Furthur analysis were performed using JPK software to perform baseline subtraction. Indentation force (F) and depth (D) data were then exported and fitted using MATLAB (R2016) to obtain an apparent Young's modulus (E). The Young's Modulus was determined using the classical Hertz contact model (Hertz, 1882).

$$F = \frac{4}{3}\frac{E}{(1-\nu^2)}\sqrt{RD^3} \tag{2.23}$$

where R is the radius of the spherical bead, and v is the Poission ratio (v = 0.4) (Nawaz et al., 2012). This model, which describes indentation of elastic solid objects by a spherical indentor, has been widely used to determine elasticity in cell mechanics studies (Yousafzai et al., 2016; Guz et al., 2014; Nawaz et al., 2012) .

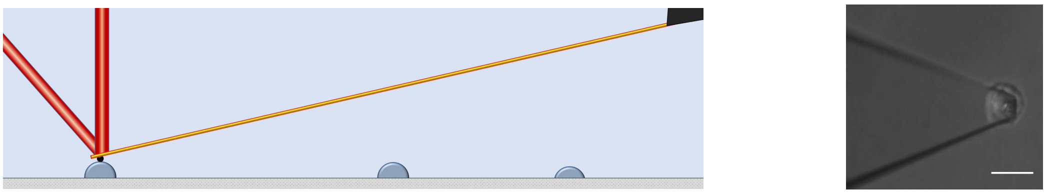
(a) (b)

FIGURE 2.14: AFM indentation. (a) Schematic setup for AFM measurements. Figure shows a cantilever (yellow) with a bead (black) attached at the end, and a laser light (red) deflecting at the end of cantilever. (a) Cantilever with a bead attached at the tip for probing the nuclei. Scale bar - 10μm.

2.4 Micropipette Aspiration (MA)

Micropipette aspiration (MA) is a technique used to to deform and aspirate samples which are micrometer in size. This technique was initially implemented on single cells such as erythrocytes and leukocytes back in the 1970's (Waugh and Evans, 1979; Needham and Hochmuth, 1990). In this technique, a negative suction pressure, ΔP, is applied. This is done by connecting a micro pipette to a water reservoir or a pump. The deformation of the sample is determined from images recorded by using a optical microscope.

2.4.1 General Theory

Different models can be used to quantify the mechanical properties of cells from their shapes during aspiration measurements. Here we describe two models based on previously reported analyses carried out in more conventional MA experiments to quantify cell mechanics (Drury and Dembo, 1999; Hochmuth, 2000). In both cases, we refer to the derived mechanical properties as 'effective' due to the modelling assumptions applied.The first and most commonly used model is the continuum medium model, where the aspirated cell is assumed to be homogeneous, incompressible and mostly spherical in shape (Hochmuth, 2000; Van Vliet, Bao, and Suresh, 2003). In this model, an aspirated cell can be considered a liquid drop, as shown in Fig. 2.15. The pressure difference ΔP as the cell is aspirated into the pipette can be described using the Young - Laplace equation (Shojaei-Baghini, Zheng, and Sun, 2013; Needham and Hochmuth, 1990),

$$\Delta P = 2T_c\left(\frac{1}{r_i} - \frac{1}{R}\right) \tag{2.24}$$

where T_c is the cortical/membrane tension, r_i is the pipette opening radius and R is the radius of the cell outside the pipette. As the suction pressure gradually increases and the aspirated length ΔL increases, three stages are observed: i) $\Delta L < r_i$, ii) $\Delta L = r_i$ and iii) $\Delta L > r_i$. The cell flows into the pipette at suction pressure when $\Delta L > r_i$ at constant velocity(v). The Laplace equation is no longer valid beyond the critical pressure (ΔP_c; when $\Delta L \geq r_i$) when the cell flows into the pipette. In this situation, the viscosity (η) of the cell can be calculated as

$$\eta = \frac{r_i(\Delta P - \Delta P_c)}{6v(1 - \frac{r_i}{R})} \tag{2.25}$$

where R is the radius of the cell outside the pipette when v is measured. With increasing suction pressure beyond the critical pressure for solid-like cells, the equation can be written as,

$$\Delta P = \frac{2\pi}{3}E\frac{\Delta L}{r_i}\phi \tag{2.26}$$

where E is the Young's Modulus for the solid cell and ϕ is a constant with a typical value of 2.1. This value depends on the ratio of thickness of the pipette wall to r_i. The elasticity of the particle is related to its viscosity by

$$E = \frac{3\pi\eta}{\tau} \tag{2.27}$$

where τ is the characteristic relaxation time of the particle.

When a sample starts to be aspirated, it undergoes an initial elastic deformation, as

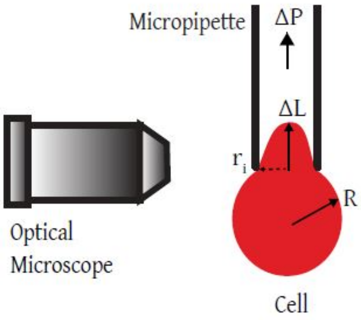

FIGURE 2.15: Schematic of micropipette aspiration

shown in Fig. 2.15, ΔL is measured by optical microscopy using the first video frame in which the nucleus is aspirated by the micropipette tip (e.g. Fig. 5.1(c) (right image)). From this measured aspirated length ΔL, the effective elastic modulus (E) is

$$E = \frac{r_i \Delta P}{\Delta L} \tag{2.28}$$

The second model is based on those developed for viscoelastic particles (Guevorkian et al., 2010) but data analysis is customized for full aspiration of particles into a conical pipette (Gangotra and Willmott, 2019). While conventional MA often uses optical microscopy data to analyse the total aspirated length (L) as a function of time, here only the event duration ΔT, is used. This is obtained from the electrical signal which has better resolution than optical data. At the start of the experiment, a baseline current (I_0) is established and measured. ΔT is defined as the time it takes for the nucleus to pass through the pipette tip constriction, measured as the time during which $I < 0.95 I_0$. Using the geometry of the pipette tip and the sample, the velocity of aspiration (u) can be estimated. The critical pressure required for aspiration to start, related to the surface tension of the sample, is assumed negligible compared to ΔP, and friction is also neglected in this analysis. The effective viscosity (η') of the nucleus is

$$\eta' = \frac{r_i \Delta P}{3\pi u}. \tag{2.29}$$

The viscous and elastic regimes are separated by a constant stress relaxation time (τ), and an effective elastic modulus (E') is obtained using this second model is given by:

$$E' = \frac{3\pi\eta}{\tau}. \tag{2.30}$$

2.4.2 Setup Description and operation

MA experiments were conducted at the Physics Department of the University of Auckland (Gangotra, 2019). The MA setup was built on an antivibration table to reduce mechanical perturbations. A Custom-made mount was made to hold on the pipette, attach the pipette to a Ag/AgCl electrode, and connect the electrode to the electrometer. The mount was designed to be connected to 3-D movement piezo actuators for precise displacements in the range of nm to μm. A manual stage with X-Y movement was used to hold the substrate which was submerged in the electrolyte bath for coarse movement of the sample. Two microscope objectives were used in vertical and horizontal directions as shown in the schematic Fig. 2.16(a) to image the pipette and sample, respectively. A pressure reservoir was used to collect the aspirated fluid, so the pipette pressure is controlled by a pressure sensor and the pressure pump (apply -ve pressure). To reduce electrical noise, the apparatus was shielded with a Faraday Cage as shown in Fig. 2.16(b). Detailed components and their explanations of the setup are listed in Appendix B.2.

Micropipettes were fabricated from borosilicate glass capillaries (QF-100-50-7.5, Sutter Instruments) using a CO_2 laser pipette puller (P-2000, Sutter Instruments). The micropipettes had a (6.5 ± 0.5) μm inner diameter. To reduce adhesion, each pipette was immersed in a silanising agent (Sigmacote, Sigma Aldrich) for 1–2 s and left to air dry overnight to form a uniform surface coating at the tip. Fig. 2.17 shows the image analysis and current response as the particle is being aspirated. During the experiment, a micropipette was backfilled (Hansma et al., 1989) and immersed in an electrolyte bath filled with 3 mL 1× PBS. Once the pipette was affixed in place, 50 μL of a solution containing samples (typically nuclei isolated from MCF7 cells) was transferred to the electrolyte bath near the pipette tip. To begin each experiment, a potential of 0.1 V and suction pressure (ΔP) of 25-200 mbar (2.5-20 kPa) was applied using the electrometer and pressure pump respectively. An electrical current between the electrodes (I) was recorded simultaneously with an optical microscopy video focused on the pipette tip (Fig. 5.1(c) (Top - right image)). In this study, aspiration events

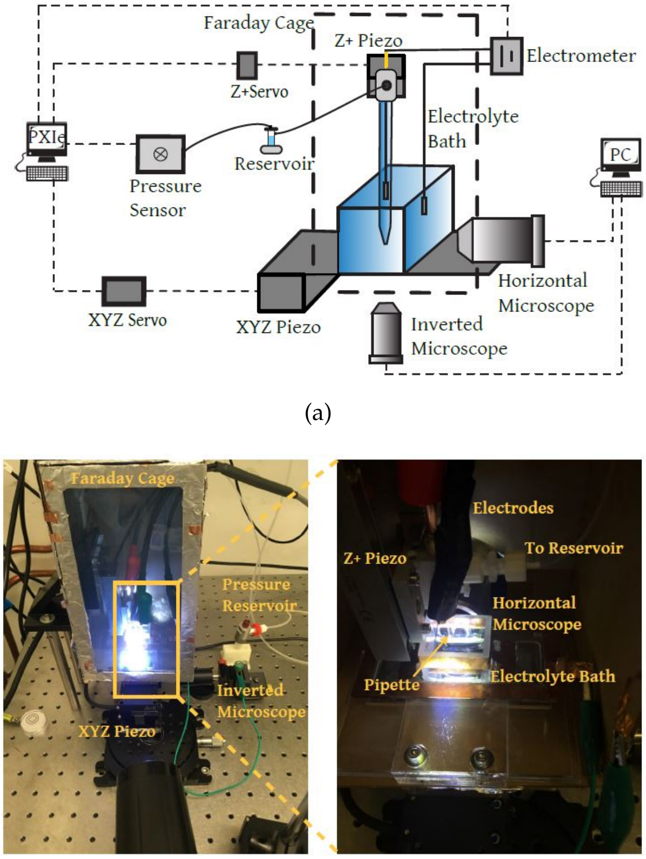

(a)

(b)

FIGURE 2.16: (a) MA apparatus setup. (b) MA apparatus photos with an overall view of the apparatus (left) and a close up image taken inside the Faraday cage (right).

differed from conventional MA experiments because each event consisted of a sample being deformed and additionally completely drawn through the pipette tip. Each experiment was run for 60-90 s, during which multiple events were captured. The micropipette was replaced between experimental runs when it became obstructed or clogged. It was of interest to measure the duration of each aspiration event. The electrical data were used for this because electrical signals were sampled at 300 Hz, whereas optical microscopy videos were captured at 24 frames per second. The electrical current decreases as the sample particle enters the tip and recovers after it traverses the tip, clearing the ionic transport pathway. Aspiration event times (T) were typically 0.5-2 s.

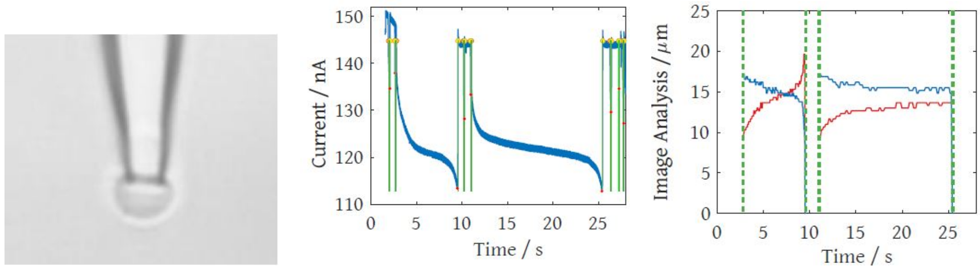

(a) (b) (c)

FIGURE 2.17: Synchronisation of microaspiration current and optical microscopy data. (a) Aspiration of 10-20 μm polymer particles with a 8μm diameter pipette. (b) Current response for the aspiration. Green lines indicate the start and end of aspiration events. (c) Synchronised image analysis from image stacks of aspiration events. Red lines represent the aspirated lengths, blue lines represent the diameter of the polymer particle outside the pipette and green lines indicate the start and end of the aspiration events determined from the current response.

2.5 Mechanical Rheometer

Bulk Rheology measurements were also carried out where useful to compare with the measurements from microrheological techniques.

2.5.1 Experimental method

A frequency sweep was performed to characterize the rheological properties of PEO solutions (described in more detail in the next chapter). The frequency is varied while the amplitude of the shear stress is kept constant. Measurement parameters for frequency sweeps are listed in table 2.4:

TABLE 2.4: Frequency sweep.

Temperature	20 °C
Strain %	1%
Angular frequency	0.1-250 rad s^{-1}
Points per decade	10
Conditioning Time	5 s
Sampling Time	5 s
Preshear	1 rad s^{-1} for 30 s

2.5.2 Conclusion

In this chapter the methods and the calibration that are required for this thesis were described in detail. OT is the major technique among all of them and has used extensively in the entire thesis. AFM and MA techniques were used specifically for nuclei mechanics in chapter 5. We now move our attention to results obtained using these techniques.

Chapter 3

Microrheology of Polyethylene oxide (PEO)

After a thorough discussion of the many techniques utilized in this thesis in chapter 2, the next goal was to implement and understand the use of some of these microrheological techniques in complex fluids. This chapter focuses on using basic passive and active techniques to study Polyethylene Oxide solutions (model viscoelastic solutions). Particular attention was paid to the calibration of OT in a viscoelastic media using an active microrheology approach.

3.1 Introduction

Complex fluids like gels, polymer solutions, and bio-materials are often 'squishy' in nature and exhibit mechanical properties that vary with length and time scale. The response of these materials to induced shear strain gives us information about the structure of the material. For instance, solids store energy and are elastic, while fluids dissipate energy and are viscous. Complex fluids exhibit both these features and are viscoelastic in nature.

A traditional way of understanding these complex materials is by using a mechanical rheometer, where the stress response of the material to an applied oscillatory strain determines the complex modulus $G^*(\omega)$. The real part of the complex modulus $G'(\omega)$ measures the ratio of the in phase response of the medium to the applied oscillatory strain which determines the elastic component of the material. The out of phase response is given by the imaginary part of the complex modulus $G''(\omega)$ which determines the viscous component of the material. These two components are related to each other by the Kramer-Kronig relations (Chaikin, 1995).

Over a couple of decades, the microrheology technique has been extensively used to probe viscoelastic materials (MacKintosh and Schmidt, 1999; Cicuta and Donald, 2007b; Waigh, 2005a). The advantage is that it requires very small sample size, typically a few hundred microlitres of samples compared to milliliters of sample required for conventional mechanical rheometer measurements. Hence, the application can be particularly useful for very costly materials or biological samples (Mas et al., 2013).

To understand and compare conventional rheology and microrheology techniques, firstly passive microrheology experiments were carried out (where passive microrheology is the study of system properties using probe particle movements under the influence of only thermal fluctuations) and secondly active microrheology is performed (concerned with observing how the system responds to an externally applied force).

3.2 Materials and Methods

The experimental setup used is similar to those described in sections 2.2.3 and 2.1.1. Polyethylene oxide solutions are used as the model viscoelastic media. PEO is a viscoelastic polymer that can be used to prepare solutions which are homogeneous and not charged. 900 kDa PEO dry powder (Acros Organics) was mixed in milliQ water along with fluorescent probe particles (0.05 vol%, Poly Sciences Polystyrene, 1.0 μm, 2.6% Solids-Latex) for 3 days to make a homogeneous solution. PEO starts to exhibit viscoelasticity at concentrations higher than the overlap concentration, c*. The overlap concentration is approximately 0.16 wt% for the 900 kDa PEO samples. (Dasgupta et al., 2002). Solutions were prepared at concentrations of 2 wt% and 4 wt%, 14 and 25 times the overlap concentration respectively, to ensure significant viscoelasticity.

The microrheology of polyethylene oxide was measured by MPT and OT, with a combination of camera and QPD measurements as described in sections 2.1 and 2.2 respectively.

3.3 Results and Discussions

3.3.1 Passive Microrheology of Polyethylene Oxide

The MSD measured using a QPD and a CCD camera, for particles suspended in 2 wt% and 4 wt% PEO solutions are shown in Figs. 3.1 and 3.2. The slope of MSD data on a log-log plot at longer time scales approaches one, indicating a viscous behavior whereas at early lag times it is approximately equal to 0.56 and 0.42 for 2 wt% and 4 wt% respectively indicating predominantly elastic behavior which is as expected for a polymer solution in the semi-dilute regime and is in fair agreement with previous work (Dasgupta et al., 2002).

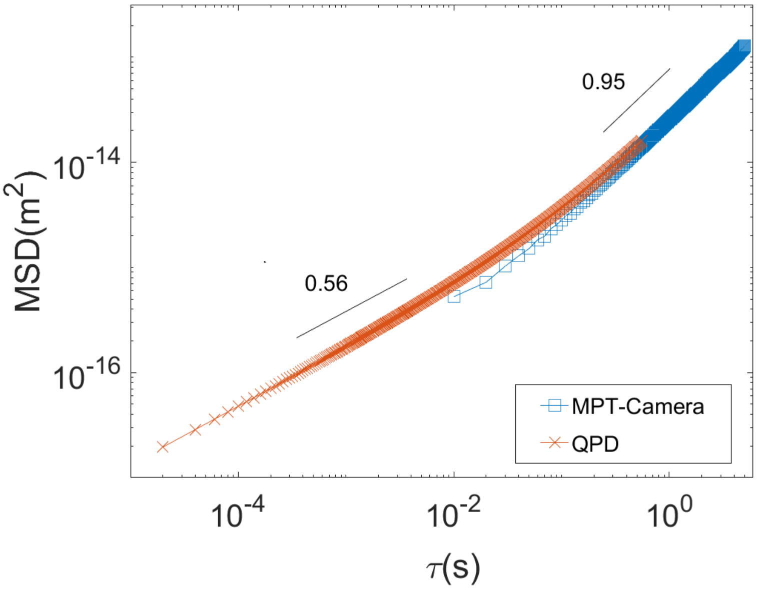

FIGURE 3.1: MSD of 2 wt% PEO. Double power law fit of exponents 0.56 (shows elastic response of polymer) and 0.95 (shows viscous behavior)

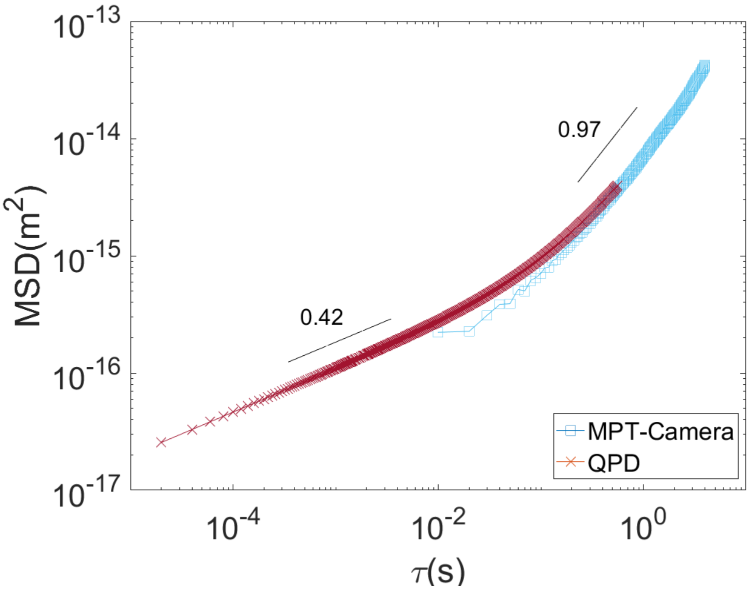

FIGURE 3.2: MSD of 4 wt% PEO. Double power law fit of exponents 0.42 (shows elastic response of polymer) and 0.97 (shows viscous behavior)

To compare with bulk rheology, the MSD data of PEO solution has to be represented in a frequency dependent regime. The MSD can be related to viscoelastic moduli using the Generalized Stokes-Einstein Relationship (GSER). Among the many methods, the Mason and Weitz's numerical method (described in section 2.0.1) is possibly the most popular method, due to its ability to handle noise and its simplicity (Mason, 2000). The plots in Figs. 3.3 and 3.4 show the comparison of moduli from microrheology using the more expansive QPD data to the bulk rheology measurements for 2 wt% and 4 wt% PEO respectively.

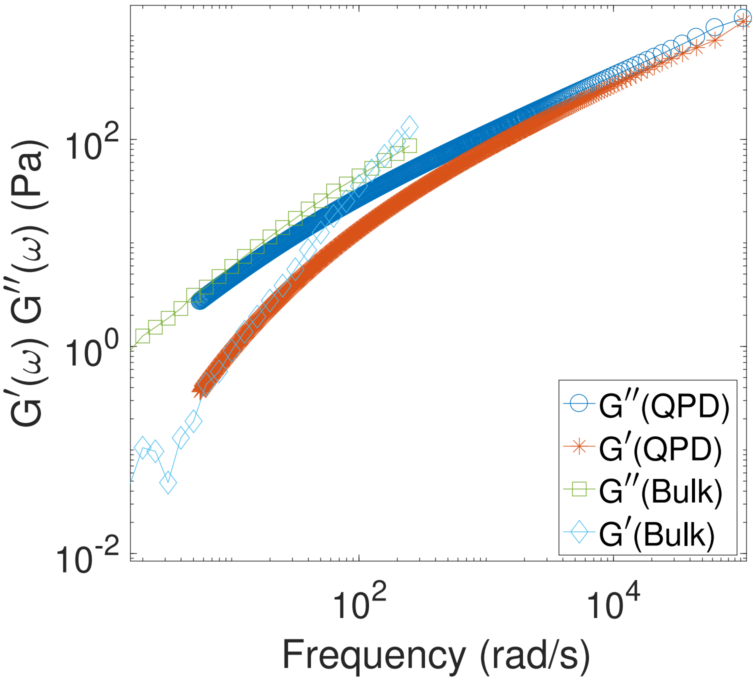

FIGURE 3.3: Elastic (G') and viscous (G'') moduli for 2 wt% PEO

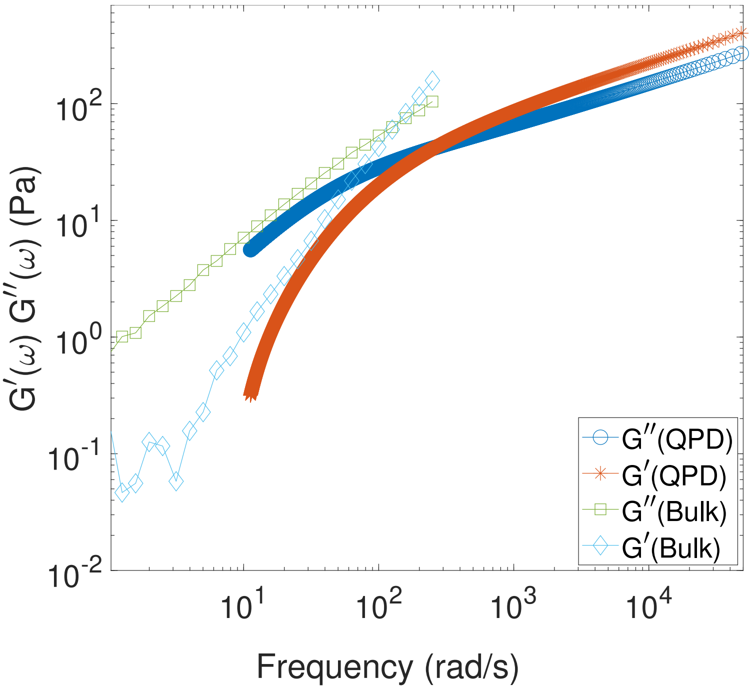

FIGURE 3.4: Elastic (G') and viscous (G'') moduli for 4 wt% PEO

Using the QPD, the moduli were obtained over ∼4 decades in frequency with fair agreement with bulk rheology measurements. QPD data shows that the cross-over frequency is shifted to lower frequency for 4 wt% PEO, as compared to 2 wt% PEO, showing the higher elastic behavior for higher concentration of PEO.

3.3.2 Active microrheology of PEO

In active microrheology techniques, the motion of the probe particles are driven by externally oscillating the stage or by translating an optical trap containing the probe particle (Velegol and Lanni, 2001b; Valentine, Dewalt, and Ou-Yang, 1996). This technique is similar to the mechanical rheometer where it is possible to drive the particle with small or large amplitudes, providing an insight into non-linear regimes, as well as linear response. To extract the viscoelastic moduli characterizing the PEO, we need to determine the stiffness of the trap in a viscoelastic solution (PEO).

3.3.2.1 Calibration of Optical Tweezers in PEO

In order to use OTs as a force measuring tool inside a viscoelastic medium, it is crucial to perform exact force calibration. The Brownian motion of particles in a viscoelastic media differs from that in a viscous media. In a viscoelastic medium, the restrictions of the motion of particles which is usually related to the trap have an additional contribution from the elasticity of the material. Hence we cannot determine the calibration using power spectrum method as shown in section 2.2.5.2, as the physical characteristics of the medium such as viscosity and elasticity are often unknown.

To calibrate in such a complex environment, passive and active techniques can both be applied using OT. In the passive part, the Brownian motion of a trapped particle in the viscoelastic media is observed and the power spectra is extracted. In the active part, the trap position is moved using a piezo stage and the response of the trapped particle is tracked. The combination of passive (undriven) and active (driven) parts can be used in concert to give an estimate of the stiffness of the trap in a viscoelastic media(Fischer and Berg-Sørensen, 2007; Fischer et al., 2010). The idea is described in Fig. 3.5.

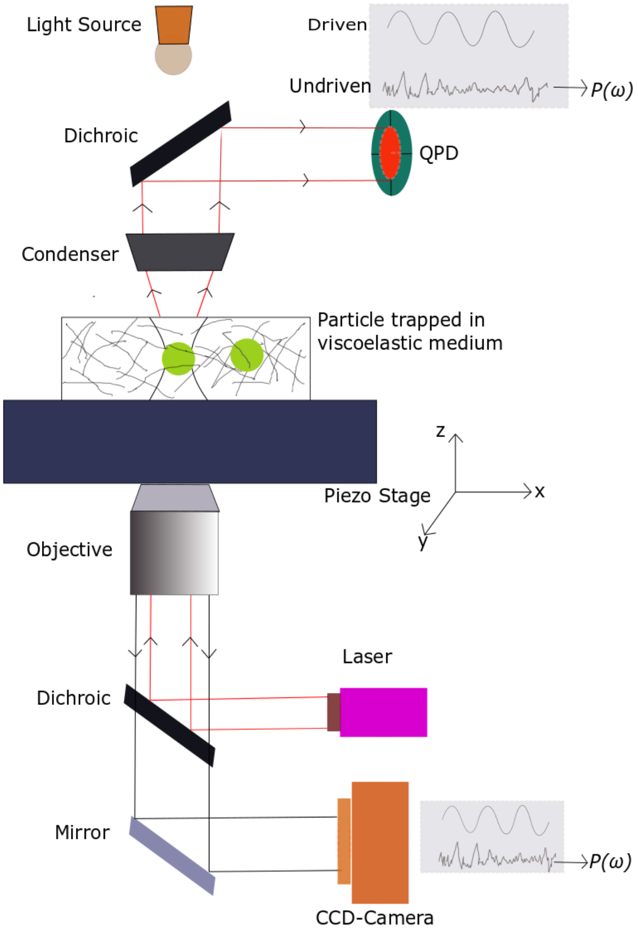

FIGURE 3.5: Passive and active microrheology setup. In passive(undriven) experiments, the particle performs a thermally induced stochastic motion. In active(driven) experiments, the sample is oscillated in controlled fashion by a piezo stage

The discussion so far has been focused on using equation 2.6 to model the motion of a trapped particles in a fluid environment subjected to friction, a conservative force, optical force and a thermal random force. This framework is ideal in the case of Newtonian fluids like water and glycerol. However, this framework cannot be applied to a viscoelastic (non-Newtonian) fluids. The friction term is coupled in a more complicated way to the environment. In order to extend the equation 2.16 to viscoelastic media (non-Newtonian fluids), a generalized Langevin equation has been proposed (Mason and Weitz, 1995). The passive part is described as:

$$m\ddot{x}(t) + \int_0^t \zeta(t-\tau)\dot{x}d\tau + \kappa x(t) = \xi(t) \tag{3.1}$$

where ζ, the time dependent memory function, represents the viscous damping. The middle term in the left hand side of equation 3.1 is called the memory friction, which captures the effect of energy stored in the medium during time evolution. For the active part, the stage is oscillated sinusoidally with driving frequency ω. The generalised Langevin equation will be similar to equation 3.1, but now with an extra term accounting for moving the stage. The equation of motion for a stationary trap and moving stage is given by:

$$m\ddot{x}(t) + \int_0^t \zeta(t-\tau)(\dot{x}(t) - \dot{x}_s(t))d\tau + \kappa x(t) = \xi(t) \tag{3.2}$$

where $\dot{x_s}$ represents the velocity of the stage. The integral term now contains the past velocities of the particle relative to the medium. The theoretical derivation of combining the active and passive parts for quantitative measurements has been described in (Fischer et al., 2010)(Fischer and Berg-Sørensen, 2007). Here, only the equations necessary for data analysis are used. The main principle is a linear response theory which connects a response function of the medium, $\chi(\omega)$, to the average Fourier transform of an observed position x of the tracer particle $< \tilde{x}(\omega) >$ and the Fourier-transform of an external force F_{ext}, $\tilde{F}_{ext}$, given by

$$< \tilde{x}(\omega) >= \chi(\omega)\tilde{F}_{ext}(\omega) \tag{3.3}$$

3.3.2.2 Passive measurements

In a series of passive measurements, time series of the position of a trapped particle (undriven), $x_p(t)$ were recorded for time T_{msr}, where T_{msr} is the total measurement time. Using this time series, the power spectrum $P(\omega)$ of the position fluctuation is calculated as :

$$P(\omega) = \lim_{T_{msr}\to\infty} \frac{< |\tilde{x}_p(\omega)|^2 >}{T_{msr}} \tag{3.4}$$

where $\tilde{x}_p(\omega)$ is the Fourier transformed position of the trapped particle and $\omega = 2\pi f$ is the angular frequency (f is the normal frequency). The position of the trapped particle in polyethylene oxide is recorded both by using a quadrant photodide (QPD) and a CCD camera as shown in Fig. 3.5.

In the passive measurements, a 5 s time series of the position of the trapped particle (undriven), was recorded with a CCD camera with a frame rate of 500 fps.

3.3.2.3 Active measurements

In active measurements, the system was driven by sinusoidally oscillating the piezo stage in the x-direction with frequencies between 1 and 15 Hz, in a PEO solution (2 wt%).The stage was moved for approximately 5 to 10 s and the motion of the bead was recorded using CCD camera. The stage movement was also monitored using a particle adjacent to the trapped one as illustrated in Fig. 3.5 (The free bead adjacent to trapped bead). Recordings of x_p^{dr} and $x_s(t)$ were performed for 5 s at a frame rate of 500 fps, where x_p^{dr} is the position of trapped particle when the stage is driven and $x_s(t)$ is stage position.

Hence, the position of the stage can be described by $x_s(t) = A_s sin\omega t$, where A_s is the amplitude of stage motion. The position of the driven trapped particle $x_p^{dr}(t)$ was recorded simultaneously. Using relations 3.1, 3.2 and 3.3, the active spectrum for stage driving $\tilde{R}_s(\omega)$ is defined as (Fischer and Berg-Sørensen, 2007):

$$\tilde{R}_s(\omega) = \frac{x_p^{dr}(t)}{i\omega\tilde{x}_s(\omega)} \tag{3.5}$$

The active spectrum can be more conveniently calculated via the phase difference $\Delta\phi$ between the phase of the stage driving, ϕ_s, and the phase of the trapped particle, ϕ_p:

$$\Delta\phi = \phi_p - \phi_s \tag{3.6}$$

and the active spectrum is given by:

$$\tilde{R}_s(\omega) = \frac{A_p}{\omega A_s}(sin\Delta\phi - icos\Delta\phi) \tag{3.7}$$

where A_s is the amplitude of the stage driving and A_p is the amplitude of the particle response. Hence, using the above active and passive measurements, the spring constant, κ, of the trap can be found:

$$\kappa - \omega^2 m = 2k_B T\frac{Re(\tilde{R}(\omega))}{P(\omega)} \tag{3.8}$$

If the stage is driven at a particular frequency ω_s, then after inserting the real part of equation 3.7 into equation 3.8, the relation becomes:

$$\kappa - \omega_s^2 m = \frac{2k_B T}{P(\omega_s)} \frac{A_p}{\omega_s A_s} sin(\Delta\phi) \tag{3.9}$$

In equation 3.9, m is the mass of the particle. The particle size is not required. Also, in these experiments the frequency and the mass is very small, hence, the term $\omega^2 m$ in equation 3.9 can be neglected (Mas et al., 2013). This allows the trap strength to be properly calibrated in a viscoelastic fluid.

3.3.2.4 Experimental results using 2 wt% PEO

Combining the active and passive measurements described above, trap stiffness was measured using a fixed laser power (2 W) with driving frequencies ranging from 2 to 15 Hz.

Stepwise calibration procedure:

(a) Passive recording of a particle ($x_p(t)$) in a trap. This is the undriven part as shown in Fig. 3.5. Power spectra are determined from this passive recording as described in section 3.3.2.2.

(b) Active driving and recording as illustrated in Fig. 3.6.

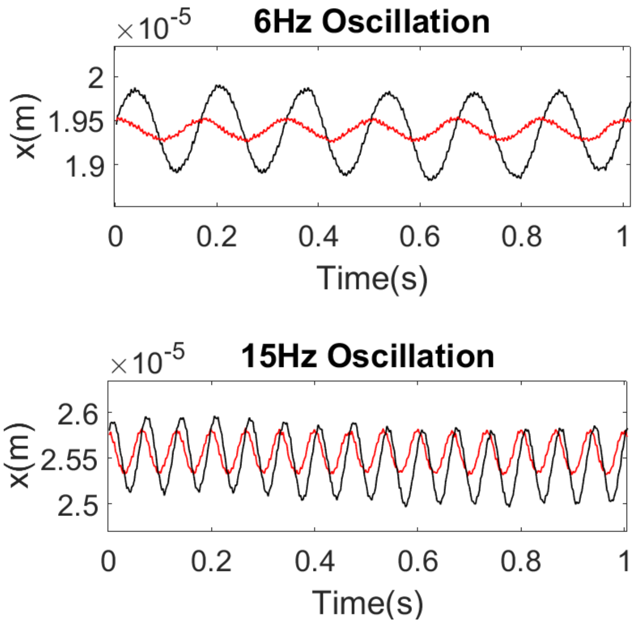

FIGURE 3.6: Figure shows sinusoidal oscillation of stage (*black*) and response of optically trapped particle (*red*) at 6Hz and 15Hz.

(c) The phase difference (using equation 3.6) and amplitude ratio ($\frac{A_p}{A_s}$) are obtained for different oscillation frequency and are shown in Fig. 3.7. The active spectrum $\tilde{R}(w)$ is then recovered using equation 3.7. As seen from Fig. 3.7, the phase difference between stage driving and bead response (Fig.3.6) decreases while amplitude increases with driving frequency.

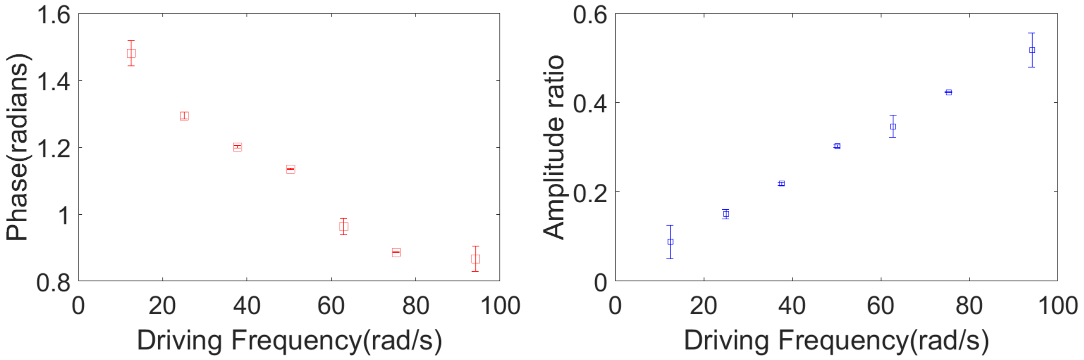

FIGURE 3.7: Phase shift and amplitude ratio for active measurements. Error bar indicates standard error (SE).

(d) Following (a), (b) and (c), the trap stiffness of the particle is determined using equation 3.9. Fig. 3.8 shows stiffness (κ) versus oscillation frequency (ω), error bars represents standard error (SE) for a similar system. Within the error bars, the data are consistent with κ being independent of driving frequency and having an average value of $\kappa = (33 \pm 2.9)$ pN μm^{-1}. The measured values of κ are more precisely obtained than given in literature $\kappa = (44.9 \pm 13.5)$pN μm^{-1} (Mas et al., 2013).

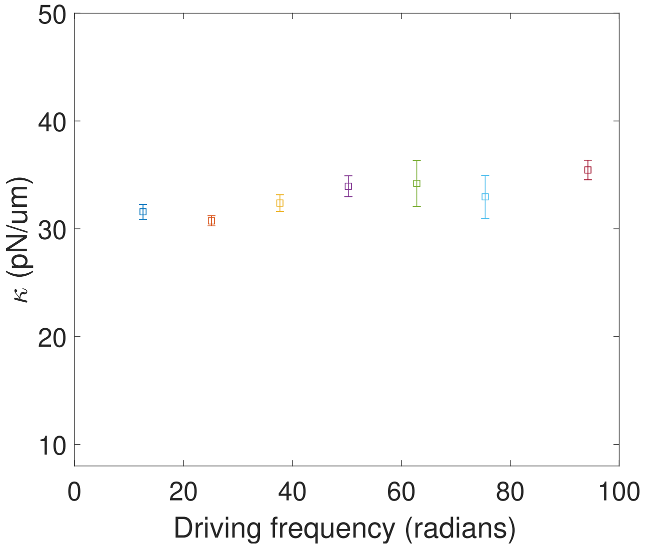

FIGURE 3.8: Plot of stiffness versus oscillation frequency. The error represents standard error (SE) (n = 10).

The experimental method is already described in section 3.3.2.3. The equation of motion for a sinusoidally moving trap is described in equation 3.2. By measuring the phase difference of the particle and stage displacement shown in 3.7, the complex modulus (G^*) can also be determined along with the trap stiffness (κ) in the viscoelastic media. Using the equations for active and passive measurements described in sections 3.3.2.2 and 3.3.2.3, the viscoelastic modulus can now be extracted (Mas et al., 2013):

$$G^*(\omega) = \frac{i\omega}{6\pi r}(\kappa - \omega^2 m)\frac{\tilde{R}_s(\omega)}{1 - i\omega\tilde{R}_s(\omega)} \tag{3.10}$$

where r is the radius of the particle, κ is the stiffness which is determined using equation 3.9 and $\tilde{R}_s(\omega)$ is the active spectrum of the stage driving, determined using the equation 3.7.

3.4 Conclusion

This chapter highlights the ability of microrheology techniques to measure the viscoelastic properties of simple flexible polymer solutions that are not permanently cross-linked. The viscoelastic spectra obtained using passive microrheology (using the CCD for MSD measurements over a large frequency range) agrees fairly well with bulk rheology measurements and extends them to higher frequencies. Using a QPD, the range of viscoleastic spectra for passive microrheology extends over 4 decades. The results show that the passive microrheology experiment works well when applied to uncross-linked polymer suspensions. Calibration of the OT in milli-Q water is explored rigorously in the literature, however the calibration in viscoealstic media is much less explored. In this chapter, calibration of OT in viscoelastic media is achieved using an oscillating piezo stage to move the probe particles in the viscoelastic medium, which is a prerequisite step to perform active microrheology. Further experiments were not performed as this work was mainly undertaken to get a better handle on the OT setup and the ideas needed to probe biological samples, to which we now switch our attention.

Chapter 4

Mechanical properties of MCF-7 cells

Moving from standard viscoelastic systems to a biological system of interest, this chapter focuses on using OT to understand how the mechanical properties of MCF7 breast cancer cells are altered when the amount of heterochromatin protein 1α (HP1α) they express is reduced. This research was carried out in collaboration with Dr. Tracy Hale (Chromatin research group, Massey University). Since OT forces are in the range of 1 - 100 pN and the typical trap stiffness varies from 1 - 100 pN/μm, it makes an ideal technique for probing these cells. Firstly, the Young's modulus was obtained by performing cell indentation longitudinally (from the top of cells sitting on a polylysinated surface), moving the cell toward an optically trapped bead. Secondly, the membrane tension was obtained by pulling a membrane tether from the cells. In all cases, the results were compared between control and HP1α depleted cells.

4.1 Introduction

Cells are considered as the basic building blocks of tissue. They are a dynamic system capable of sensing mechanical stimuli within their environment and converting them into biochemical signals. Cells also constantly generate force when they crawl and contract and in doing so, remodel their structural stiffness in response to changes in their physical environment. Hence, understanding the mechanics of cells is important to understanding cellular functions such as differentiation, motility, migration, and invasion. Recently, the relationship between cancer cell invasiveness and cell mechanics has garnered much interest, encouraging physicists, mainly from areas like soft matter and statistical physics, to work in tandem with biologists. Various techniques have been used to characterize the mechanical properties of the cells, described in table 1.1.

4.1.1 Overview of the MCF7 cell line and the knockdown of HP1α protein

MCF7 is a human breast cancer cell line derived from a patient with metastatic breast cancer cells in 1970 by Dr Soule of the Michigan Cancer Foundation, Detroit, MI (Levenson and Jordan, 1997). Metastasis is the primary cause of death in breast cancer patients as reported in global cancer statistics (Torre et al., 2015). In metastatic disease, the cell leaves the primary tumor, invades the surrounding tissue, and finally infiltrates other tissues via the circulatory system (Denais and Lammerding, 2014). Before a cell can invade other tissues, it has to squeeze through dense interstitial space and narrow capillaries. Considering that the nucleus is the largest organelle in MCF7 cells (shown by the immunofluroscence confocal microscopy in Fig. 4.1 - Control), it must become malleable and deformable enough to pass through the narrow tissue constrictions. Hence, the mechanical properties of the cell nucleus, its connection to the cytoskeleton and ultimately to the cell membrane can all play a major role in the efficiency with which the cell can perform metastasis.

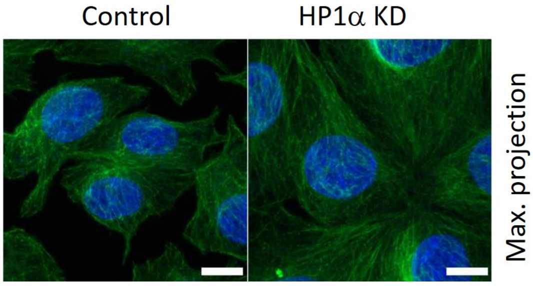

FIGURE 4.1: Immunofluorescence confocal microscopy of MCF7 71 control and MCF7 HP1α KD cells stained with DAPI (blue) to detect DNA and an antibody against α-tubulin (green, mouse monoclonal, ThermoFisher Scientific A11126). Representative images of maximum intensity projection of z stack are shown. Scale bars - 10μm.

Research in cancer cell mechanics has become focused on understanding the stiffness of the cell cytoskeleton, a structure mostly comprising of actin filaments and micro-tubules structures and its interaction with the intermediate filaments (Hu et al., 2018; Xu et al., 2012; Hayashi and Iwata, 2015). The eukaryotic nucleus is defined by the nuclear envelope, which is composed of the outer nuclear membrane and inner nuclear membrane. Lining the inner nuclear membrane is the lamina, a proteinaceous layer comprised of separate but interconnected intermediate filament networks of A-type lamin (A and C) and B-type lamin (B1 and B2) proteins (Kumar, Sengupta, and Bickmore, 2020; Dechat et al., 2008; Shimi et al., 2008; Holaska, Wilson, and Mansharamani, 2002). This barrier houses the genome, where DNA is wrapped around histone proteins to form chromatin fibres undergoing further levels of folding to create domains of highly condensed transcriptionally silent heterochromatin, and domains of less compact transcriptionally active euchromatin (Pombo and Dillon, 2015; Janssen, Colmenares, and Karpen, 2018). This compartmentalisation of the genome determines patterns of gene expression and thus cell identity.

Heterochromatin protein 1α (HP1α) maintains the highly condensed portion of the genome and tethers to the inner nuclear membrane as shown in fig. 4.2. HP1α is an architectural protein that forms and maintains compact domains of heterochromatin (Grewal and Jia, 2007; Ryan and Tremethick, 2018), and contributes to the sequestration of heterochromatin at the nuclear periphery through its interactions with proteins embedded in the nuclear membrane and lamina (Grewal and Jia, 2007; Polioudaki et al., 2001; Kourmouli et al., 2001; Poleshko et al., 2013). This network of interactions between the nuclear envelope, underlying the lamina and the adjacent heterochromatin, ensures both nuclear and genomic integrity. In the poorly invasive breast cell MCF7 line, constitutive knock-down (KD) of HP1α has been shown to increase the ability of cells to move through a three-dimensional extracellular matrix. The introduction of HP1α into highly invasive MDA-MB-231 breast cancer cells, with low endogenous levels of HP1α, suppresses their invasive potential *in vitro* (Norwood et al., 2006; Kirschmann et al., 2000). These findings are supported by the correlation of reduced HP1α expression with the onset of malignant cell invasion in many solid tumours, including those of the thyroid and breast (Tretiakova et al., 2014; Contreras, Gutierrez, and Hale, 2010; Kirschmann et al., 2000).

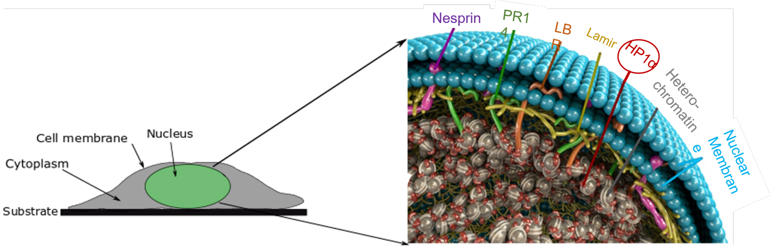

FIGURE 4.2: Schematic of the nuclear periphery. The red circle denotes the HP1α protein.

This chapter investigates the hypothesis that reduction of HP1α alters the mechanical properties of MCF7 cancer cells.

4.1.2 Indentation experiments using Optical Tweezers

Our understanding of the stresses and deflections arising when a bead indents a cell uses a classical theory of how two solids in contact deform. In 1897, Heinrich Hertz deduced theoretical solutions to different contact geometries of two elastic bodies, in what was to be known later as the field of contact mechanics (G, 1896). This study had practical applications in different fields such as the design of dental prostheses, hardness testing, wear and impact damage of engineering ceramics, nano-indentation on cells, etc (Fischer-Cripps, 1999). AFM technique is the most widely used technique for nano-indentation of living cells (Chen, 2014). Here, OT is used for indenting cells which represents a complementary tool. Chapter 5 focuses on the use of multiple techniques to examine nuclear mechanics and in that context the pros and cons of each method are discussed in detail.

4.1.2.1 Previously reported findings using Optical Tweezers

Using OT techniques for indentation measurements is relatively new compared to AFM. Different configurations have been developed to perform mechanical measurements on cells using OT as shown in Fig. 4.3. Fibronectin coated beads trapped by OT at opposite sides of the cell were moved towards the cell in an oscillatory or linear motion (Bacabac et al., 2008; Falleroni, Torre, and Cojoc, 2018) to perform nano indentation (Fig.4.3(a)). Cells have been indented axially (from the top of cells attached to a polylysinated coverslips)(Yousafzai et al., 2016) similar to AFM by moving the cell towards the fixed trap (Fig.4.3(b)). In cases where the cell is not prohibitively spread on the surface, the indentation can also be performed laterally (from the side), where the sample or the trap is moved along the image plane as shown in Fig.4.3(c).

For the configurations mentioned above, different models have been used to extract the cell mechanical properties from force - indentation measurements. The most commonly used model for AFM and OT indentation studies is the Hertz model (Bacabac et al., 2008; Yousafzai et al., 2016; Nawaz et al., 2012). This model assumes that the cell is a homogeneous elastic object and that the size of the indentation is smaller then the size of the probe. Under this assumption, the velocity-dependent viscous components are omitted and the cell can be described by just two parameters, the Poisson ratio v and Young's modulus E. The Poisson ratio is defined as the negative transverse to longitudinal strain ratio, which is a measure of cell's compressibility. The Young's modulus is a direct estimation of cell stiffness (Arbore et al., 2019; Bacabac et al., 2008).

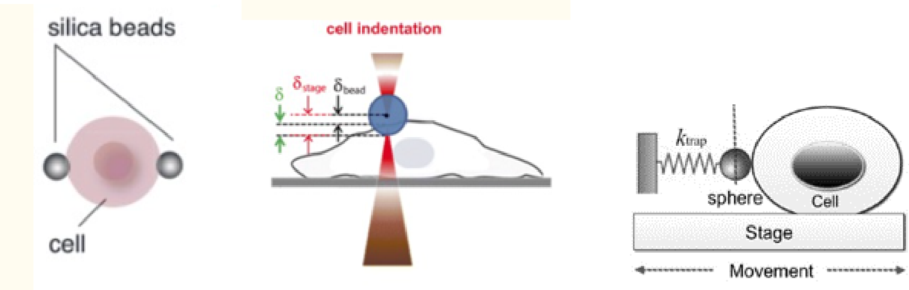

(a) (b) (c)

FIGURE 4.3: Different configurations of Indentation (a) Schematic of a rounded red blood cell/osteocyte cell being indented by silica beads using oscillatory trap. Figure extracted from Arbore et al., 2019. (b) Schematic of the experimental procedure where the stage is displaced upwards by δstage so the cell and bead can interact. Figure extracted from Arbore et al., 2019. (c) Schematic of lateral indentation when cell is moved by piezo stage towards a fixed trap. Figure extracted from Zhou et al., 2014.

4.1.2.2 Qualitative description of Hertz contact model

Here, the contact between a rigid indentor and a elastic specimen is of particular interest. The shape of the indentor may be conical, spherical or cylindrical. The interactions between different geometries and the elastic specimen are termed as 'Hertzian contact'. To understand the interaction of spherical bead and cells, the most well-known scenario is the contact between a rigid sphere and an elastic half sphere. A rigorous formulation of this contact problem is described in the book by Valentin Popov (Popov, 2017). Here we consider a qualitative estimation for ease of understanding the Hertz equation between a rigid sphere of radius ’R’ and an elastic half space. The assumptions in the half space approximation are that i) Surfaces are infinitely large half-spaces, ii) Pressure profiles are parabolic (eg., sphere, ellipse or a cylinder), and iii) Strain is small compared to the size of the probe and the indentor is not deformable (Popov, 2017).

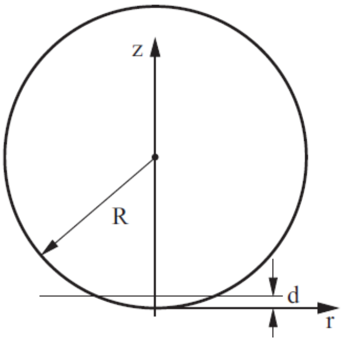

FIGURE 4.4: Hertz contact problem. Image taken from Popov, 2017. Figure shows a rigid sphere of radius ’R’ which on contact with surface, produces a penetration depth of ’d’, with a contact radius of $\sqrt{2Rd}$.

On contact with the surface, the elastic sphere has a penetration depth ’d’, a contact radius $\approx \sqrt{2Rd}$, and a contact area, A, given by

$$A = \pi a^2 \approx 2\pi R d \tag{4.1}$$

The order of magnitude of the elastic deformation can be estimated to be $\varepsilon \approx \frac{d}{2a}$. The magnitude of stress can then be of the order of $\sigma \approx E\frac{d}{2a}$, where E is the Young’s modulus. This gives the force as

$$F = \sigma A \approx \frac{Ed}{2a}\pi a^2 \approx \frac{Ed}{2}\pi\sqrt{2Rd} = \frac{\pi}{\sqrt{2}}E\sqrt{Rd^3} \tag{4.2}$$

which shows that the force is proportional to $d^{3/2}$, comparable to the exact Hertz equation 2.23.

4.1.3 Pulling tethers from the cell membrane

The technique of extracting membrane tethers has been widely used to measure lipid bilayer mechanics in many systems such as synthetic vesicles, neuronal growth cones and eukaryotic cells. The first membrane tether pulling experiments were performed on red blood cells (RBC) in 1970 using a micropipette. Currently, OT and AFM techniques are also being widely used for tether extraction. However, OT is the most widely used technique for adherent cells, as it has an ideal force range compared to other techniques (Moeendarbary and Harris, 2014).

When a flat lipid membrane is grabbed and pulled by a point force, this will result in a cone-like structure forming, eventually giving rise to a tube centered around the point of application of the force applied. This tube is formed due to the increase in tension in membrane. The membrane will try to minimize the surface area to decrease the surface energy, leading to the formation of a very narrow tube. As it becomes thinner, the curvature increases (curvature is inversely proportional to radius). This curvature costs a large bending energy due to the finite bending modulus of the lipid bilayer, thus putting a limit on the tether radius. The result is the formation of a tube-like structure with a finite small radius maintained by a certain force to balance between bending energy and surface energy. Using this assumption, the radius of the tube at equilibrium can be calculated by minimizing the total free energy. Here, the terms *membrane nanotube*, and *tether* are used interchangeably.

4.1.3.1 Previously reported findings

By pulling a membrane tether from synthetic vesicles, relationships between the tether radius and membrane tension were validated by Evans and Yeung (Evans and Yeung, 1994) and used to estimate the bending modulus. As a tether is pulled at a constant velocity, the force on the tether increases linearly during pulling, but the tether radius remains constant for tethers extracted from vesicles and neuronal growth cones (Evans and Yeung, 1994). Sheetz, Dai and Hochmuth have claimed that the apparent membrane tension measured on biological cells combines in-plane membrane tension and the energy of adhesion between the membrane and cortical cytoskeleton (Hochmuth et al., 1996). Jianwu and Sheetz pulled tethers from blebbing cells (Dai and Sheetz,

1999) to understand the membrane tension of solely the cell membrane without a cytoskeleton. During tether extraction, the Sheetz group demonstrated that there exists a range of tether lengths for which the force on the tether remains fairly constant as shown in Fig.4.5. This points towards the existence of membrane reservoirs in cells, maintaining a constant membrane tension (Dai and Sheetz, 1999).

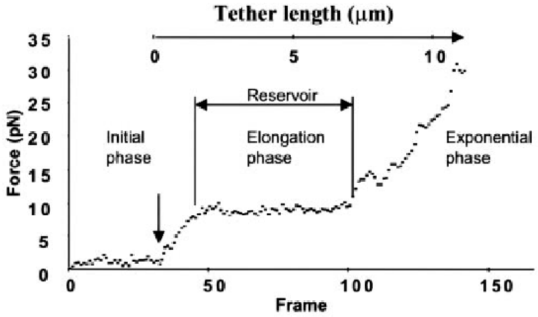

FIGURE 4.5: Plot of force with time during tether formation and elongation. Extracted from Raucher and Sheetz, 1999

4.1.3.2 General theory of tether extraction

In general theory, the free energy of a lipid bilayer with mean curvature C, in the absence of external force has contributions from (i) the Helfrich-Canham curvature energy as lipid bilayers have finite bending modulus B (ii) Surface energy because the number of lipids exposed to water like environment is restricted, giving rise to the membrane tension or surface tension, σ, (iii) The pressure - volume term for the closed shapes systems such as cells, vesicles and lipid membranes, coming from the pressure difference across the outer and inner membrane which can result in the molecules entering or leaving, resulting in swelling or shrinking of cells, vesicles and lipid membranes. Thus, the total free energy of the membrane is described as

$$E = \sigma \Delta A + \int_A \frac{B}{2} C^2 dA - \Delta p V \tag{4.3}$$

The components described above for the free energy of the membrane can also be applied for membrane tethers. For simplicity, we consider a tether pulled from a vesicle as shown in Fig.4.6 to understand the contributors of the free energy of the membrane. The vesicle acts as the reservoir of lipids similarly to the reservoir in cells.

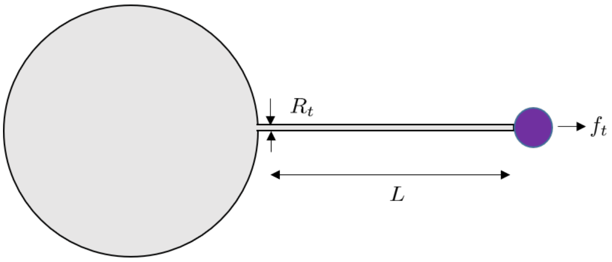

FIGURE 4.6: Schematic of membrane tether of length L and radius R_t pulled by a trapped bead with force f_t from a synthetic vesicle.

For a small tether, the term ΔpV in equation 4.3 is negligible and contributes insignificantly towards determining the tether radius, hence this term can be ignored. Except for the two ends of the tether, the rest of the tube can be treated as a cylinder of radius R_t and length L_t. Thus, for the cylindrical tube, its curvature C is the inverse of the radius R_t and ΔA is $2\pi RL$. Substituting these terms into the equation and adding the work done by pulling 4.3, the total free energy is given by

$$E = \left[\frac{B}{2}\frac{1}{R_t}^2 + \sigma\right] 2\pi R_t L_t - f_t L_t \tag{4.4}$$

Minimizing the free energy with respect to R_t and length L, gives its radius at equilibrium (R_o)

$$R_o = \sqrt{\frac{B}{2\sigma}} \tag{4.5}$$

At equilibrium, the tether radius is a function of just the bending modulus and tension of the membrane and is independent of the pulling force. Substituting the expression for R_o in 4.4

$$E = (\sqrt{2B\sigma}) 2\pi L_t - f_t L_t \tag{4.6}$$

The value of the applied force required to keep a tether of length L_t pulled at equilibrium ($f_t = F_o$) can be found by equating the above free energy to zero

$$F_o = 2\pi\sqrt{2B\sigma} \tag{4.7}$$

which shows that force is independent of tether length. Thus combining equations 4.5 and 4.7, we can write

$$\sigma = \frac{F_o}{4\pi R_o} \tag{4.8}$$

which shows that if radius R_o and force F_o is known, one can calculate tension σ.

In addition, by rearranging equation 4.7, the membrane tension can be expressed in terms of bending modulus B and tether force F_o as

$$\sigma = \frac{F_o^2}{8\pi B} \tag{4.9}$$

4.2 Materials and Methods

4.2.1 Creation and maintenance of the HP1α knock-down cell line

MCF7 (RRID:CVCL0031) cells (ATCC) with constitutive KD of HP1α were created using Qiagen SureSilencing shRNA plasmids. Briefly, MCF7 cells were transfected with linearized scrambled or HP1α KD shRNA (shRNA 1-4) plasmids using X-treme GENE 9 DNA Transfection Reagent (Roche). Transformed cells were selected with 200 μg/mL hygromycin B to obtain a polyclonal population of cells to minimize insertional variation. After determining the level of HP1α KD compared to both MCF7 cells and the scrambled shRNA MCF7 control line, the MCF7 HP1α KD line established with shRNA4 (HP1α KD) was used for this study along with the scrambled shRNA MCF7 control line. The MCF7 HP1α KD and matched control line were maintained in DMEM (Gibco) supplemented with 35 μg/mL hygromycin B (Gibco), 10 μg/mL insulin (Sigma-Aldrich), 1% penicillin/streptomycin (Gibco) and 10% fetal bovine serum (FBS; Gibco) at 37 °C with 5% CO_2 in a humidified atmosphere.

4.2.2 Optical Tweezers for Indentation experiments

4.2.2.1 Experimental setup and measurement technique

Indentation experiments were carried out using the OT setup described in section 2.2. Measurements were conducted at an ambient room temperature of T = 20 °C. A sample chamber consisting of a polylysine coated coverslip and a welled microscope slide was prepared and filled with the loading medium and 2 μm diameter polystyrene beads (Poly Sciences Polystyrene 2.6% Solids latex, 0.001% suspension).

MCF7 cells were allowed to settle onto a polylysine coated coverslip which was subsequently mounted on the piezo stage. Indentation was achieved by moving the piezo stage containing the cell along the Z-axis (longitudinally) towards the fixed trapped bead. A QPD was used to detect the displacement perpendicular to the surface, which is indicated by a change in the size of the interference pattern. As soon as the cell touches the bead, the bead is displaced vertically. The total displacement of the bead combines both longitudinal (perpendicular to the surface) and lateral (parallel to the surface) components of the displacement as shown in Fig. 4.7(b) (Displacement-time graph). At the beginning of the second half of the period, when the cell intercepts the bead and pushes it up, the displacement of the bead in the z direction begins to be significant and it is accompanied by smaller lateral displacements in X and Y directions. Hence, monitoring all components gives the total force exerted on the bead by the cell, and leads to more accurate force measurements. The trap stiffness was calibrated in situ by using the power spectrum of the position signal of the trapped bead and applying the equipartition theorem as described in section 2.2.5. In the first half of the period, the cell moves down and hence the bead diffuses freely in the trap. The laser power was fixed to 1 W at the source. The longitudinal spring constant was found to be (28 ± 0.8) pN/μm (Error represents SE).

4.2.2.2 Young's modulus calculation for optical tweezers (OT)

The apparent Young's modulus (E) was obtained from OT force-indentation measurements by using the Hertz contact model. However, owing to the considerably lower magnitude and range of forces applied in the OT experiment, which limits the exploration of the control variable space, fitting to the full functional form was not carried out in this case as would be typical in an AFM experiment. Instead, an analysis procedure inspired by the work of Yousafzai et al. (Yousafzai et al., 2016) and Bacabac et al. (Bacabac et al., 2008) was used. In this methodology, the indentation depth is written as a constant common indentation depth (D_o) plus a small varying indentation and Eq. 2.23 is expanded as a Taylor series around D_o. Retaining only the first-order term yields:

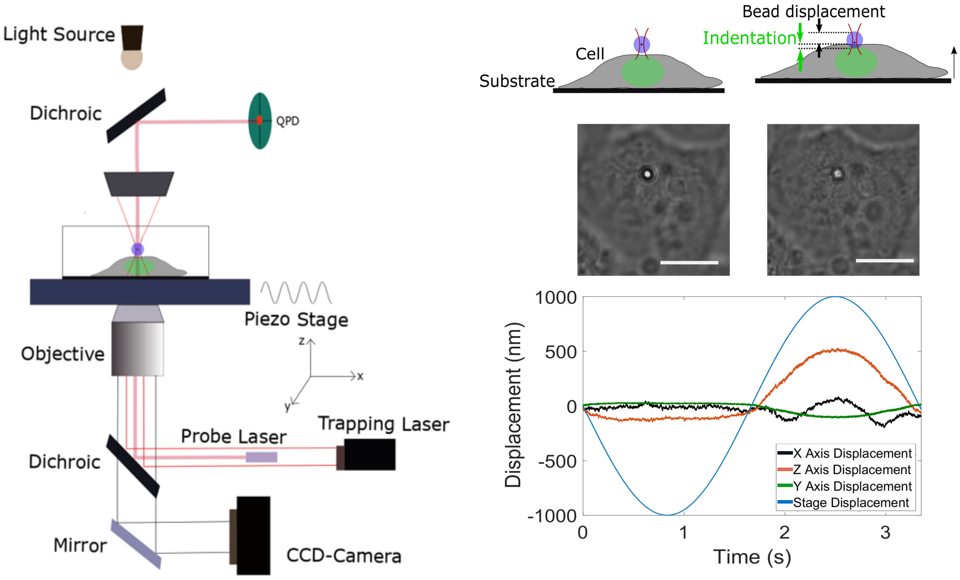

(a) (b)

FIGURE 4.7: OT setup for MCF7 cell indentation and force measurements for longitudinal (top) indentation (a) An infrared laser beam of wavelength 1064 nm is coupled into the optical path of a standard upright microscope via a dichroic mirror and focused into the sample by the objective. The stage position is controlled by a piezo stage. A probe laser of wavelength 675 nm placed in the same beam path and focused at the QPD detects the translations of bead in the trap. A CCD camera is used to acquire image sequences. (b) The cell is moved toward the trapped bead longitudinally (from the top) producing indentation on the cell. The schematic of the experimental procedure shows bead deflection. The sinusoidal movement of the stage displacement (SD) produces bead displacements (BD) in X, Y and Z directions in the second half of the sinusoid. Scale bars - 5μm.

$$E = \frac{3(1-\nu^2)}{4\sqrt{D_o R}} S \tag{4.10}$$

In this work the bead radius was $R = 1\ \mu$m, the Poisson ratio, ν, was 0.4 (Nawaz et al., 2012), and D_o was pragmatically set to 50 nm for each case (corresponding to a difference between the applied stage movement and indenter reponse of ≥ 10 nm as shown in Fig. 4.10), allowing the comparison of the moduli for different samples. $S = \frac{dF}{dD}$, which can be extracted from a simple linear fit to the selected region of the experimental force-indentation curve. It is worth noting that this chosen interval remained within the region of the linear relation between stage displacement and indentation. Analyses were performed using MATLAB (R2016).

4.2.3 Optical Tweezers for membrane tether extraction

4.2.3.1 Experimental setup and measurement technique

The same OT setup as described in section 4.2.2.1 was used to pull membrane tethers from cells. The stage was coupled to a home-built Peltier sample chamber built by Rob Ward (whiterabbitscientific.com) in our research group (Fig. 4.8) to perform experiments at 37 °C.

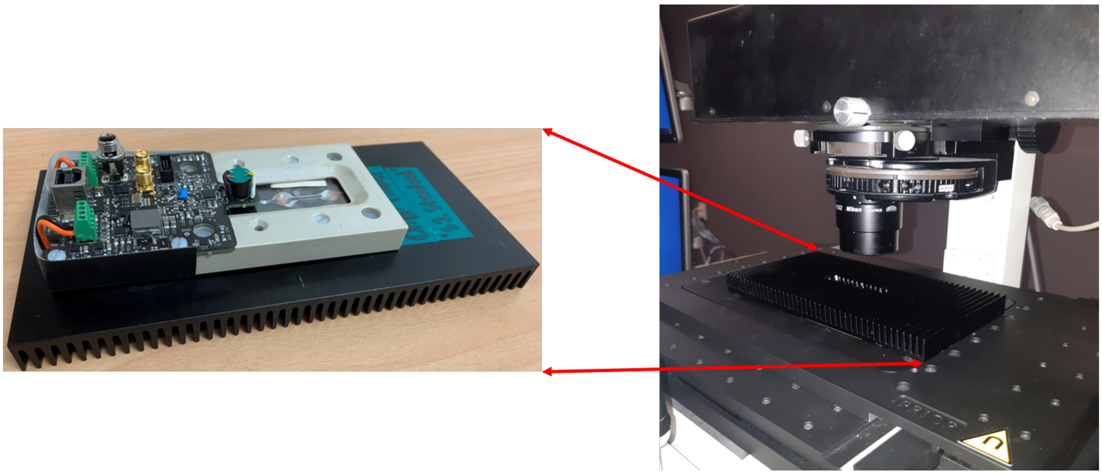

FIGURE 4.8: Home built Peltier sample chamber mounted on the OT setup.

Displacement of a trapped bead from the center of the trap was detected and measured using a QPD. Trap stiffness was calibrated *in situ* just before the experiment using the methods described in section 4.2.2.1. The stiffness constant for 1W laser power at the source was found to be (48 ± 0.9) pN/μm on the X axis and (54 ± 0.7) pN/μm along the Y axis (Error represents SE).

The stage was initially moved so that a surface mounted cell was in contact with optically trapped Concanavalin A (ConA) coated 3 μm bead (Poly Sciences Polystyrene 2.6% Solids latex, 0.001% suspension) for approximately 1 min. The ConA coating helps the specific binding discussed in the next section. The stage was then moved away from the bead, resulting in a tether formation. After pulling a tether of length 2 μm, stepwise displacements of length 2 μm were applied at a speed 100 μm/s as shown in Fig. 4.9.

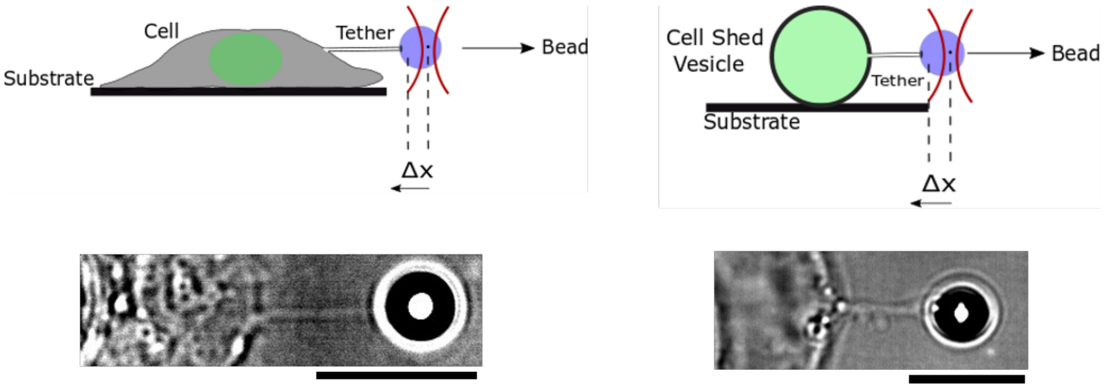

FIGURE 4.9: Schematic and experimental pulling of tether membrane for MCF7 cells and cell shed vesicles. Figure shows a tether being pulled to a length of 4 μm using an optically trapped bead. The bead gets shifted from the center of the trap (Δx) due to the tether force. Scale bars: 5μm.

4.2.3.2 Bead Preparation

To form a membrane tether, a 'handle' is required for OT to hold a part of membrane. The handle is the same polystyrene bead described in section 4.2.2 that binds to the cell surface. The beads were coated with Concanavalin A (Alexa Fluor^{TM} 488 conjugate). ConA is a lectin (carbohydrate-binding protein) which adheres to the cell membrane.

The steps for bead coating were: i) 100 μl beads were taken from the stock solution and sonicated (10-20 secs). ii) 100 μl ConA solutions (0.1 mg/ml in PBS) were prepared and mixed with beads. iii) The beads were incubated overnight at 4°C. iv) The incubated beads were centrifuged at 10,000 g for 10 min, and the supernatant was removed. v) The beads were resuspended in 1.5 ml PBS. vi) The beads were again centrifuged at 10,000 g for 10 min and washed three times. vii) They were finally re-suspended in 100 μl PBS and stored at 4°C. The coated beads were kept for use up to two weeks. This protocol has been taken from Dai and Sheetz. (Dai and Sheetz, 1997).

4.3 Results and Discussion

4.3.1 OT Indentation experiments on MCF-7 cells

OT were used to indent the cell periphery longitudinally (from the top, perpendicular to the surface, as in an AFM experiment) by moving the MCF7 cells against optically trapped micro-beads and measuring the bead displacement. Fig. 4.10 shows the sweeping, sinusoidal movement of the stage during experiments. The trap stiffness, k, was measured *in situ* during the first half of the sinusoidal period, when the nucleus was far away from the optically trapped particle and the bead was freely diffusing in the trap. This is shown in the inset for the interval A in Fig. 4.10. The interaction between a single cell and a bead is observed in the second half of each sinusoid, where the cell is driven into the optically trapped bead. Bead displacements were measured as described in the Materials and Methods. Region B in Fig. 4.10 represents the bead displacements. Once k and BD are known, Hooke's law was used to estimate the restoring force generated ($F = -kBD$). When the cell comes into contact with the bead and begins to push it, BD increases in the same direction as SD. The difference between the displacement of the stage (and thus cell) and the resultant displacement of the trapped bead gives the indentation ($D = SD - BD$). Fig. 4.11(a) shows the indentation interval for control cells. This regime is extracted to obtain F-D curves as shown in Fig.4.11(b). Young's moduli are then obtained by fitting a linear curve which is described in section 4.2.2.2.

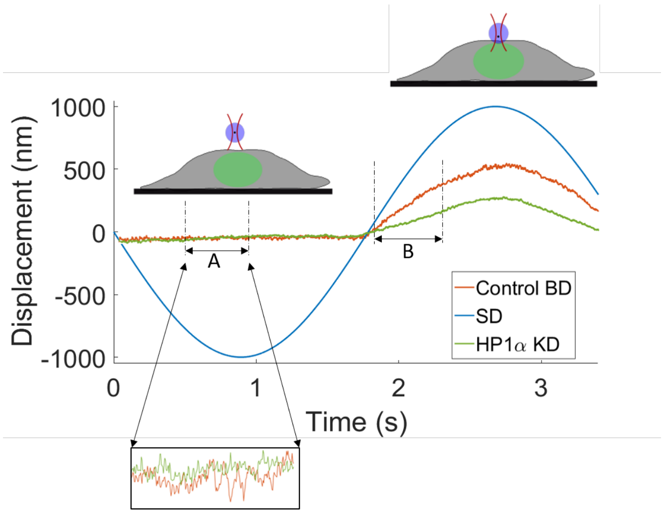

FIGURE 4.10: Stage displacement and bead displacement for MCF7 Control and HP1αKD cells. SD is represented by the *blue* curve. MCF7 control and HP1α KD cells. BD are represented by *red* and *green* curve respectively. Trap stiffness is calculated from interval A, where the bead is freely diffusing in the optical trap. The indentation on the cells is extracted by linearly fitting the region of interval B.

4.3.1.1 HP1α knock-down results in a softer cell periphery as determined by OT

Using the OT method, we can clearly distinguish forces as low as 1 pN, which allows an accurate estimate of the mechanical properties of the cell in the range of 1 to 10 pN. Indentation measurements were performed on 29 control cells (n = 111) and 26 HP1αKD cells (n = 96), where 'n' is the total number of indentations performed. All indentation measurements were carried out in their central region, on top of the cells as shown in Fig. 4.7(b). The F-D plot shown in Fig.4.11(c) indicates that the periphery of the MCF7 control cells has a relatively smaller indentation compared with HP1α KD cells. Indentation values for the maximum applied force for control and HP1αKD cells were (250 ± 78) nm and (320 ± 83) nm, respectively. Using the F-D plots, we obtain Young's modulus value which are shown by the box plot distribution in Fig.4.12. The distribution shows that control cells (E = (117± 38) Pa) are stiffer compared to HP1αKD cells (E = (63 ± 27) Pa). The error represents SE. A t-test has been applied to show the data sets are significantly different ($p < 0.001$). The broad distribution of modulus values signifies that the cell is relatively heterogeneous.

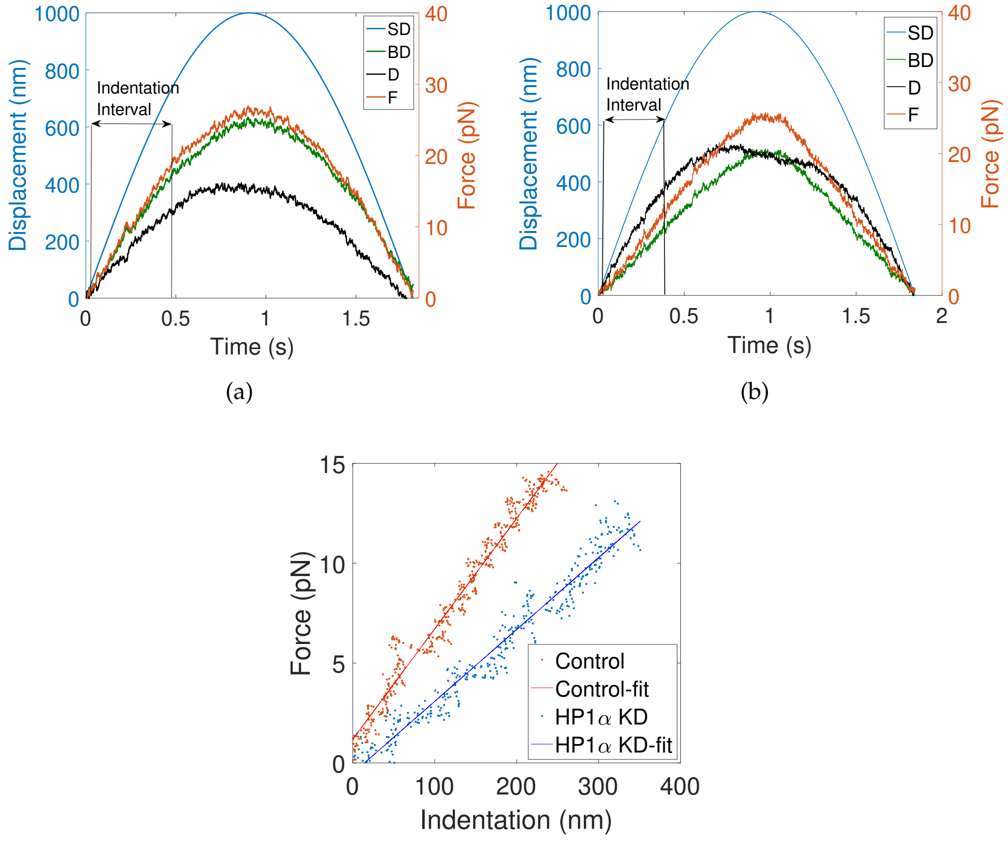

(a)

(b)

(c)

FIGURE 4.11: Longitudinal (from the top) indentation (a), (b) represents the measured bead displacement (green), calculated force (red) and indentation (black) during the indentation interval, when the bead interacts with MCF7 control and HP1αKD cells respectively. (c) Comparison of F-D plot between control and HP1αKD

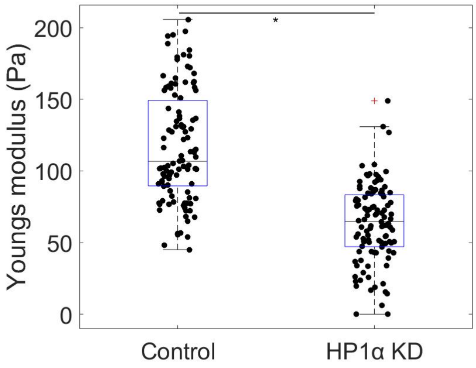

FIGURE 4.12: Comparison of Apparent Young's modulus for control and HP1α KD whole MCF7 cells (*$p < 0.001$). The distribution is represented by box plot with scattered modulus values. The black horizontal line inside the box plot shows the mean value and the red squares shows the outlier data points.

The schematic of a section of the cell as shown in Fig.4.2 indicates that HP1α is present at the nuclear periphery and tethered to the inner nuclear membrane. A recent study has reported that the tethering of heterochromatin to the inner nuclear membrane depends on Lamin B receptor (LBR) and lamin A/C (Solovei et al., 2013). This nuclear envelope is coupled to the cytoskeleton, mostly to actin filaments and microtubules via the so-called LINC (linker of nucleoskeleton and cytoskeleton) complex (Khatau et al., 2012). The knockdown of HP1α protein may be causing a remodelling of the nuclear periphery affecting the nuclear architecture, which could affect the entire coupling to the cytoskeleton and to the cell membrane. The indentation experiments performed by OT suggested higher indentation values with loss of HP1α protein, which is an indication of increased malleability. The thickness of the cell membrane has been reported to be $\approx$ 80 nm and the cytoskeleton beneath the cell membrane just above the nucleus to be $\approx$ 200 nm (Bourne, 1970) . The side view image using confocal microscopy, shown in Fig.4.13 indicates a similar thickness $\approx$300 nm (for the cell membrane and the cytoskeleton). Considering the indentation for maximum force using OT to be around 200 to 450 nm, OT are likely only indenting the cytoskeleton mesh and a small portion of the nuclear envelope as illustrated in schematic in Fig.4.13.

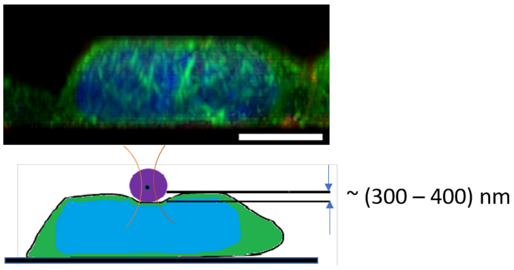

FIGURE 4.13: Side view of MCF7 cell using Immunofluorescence confocal microscopy, stained with DAPI (blue) to detect DNA and an antibody against α-tubulin (Tracy Hale, Massey University). The schematic shows the approximate indentation values using OT. Scale bar: 5μm.

4.3.2 Tether force measurements

Tethers were pulled from MCF7 control cells, HP1αKD cells, and cell shed vesicles using the protocol described in section 4.2.3.1. Tethers were pulled to a constant length of around 5 - 10 μm at steps of 2 μm as described in Fig.4.14. Detachment of the tether as shown in the figure also gives an estimate about the force required to hold the tether at a constant length. Generally the X and Y axes of QPD were set to zero before tether pulling to extract the absolute values of the tether force.

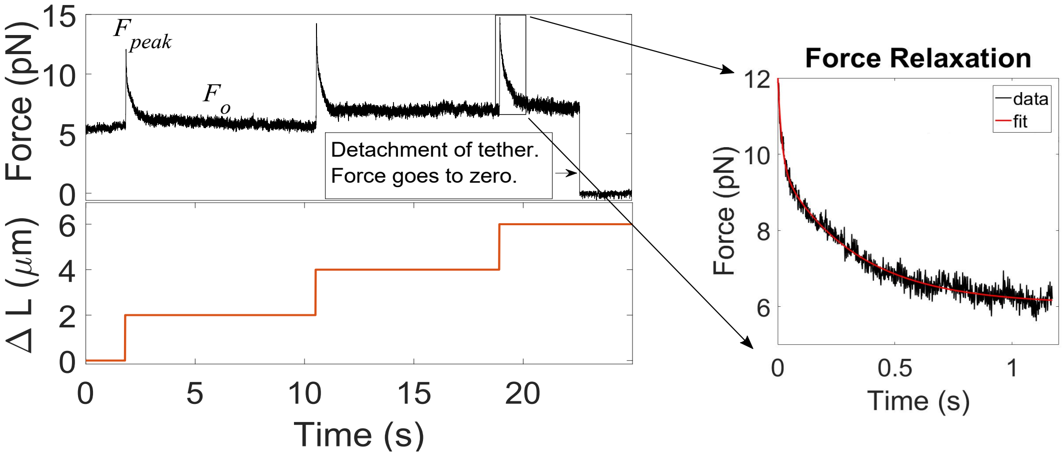

FIGURE 4.14: Evolution of tether force with step-wise tether elongation. The tether was elongated by length ΔL. The inset shows the double exponential fitting to force relaxation. F_{peak} is the peak height and F_o is the static tether force.

Here, four parameters are compared between control and HP1αKD cells and vesicles, namely, i) Peak force F_{peak}, which is the maximum force required during step elongation (ΔL = 2 μm) of the tether, ii) Static tether force F_o, iii) Peak Height F_p (F_{peak}-F_o) and iv) Force relaxation time constants. Here the terms 'cell shed vesicles' and 'blebs' are used interchangeably.

4.3.2.1 Comparison of static tether force (F_o), peak force (F_{peak}) and membrane tension (σ)

During the process of tether formation, the force exerted by the cell membrane on the bead rises transiently and relaxes to a static value, called the equilibrium force value (F_0) (given in equation 4.7). As described in section 4.1.3.2, if the equilibrium force or static tether force F_o and the bending modulus B is known, then we can extract the membrane tension using equation 4.9. The tether reaches a static force value approximately 5 to 7 s after the pulling stops. Fig.4.15 shows the peak height (F_{peak}) and static force (F_o) for MCF7 control, HP1αKD and control cell shed vesicles.

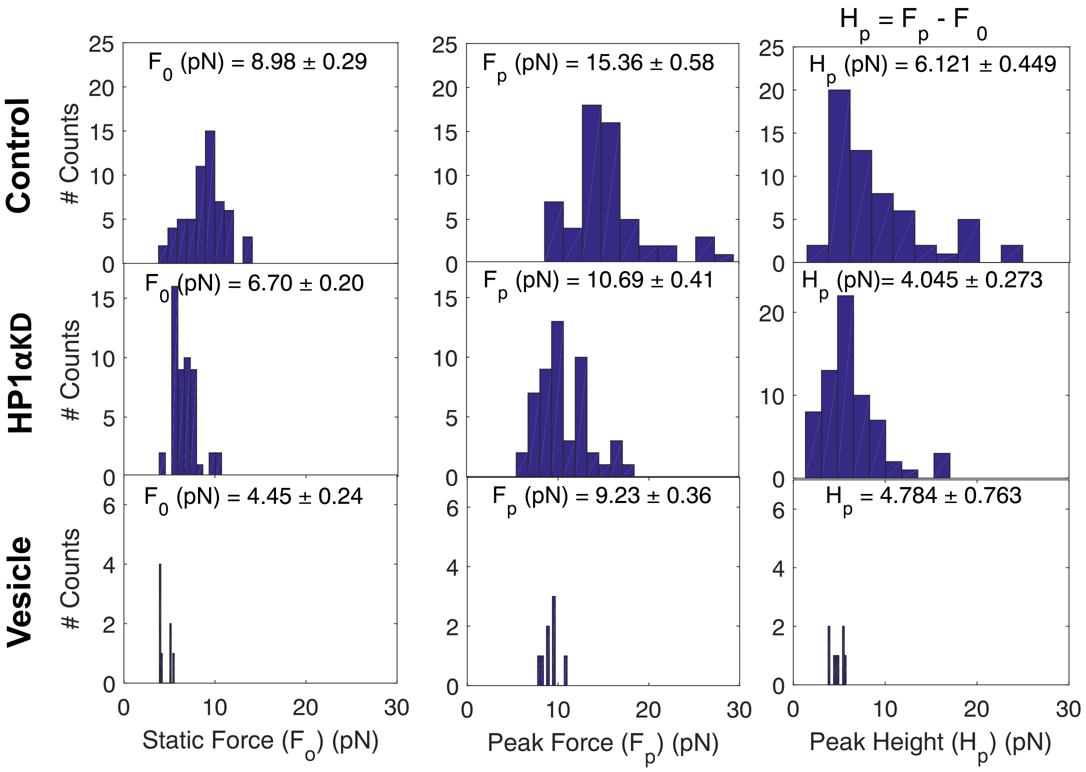

FIGURE 4.15: Static force, Peak Force and Peak Height distributions for Control, HP1αKD and Cell shed control vesicles.

The distribution clearly shows a decrease in F_o, F_{peak} and H_p for HP1αKD cells (18 cells, n = 67) compared to control cells. The obtained values are comparable to the reported literature findings (Datar et al., 2015). Cell shed vesicles showed a further decrease in F_o values (3 vesicles, n = 8). The value of membrane tension can be estimated using a bending stiffness of $2.7 * 10^{-19}$ N.m, a value typical for lipid bilayers, red blood cells and neutrophil membranes (Dai and Sheetz, 1999). Here 'n' indicates the number of pulling events and the error in force measurement represents the standard error in mean. According to Dai and Sheetz (Dai and Sheetz, 1999) the cell static force F_o contains the contributions from membrane tension σ, bending stiffness B of the bilayer, and membrane cytoskeleton adhesion γ.

From the F_o measurements in control and HP1αKD cells, the apparent membrane tension σ were found to be $(3.8 \pm 0.3) * 10^{-6}$ N/m and $(2.1 \pm 0.2) * 10^{-6}$ N/m respectively. This shows that the membrane tension is reduced in HP1αKD cells ($p < 0.001$ (two sample paired t-test)). In a cell shed vesicle γ term is completely lacking. The membrane tension for vesicles $(0.9 \pm 0.3) * 10^{-6}$ shows a significant difference compared to cells, which is in agreement with the values obtained by Sheetz (Dai and Sheetz, 1999). The lacking membrane adhesion term γ (absence of cytoskeleton) in vesicles could be the reason for the reduced membrane tension.

4.3.2.2 Comparison of force relaxation after step elongation of the membrane tether

Elongating the tether by ΔL steps of 2 μm at the rate of 100 μms^{-1} causes a sudden increase in force after each step that slowly relaxes back to the static force value F_o as shown in Fig. 4.14. The observed force relaxation behavior has been reported in different cell types such as red blood cells, E.coli, and neurons (Datar et al., 2015). Campillo et al. (Campillo et al., 2013) reported two well-separated relaxation timescales in multicomponent synthetic vesicle systems and concluded that force relaxation behaviour for tether pulling experiments can be understood by considering a tension gradient along a tubular membrane with membrane reservoirs at its ends. The tension equilibration in such a case occurs mainly through two diffusive modes called peristaltic and Lucassen modes. The faster time scale process is an effect of the intermonolayer friction, whereas the slower time scale comes from an unknown diffusive process over the length of the tether. However, Datar et al.(Datar et al., 2015) concluded that the tethered neck forms a potential barrier for membrane components giving rise to concentration gradient(s) of lipids, which plays a major role in force relaxation. Using this hypothesis, Datar et al. developed a model of the relaxation dynamics which was a good fit to the relaxation data.

Here, for simplicity, a double exponential function is fitted to the force relaxation data obtained in MCF7 cells as shown in the inset in Fig.4.14. A double exponential function shows a good fit to the data obtained compared to the single exponential fit. Double exponential fit in the form $a + b * exp(-x/c) + d * exp(-x/e)$ were fitted to the measured force relaxation curve, where the two time constants $'c'$ and $'e'$ were extracted, $'c'$ represents the fast relaxation and $'e'$ represents the slow relaxation processes. Force relaxation fit for control cells, HP1αKD cells and vesicles is shown in Fig.4.16.

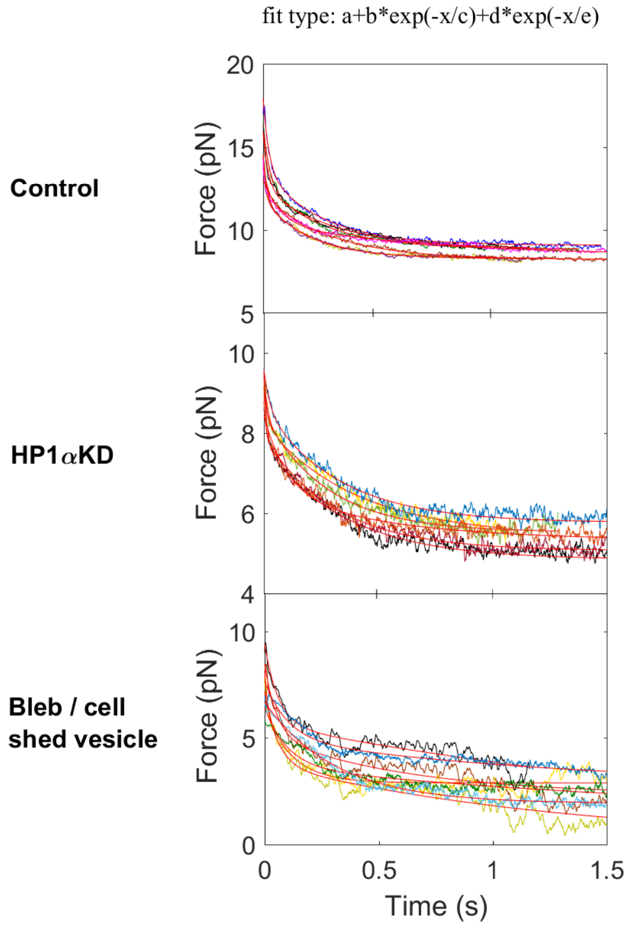

FIGURE 4.16: Force relaxation following tether pulling for Control MCF7 cells (7 relaxation force curves), HP1αKD cell (7 relaxation force curves) and Cell shed control MCF7 vesicle (entire force curves). To test the goodness of fit, χ^2 test has been applied, returning p values < 0.0002 for the entire data sets, suggesting a good fit.

Since the focus of this project was to measure membrane tension values for control and HP1αKD cells, pulling membrane tethers from cell shed vesicles was more of a curiosity experiment. This is the reason for a smaller sample size compared to cells. Histograms comparing the extracted time constants for control, HP1αKD, and cell shed vesicles are shown in Fig. 4.17.

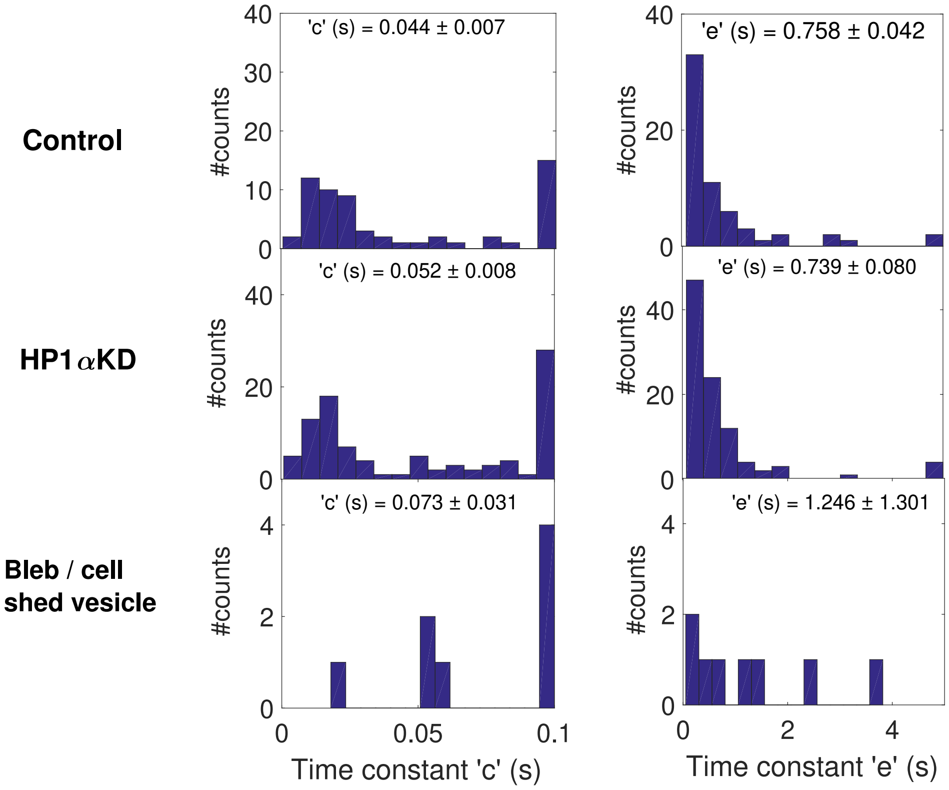

FIGURE 4.17: Tme constant distributions for ′c′ and ′e′ representing Control MCF7 cells, HP1αKD cell and Cell shed control MCF7 vesicles.

Time constant ′*c*′ is almost ten times smaller than time constant ′*e*′ which is in agreement with previous findings of multi-component relaxation events which are governed by a fast followed by slow relaxation processes in similar systems (Campillo et al., 2013). The time constants for control and HPαKD cells show similar time scales as shown in Fig. 4.17. However, for vesicles, there is an increase in time constants compared to cells. There could be many reasons for this increase in time scales, one of the major differences as reported by Datar et al., 2015 is the difference in the lipid reservoir at the base of the tether resulting in different concentration gradients of lipids across the length of the tether and lack of cytoskeleton in vesicles.

4.4 Conclusion

This chapter demonstrates the strength of OT by performing two different experiments: i) Measuring cell-bead interactions leading to the extraction of force - indentation curves and characteristic moduli in a regime that provides complementary information to AFM. OT operate with a loading rate $\approx$ 15 pN/s and maximum forces $\approx$ 20 pN, and they provide complementary information to AFM experiments (AFM cantiliver fluctuations due to thermal fluctuation can be around 30 pN). ii) Pulling membrane tethers from cells/ cell shed vesicles, extracting membrane tension and force relaxation time scales in response to step elongations of the tether.

Loss of HP1α in MCF7 cells resulted in a reduced Young's modulus and membrane tension compared to control cells, which is an indication of increased malleability in these cells. This result suggests that knockdown of HP1α in MCF7 cells decreases the mechanical stability of the cell. Considering that the KD of HP1α largely affects the nucleus, there is a further need to probe just the nuclei in isolation. Hence, chapter 5 focuses on probing nuclei isolated from MCF7 cells using a combination of techniques to deform the nuclei locally (AFM, OT) and globally (MA). By exploring nuclear remodelling pathways regulated by HP1α, there may be certainly a scope to try to understand how to suppress the invasive potential of MCF7 cells.

Chapter 5

Mechanical properties of MCF-7 nuclei

This chapter focuses on probing the mechanical properties of nuclei isolated from HP1αKD and control cells using AFM, OT, and MA. Along with mechanical measurements, quantitative imaging studies of lamin and heterochromatin domains for control and HP1αKD nuclei were carried out in collaboration with Dr. Tracy Hale's lab (Chromatin research group, Massey University).

5.1 Introduction

Among the many organelles inside the cell, the nucleus is one of the most important, as it is a site of various crucial metabolic activities such as DNA replication, RNA processing, gene transcription, and ribosome subunit assem bly. The nucleus is also directly involved in mechanotranduction, as evidence from experimental findings have shown that the adhesion molecule (integrin receptor), cytoskeleton (actin and microtubules) and the nucleus are physically connected (Maniotis, Chen, and Ingber, 1997; Dahl, Ribeiro, and Lammerding, 2008). This physical connection may serve as a pathway to transmit mechanical signals received by the adhesion molecule from the extracellular matrix directly to the nucleus and regulate gene expression. Hence, the nuclei have been found to play an important aspect in whole cell mechanical behaviour. Understanding nuclear mechanics and its link to overall cell mechanics will be a first step in revealing the role of the nucleus in the mechanotransduction of certain diseases related to the malfunction of the nucleus, for example laminopathies which are diseases caused by the mutation of the nuclear lamin A/C gene leading to impaired mechanical integrity of the nucleus (Li and Lim, 2010).

The nuclear envelope separates the nucleus from the cytoplasm as described in section 4.1. As the largest cellular organelle, the nucleus is also a major physical entity, where the nuclear lamina and heterochromatin are key mechanical components (Bustin and Misteli, 2016). An A-type lamin network is relatively stiffer as compared to B-type lamins. (Swift et al., 2013; Lammerding et al., 2006). Depletion of lamin A results in a loss of nuclear rigidity (Furusawa et al., 2015; Stephens et al., 2017a), a reduction of chromatin-lamina attachment, and the loss of heterochromatin (Harr et al., 2015; Solovei et al., 2013). In differentiated cells, it is found that the retention of heterochromatin at the nuclear periphery renders the nucleus less malleable whereas a more diffuse pattern of stem cell-like heterochromatin increases nuclear plasticity (Dahl et al., 2005; Pajerowski et al., 2007). Micromanipulation and atomic force microscope studies have increased the understanding of the contribution heterochromatin makes to the mechanical properties of the nucleus. In particular, these previous studies showed that the mechanical properties of the nucleus were influenced by the compaction state of chromatin, that effected how it dominates local small-strain responses (Stephens et al., 2018; Furusawa et al., 2015; Stephens et al., 2017b; Vaziri and Mofrad, 2007; Dahl et al., 2004). Knockdown of HP1α in MCF7 cells showed a decrease in the Young's modulus of the whole cell as reported in chapter 4. Given the role of HP1α in heterochromatin organisation, this raises the possibility that reduction of HP1α aids malignant cell invasion, not only by disrupting gene silencing but also by altering the mechanical properties of the nucleus. We therefore sought to measure these properties in nuclei extracted from MCF7 cells with HP1α KD against a matched control cell line.

Various techniques (Verstraeten and Lammerding, 2008) have been used to characterize the mechanical properties of nuclei in many different cell types, including AFM indentation (Vaziri, Lee, and Kaazempur Mofrad, 2006; Dahl et al., 2005; Li and Lim, 2010; Coceano et al., 2015) and MA (Deguchi et al., 2005; Guilak, Tedrow, and Burgkart, 2000; Dahl et al., 2005; Pajerowski et al., 2007; Rowat et al., 2005). The elastic modulus measured using these techniques typically ranges from 1-15 kPa. In this study, a combination of AFM, OT and MA-based micropipette techniques were used to characterize the mechanical properties of nuclei isolated from MCF7 control and HP1α KD cells. The OT experiments are indentation experiments carried out in the spirit of AFM but are considerably more sensitive, and can probe the response of the very outer region of the nuclei whose response is usually masked by the thermal fluctuations of the AFM cantilever. In addition, in the OT studies, the longitudinal indentation (into the top of the surface-bound nucleus) was complemented by a lateral indentation (into the side) of MCF7 nuclei, probing the potential anisotropy. Given the small strain exerted in these local indentation experiments, the response is expected to be dominated by the underlying peripheral heterochromatin, with the lamina still slack (Stephens et al., 2018; Furusawa et al., 2015; Hobson et al., 2020; Stephens et al., 2017b; Vaziri and Mofrad, 2007; Dahl et al., 2004).

5.1.1 Previously reported findings using multiple biophysical techniques to probe cells

The mechanical properties of cells and nuclei can be probed using various biophysical techniques as reported earlier. However, most of literature studies focus on and emphasize a particular technique. There are few papers where a combination of techniques have been used to probe nuclei or whole cells. It is interesting to emphasize one technique, but using a combination of techniques can provide greater insight on the length scales, spatial- temporal resolution etc., as each technique probes the sample differently. Although the underlying principles are the same, cell/nuclei mechanics depend on the level of mechanical stress, rate of deformation, the geometry of the mechanical probe, the probe to sample contact area, the probed location in the sample and extracellular context (for eg, adherent cells versus free-floating cells, monolayer of cells versus single cells, etc.) (Wu et al., 2018).

Wu et al (Wu et al., 2018) measured and compared the mechanical properties of MCF7 cells by applying seven different techniques, namely, AFM, magnetic twisting cytometry (MTC), particle-tracking microrheology (PTM), parallel-plate rheometry, cell monolayer rheology (CMR), and optical stretching (OS) in similar environmental conditions. They reported that the elasticity measurement varied by up to 1000 fold between techniques. They also reported that the potential cause of variation was likely due to the differential mechanical responses of cells to the different force profiles produced by these different methods. Coceano et al (Coceano et al., 2015) have also reported similar findings using OT and AFM on MCF7 cells. They report a several orders of magnitude difference between AFM and OT elasticity measurements. Bacabac et al (Bacabac et al., 2008) reported similar elasticity differences between floating bone cells (probed by OT) and adherent bone cells (probed by AFM). Nawaz et al (Nawaz et al., 2012) performed indentation experiments on 3T3 fibroblasts using AFM and OT, highlighting the fact that OT has the benefit of a low force noise ceiling allowing accurate determination of absolute indentation.

5.2 Materials and Methods

5.2.1 Isolation of nuclei for biophysical analyses

Asynchronously grown MCF7 cells (4.2.1) were harvested at confluence, washed twice with PBS then resuspended in ice cold nuclei extraction buffer (320 mM sucrose, 10 mM HEPES, 5mM $MgCl_2$, 1% Triton X-100, pH 7.4) at a concentration of 1 x 10^6 cells/mL, and vortexed gently for 10 s. The cells were incubated on ice for 15 min, vortexed briefly every 5 min, then centrifuged at 2000 x g for 5 min at 4 °C. The nuclear pellet was resuspended in nuclear wash buffer (320 mM sucrose, 10 mM HEPES, 5 mM $MgCl_2$, pH 7.4), and the nuclei were then processed further as required. The HP1αKD (section 4.2.1 describes the creation of the knockdown cell line) were also isolated using the same procedure.

5.2.2 Antibodies

The primary antibodies used for this study were HP1α (2616, Cell Signaling Technology), Histone H3K9me2 (ab1220, Abcam), Histone H3K9me3 (ab8898, Abcam), Lamin A/C (ab108595, Abcam), Phospho Lamin A/C Ser22 (PA5-17113, Invitrogen), Lamin B1 (702972, Invitrogen), Lamin B Receptor (PA5-66473, Invitrogen), and alpha-Tubulin (ab4074, Abcam). Secondary antibodies were anti-mouse Alexa 555 (ab150114, Abcam), anti-rabbit Alexa 647 (ab150079, Abcam), HRP-linked anti-mouse (NA931, GE Healthcare) and HRP-linked anti-rabbit (NA934, GE Healthcare).

5.2.3 Immunofluorescence

Asynchronously grown cells adhered to lysine-coated coverslips were washed twice with Phosphate Buffered Saline (PBS) containing $MgCl_2$ and $CaCl_2$, fixed in 4% paraformaldehyde/PBS for 15 min at room temperature (RT) and then washed with PBS. Cells were permeabilized (0.5%Triton X-100, PBS) for 5 min at RT, washed again with PBS, before incubation in blocking buffer (PBS, 5% bovine serum albumin, 0.5% Tween-20) for 30 min at RT. The appropriate primary antibodies (diluted in blocking buffer) were then added to the cells for 16 h at 4°C. After washing (0.1% Triton X-100, PBS), cells were incubated with the appropriate Alexa fluorophore conjugated secondary antibody, washed again and stained with DAPI, before imaging on either a Leica SP5 DM6000B or Zeiss LSM 900 Scanning Confocal Microscope using an oil-immersion 63x objective lens (NA 1.4). Laser excitation wavelength, and collection ranges appropriate to the fluorophores of each sample were used to detect the emission spectra of the specific combination of DAPI (ex 405 nm, em 410-530 nm), and the secondary antibody Alexa fluorophores; 555 (ex 555 nm, em 565-600 nm) or 647 (ex 647, em 670-720 nm). Z-stacks were collected with a 0.35 μm vertical offset, and projected with maximum intensity. All images were digitally processed for presentation and quantification with ImageJ (Rasband, 2014). Quantification of fluorescence intensity was performed by plotting the profile of grey colour values along a line through a medial optical slice.

5.2.4 Cell fractionation and immunoblot analyses

Using a method adapted from Kapoor et al (Kapoor, Lavoie, and Frappier, 2005), cells at 90% confluence were harvested, washed in PBS, and resuspended in Buffer A (20 mM Tris-HCl pH 7.5, 75 mM KCl, 30 mM $MgCl_2$, 1 mM DTT, 0.5 mM EDTA, 0.5% NP40, complete EDTA-free protease inhibitor) to a concentration of 0.5 x 10^6 cells/100 L, and incubated on ice for 10 min with intermittent mixing. An aliquot was removed and retained as the whole cell lysate fraction. The remaining sample was centrifuged at 7000 x g for 10 min at 4 °C, and the supernatant collected as the cytoplasmic fraction. The remaining pellet was resuspended in Buffer A to provide the nuclear fraction. For immunoblot analysis, samples were resolved by 10% SDS-PAGE then transferred to nitrocellulose. The blots were processed as previously described by Tretiakova et al. (Tretiakova et al., 2014) and visualised using an Azure c600 imaging system (Azure Biosystems).

5.2.5 Scanning electron microscopy (SEM)

Isolated nuclei adhered to lysine-coated coverslips were fixed in Modified Karnovsky's fixative (3% gluteraldehyde (Merck) (v/v), 2% formaldehyde (w/v) in 0.1 M phosphate buffer, pH 7.2) for at least 8 hours. After rinsing three times in 0.1 M phosphate buffer (pH 7.2), the coverslips were dehydrated in a graded series of aqueous ethanol solutions (25%, 50%, 75%, 95%) for 15 minutes each, then in 100 % ethanol for 1 hour. Samples were critical-point dried using liquid CO_2 as the CP fluid and 100 % ethanol as the intermediary (Polaron E3000 series II critical point drying apparatus). Once dried, samples were mounted on an aluminium stub, sputter coated with approximately 100 nm of gold (BAL-TEC SCD 005 sputter coater) and viewed in a FEI Quanta 200 scanning electron microscope at an accelerating voltage of 20 kV.

5.2.6 Transmission electron microscopy (TEM)

Cells were harvested at confluence, and pelleted at 200 x g for 5 minutes. The pellet was resuspended in molten low-melting point agarose and centrifuged at 8000 x g for 1 minute to form a cell pellet suspended in agarose. The cells were fixed in Modified Karnovsky's fixative for at least 8 h, washed three times in 0.1 M phosphate buffer (pH 7.2) for 10 m, followed by post-fixing in 1% Osmium Tetroxide in 0.1 M phosphate buffer for 1 hour. The sample was then washed as above, dehydrated in a series of graded aqueous acetone mixtures (25%, 50%, 75%, 95%, 100%), infiltrated in an equal mixture of resin and acetone overnight, before embedding in 100% epoxy resin (Procure 812, ProSciTech Australia). The resin was replaced another three times for 8 h or overnight before the epoxy resin was cured at 60 °C for 48 h. The embedded samples were cut to 100 nm using a diamond knife (Diatome, Switzerland) on a Leica EM UC7 ultra-microtome (Leica Biosystems, Nussloch, Germany). These cuts were then stretched with chloroform vapour and mounted on grids using a Quick Coat G pen (Daido Sangyo, Japan). The grids were stained with saturated uranyl acetate in 50%

and lead citrate. Samples were then examined with a FEI Technai G2 Spirit BioTWIN Transmission Electron Microscope (Czech Republic).

5.2.7 Biophysical Techniques

AFM, OT and MA were used to probe the mechanical properties of isolated nuclei. Local indentations were performed using AFM and OT, while a global deformation was applied out using MA. Setup description and operation of the AFM technique are described in section 2.3 of chapter 2 . AFM indentation on nuclei using a cantilever with a bead attached at the tip is shown in Fig.5.1(a). OT setup and calibration procedure are described in section 2.2 and 2.2.5 of chapter 2 respectively, while the indentation procedure is described in 4.2.2 of chapter 4. Using the OT setup to probe the nuclei laterally (from the side) and longitudinally (from the top) is shown in Fig.5.1(b). Fig.5.1(c) shows the MA technique being used to aspirate and deform nuclei. The material properties of these nuclei were compared using the two sample t - test and Wilcoxon Signed - Rank test (for unequal variances). The p values used to determine statistical significance of differences are reported in the figure captions or elsewhere in this chapter. The two sample t - test and Wilcoxon Signed - Rank test produced the same results. All the techniques were carried out at 21 °C.

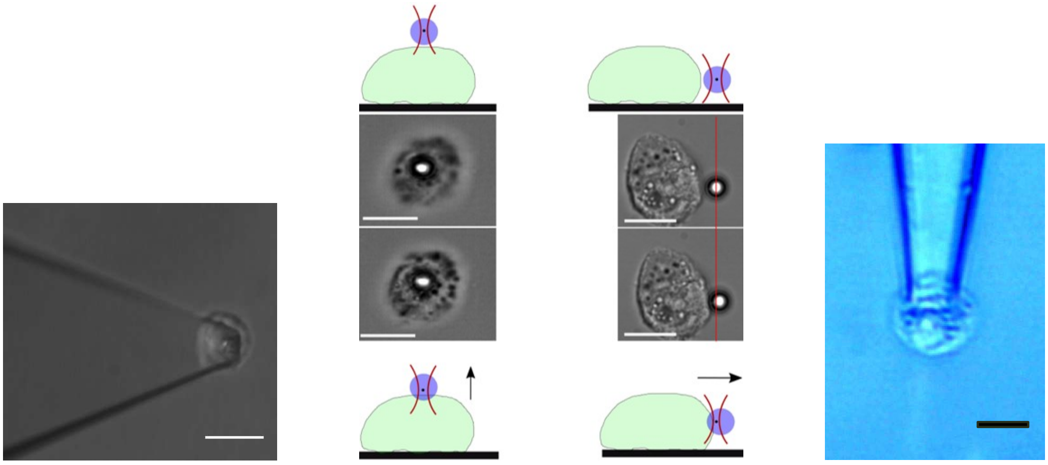

(a) (b) (c)

FIGURE 5.1: Techniques used to probe nuclei. (a) AFM indentation : Cantilever with a bead attached at the tip for probing the nuclei. Scale bar - 10μm. (b) OT setup : A nucleus is either moved towards the trapped bead longitudinally (from the top) or laterally (from the side) producing an indentation on the nuclei. The schematic of the experimental procedure shows the bead deflection. Scale bars - 5 μm. (c) Microaspiration experiments : A nucleus is aspirated into the conical pipette deforming the nucleus. Scale bar - 5 μm.

5.3 Results and discussions on biological assays of MCF7 nuclei obtained in collaboration with Tracy Hale's Lab

5.3.1 HP1α knock-down alters heterochromatin organisation

To explore if the reduction of HP1α alters the biophysical and biological properties of nuclei, MCF7 cells with constitutive KD of HP1α and a matched MCF7 control line were established. The reduction in HP1α expression in the MCF7 cells was confirmed by immunoblotting and immunofluorescence microscopy using an antibody directed against HP1α. Fig. 5.2(a) shows a reduction in the level of protein expression compared to the control cells, which have distinct HP1α foci present in their nuclei that are absent in the nuclei of the HP1α KD cells (Fig. 5.2(b)). Interestingly, when these cells were grown in 2-D culture, the shape of their nuclei differs. The nuclei, represented by DAPI stained genomic DNA, are rounder in the MCF7 control cells and flatter in the HP1α KD cells, although there was no difference in the volumes of these nuclei as shown in Fig.5.3(a).

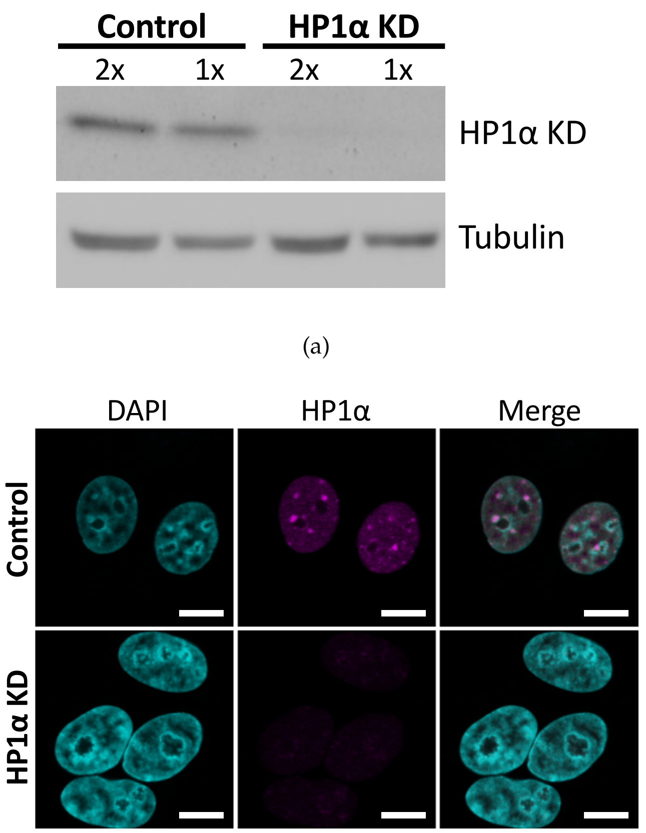

(a)

(b)

Figure 5.2: Level of HP1α protein in MCF7 cells with constitutive HP1α KD. (a) Immunoblot showing HP1α expression in MCF7 cells that constitutively express either an HP1α shRNA or the matched scrambled shRNA control. Increasing amounts of total cell lysates, (1x) 25 μg and (2x) 50 μg, are loaded. The immunoblot was stained with antibodies against HP1α and α-tubulin as a loading control. (b) Immunofluorescence confocal microscopy images of MCF7 control (top panel) and MCF7 HP1α KD (bottom panel) cells stained with DAPI to detect DNA (*cyan*) and an antibody directed against HP1α (*magenta*). Scale bars - 20 μm.

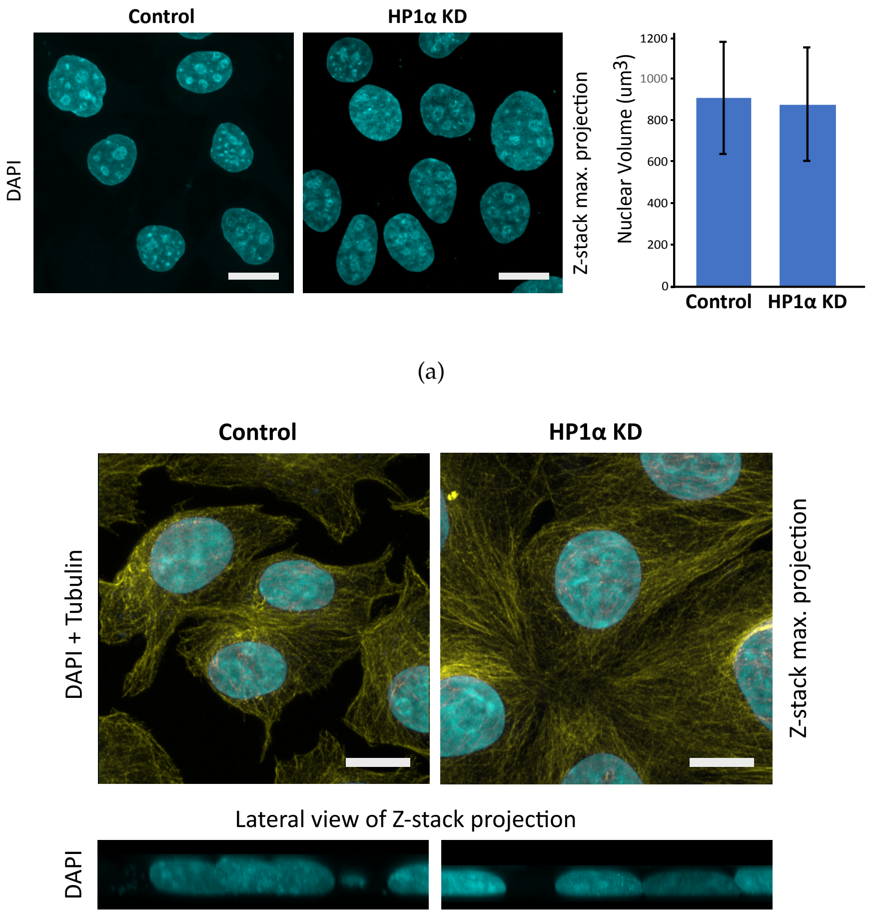

(a)

(b)

FIGURE 5.3: (a) Confocal microscopy images of z-stack maximum intensity projections from MCF7 control and MCF7 HP1α KD cells stained with DAPI to detect DNA (*cyan*), with a graph showing the average volume of the nuclei (standard error). Scale bars - 20 μm. (b) Representative confocal microscopy images of z-stack maximum intensity projections from MCF7 control and MCF7 HP1α KD cells growing asynchronously in 2-D culture stained with DAPI to detect DNA (*cyan*) and an antibody directed against α-Tubulin to show the cytoskeleton (*yellow*). Scale bars - 20 μm. The bottom panel is a 90° rotation of the above z-stack maximum intensity projection showing the DNA (*cyan*).

Heterochromatin domains are marked by H3K9me2 and H3K9me3 with those associated with the lamina being enriched in H3K9me2 (Kind et al., 2013; Janssen, Colmenares, and Karpen, 2018) to determine if the reduction of HP1α disrupts heterochromatin organisation. The level and localisation of these heterochromatin marked domains was analysed by confocal immunofluorescence microscopy. H3K9-me2 and H3K9me3 are an epigenetic modification to the DNA packaging protein Histone H2 and Histone H3 respectively. It is a mark that indicates the di and tri - methylation at the 9th lysine residue of the histone H2 (H3K9me2) and H3 (H3K9me3) proteins respectively. Medial optical slices through the nuclei showed that there is a distinct punctate layer of H3K9me2 marked heterochromatin adjacent to the Lamin A/C network in the control cells. However, a more dispersed layer of H3K9me2 lines the Lamin A/C network in nuclei lacking HP1α, with a reduction in the level of H3K9me2 marked heterochromatin within the nuclear interior that surrounds the nucleoli (Fig 5.4(a)). This agrees with the observed global reduction in the level of H3K9me2 in MCF7 cells with HP1α KD (Fig 5.4(b)). There is also a reduction in the global level of H3K9me3 in the MCF7 HP1α KD cells (Fig 5.4(b)), in a decrease in the enrichment of H3K9me3 in heterochromatin compared to those domains distributed within the MCF7 control cells (Fig 5.4(a)). These differences are also reflected in electron micrographs that show MCF7 control cells have characteristic electron dense regions of heterochromatin and lighter regions of euchromatin, while the pattern of chromatin is more homogeneous in the HP1α KD cells (Fig 5.4(c)).

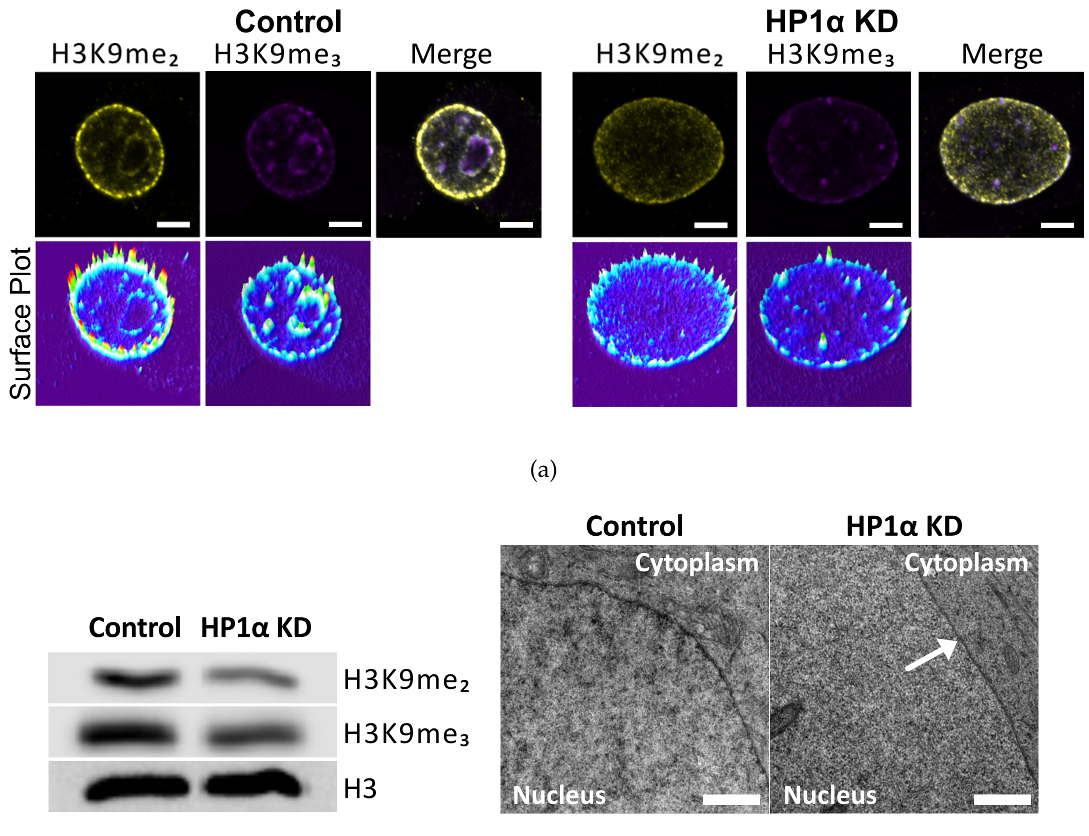

(a)

(b)

(c)

FIGURE 5.4: Knockdown of HP1α disrupts heterochromatin organization in MCF7 cells. (a) Representative immunofluorescence confocal microscopy images of MCF7 control (left panel) and MCF7 HP1α KD cells (right panel) stained with antibodies against markers of heterochromatin, dimethylation of lysine 9 on histone H3 (H3K9me2) (*yellow*) and trimethylation of lysine 9 on histone H3 (H3K9me3) (*magenta*). Fluorescense surface plots of the medial slices through the nuclei (above) demonstrate the intensity of antibody staining. Scale bars - 5 μm. Additional images of cells are presented in Fig. C.1. (b) Immunoblot analysis of extracted histones from MCF7 control and HP1α KD cells probed with antibodies against H3K9me2 and H3K9me3. An antibody against histone H3 is used as a loading control. (c) Representative electron micrographs showing regions of compact heterochromatin at the nuclear periphery in MCF7 control cells (*white* arrows), while the nuclei of MCF7 HP1αKD cells have a more diffuse chromatin patterning. Scale bars - 500 nm.

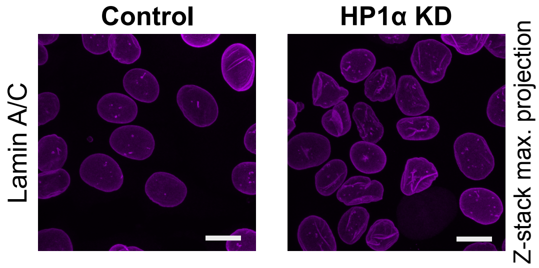

(a)

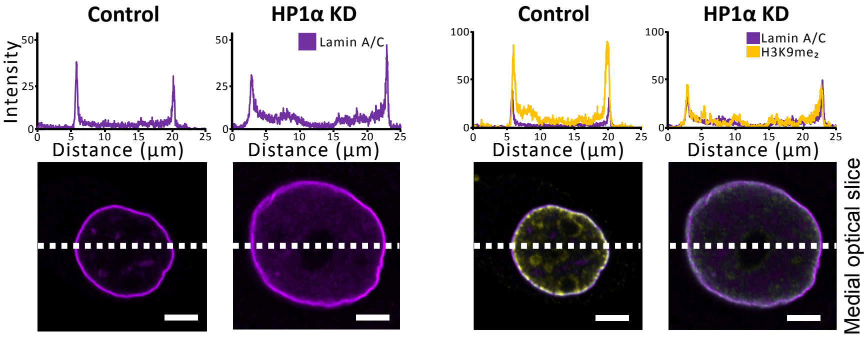

(b)

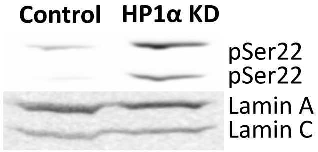

(c)

FIGURE 5.5: Knock-down of HP1α alters the lamin A/C network. (a) Representative confocal microscopy images of z-stack maximum intensity projections of MCF7 control and MCF7 HP1α KD cells probed with an antibody against Lamin A/C. Scale bars - 20μm. (b) Representative confocal microscopy medial sections of individual nuclei from MCF7 control and MCF7 HP1α KD cells stained with antibodies against Lamin A/C and H3K9me2. Top panel, medial slice showing Lamin A/C (*magenta*) alone. Bottom panel, showing Lamin A/C (*magenta*) overlaid with H3K9me2 (*yellow*). Above each medial slice, are line plot profiles of fluorescent intensity (percentage of grey value saturation). Scale bars - 5 μm. Additional images of cells are presented in Fig. C.2 and Fig. C.3. (c) Whole cell lysates from an equal number of MCF7 control or HP1α KD cells were analysed by immunoblotting with an antibody against Lamin A/C phosphorylated on serine 22 (top panel) and Lamin A/C (bottom panel).

Given the decrease in compaction of the H3K9me2 enriched lamina-associated domains upon HP1α KD, to identify if this disruption to the integrity of the peripheral heterochromatin interferes with the nuclear lamina, the individual lamin networks were visualised by immunofluorescence confocal microscopy. Fig 5.5(a) shows that the morphology of the Lamin A/C network is generally more crumpled in HP1α KD cells compared to those of the MCF7 control cells. Medial optical slices through the nucleus show a distinct Lamin A/C layer in the control cells that is associated with peaks of H3K9me2 as demonstrated by the line plots (Fig 5.5(b)). In comparison the peaks of H3K9me2 associated with Lamin A/C in the HP1α KD cells are less prominent (Fig 5.5(b)).

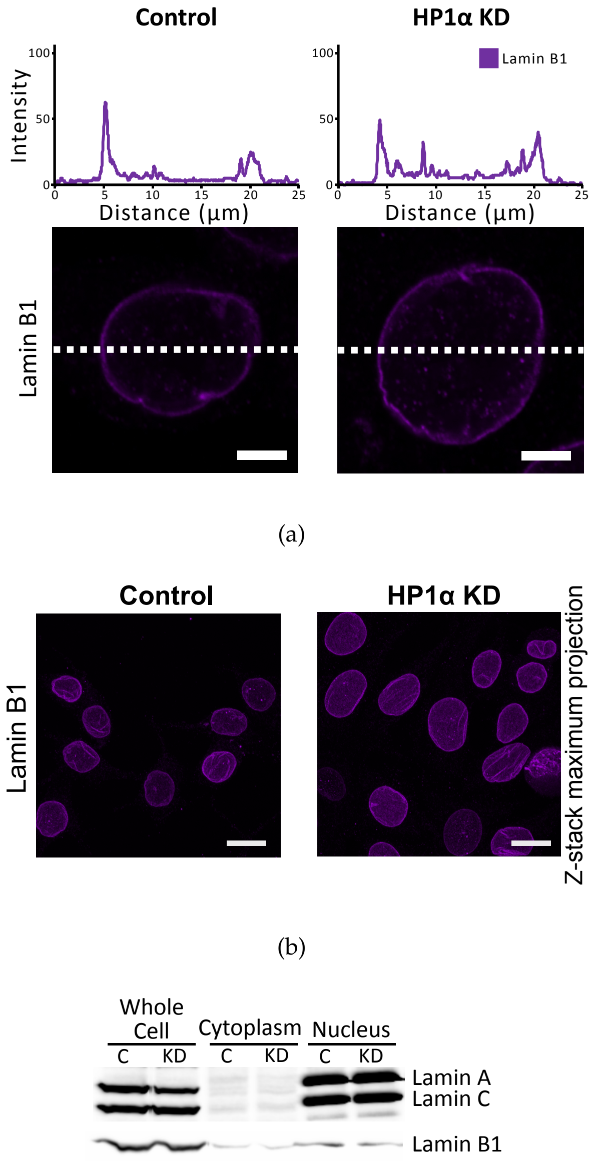

(a)

(b)

(c)

FIGURE 5.6: The Lamin B1 network is not disrupted by knock-down of HP1α. (a) Representative medial slice from confocal microscopy images of MCF7 control and MCF7 HP1α KD cells probed with an antibody against Lamin B1. Above each medial slice are line plot profiles of fluorescent intensity (percentage of grey value saturation). Scale bars - 5 μm. Additional images of cells are presented in Fig. C.4. (b) Representative confocal microscopy images of z-stack maximum intensity projection from MCF7 control and MCF7 HP1α KD cells probed with an antibody against Lamin B1. Scale bars - 20 μm. (c) Whole and fractionated cell lysates from an equal number of MCF7 control or HP1α KD cells were analysed by immunoblotting with an antibody against Lamin A/C (top panel) and Lamin B1 (bottom panel).

There is also more Lamin A/C located within the interior of the nuclei (Fig 5.5(b)), indicating an increase in the soluble pool of lamin A/C in the nucleus of MCF7 cells with HP1α KD. This is supported by the demonstration that the level of Lamin A/C phosphorylated on serine 22, which is associated with nucleoplasm localised Lamin A/C during interphase (Kochin et al., 2014), is higher in cell lysates prepared from HP1α KD cells than control cells (Fig 5.5(c)).

In contrast to the Lamin A/C layer, the distribution of Lamin B1 appears to be comparable between the MCF7 cells and HP1α KD (Fig 5.6(a)) with minimal disruption to the morphology of the Lamin B1 layer (Fig 5.6(b)). To determine if lamin expression is altered in cells with reduced HP1α, cell fractions were prepared from MCF7 control and HP1α KD cells. Fig 5.6(c), shows there is no change in the expression of Lamin A/C or B1 with HP1α KD, nor does the amount differ of each lamin present in the nuclear fraction.

In summary, reduction of HP1α alters heterochromatin organisation. The dispersed domains of lamin associated heterochromatin marked by H3K9me2, likely reflect a decrease in the tethering of heterochromatin to the nuclear envelope due to loss of the interaction of HP1α with Lamin B receptor and PRR14 proteins. (Polioudaki et al., 2001; Kourmouli et al., 2001; Poleshko et al., 2013; Solovei et al., 2013).

5.4 Results and Discussion related to biophysical techniques

5.4.1 AFM Indentation experiments on MCF-7 nuclei

To determine if these changes in the HP1α KD cells alter the malleability of the nuclear periphery, nuclei were isolated from the MCF7 cell lines for mechanical measurements. The integrity of the isolated nuclei was confirmed using SEM and as shown in Fig. 5.7, the extraction procedure resulted in nuclei with little associated debris.

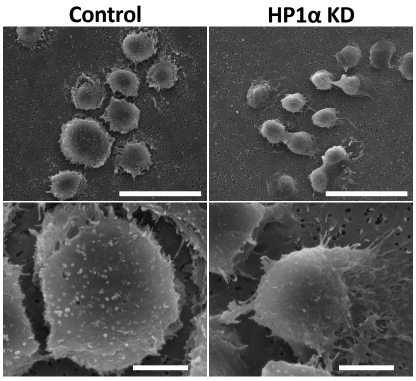

FIGURE 5.7: Representative scanning electron micrographs of nuclei isolated from MCF7 control and MCF7 HP1α KD cells. Scale bars : top panel - 30μm, bottom panel - 5μm.

Nuclei were indented with a spherical tip cantilever at a constant rate of 0.5 μm/s and three sweeps were performed between zero and maximum forces of 300 pN, 500 pN and 1nN. A spherical bead indenter was used instead of sharp tip to average over a larger surface area with a well defined contact geometry (Smith et al., 2005). The $F-D$ curves were deduced and the Hertz's equation was fitted to the curve to extract the apparent elastic modulus or Young's Modulus (E). This was done for all the three maximum forces applied as shown in Fig. 5.8.

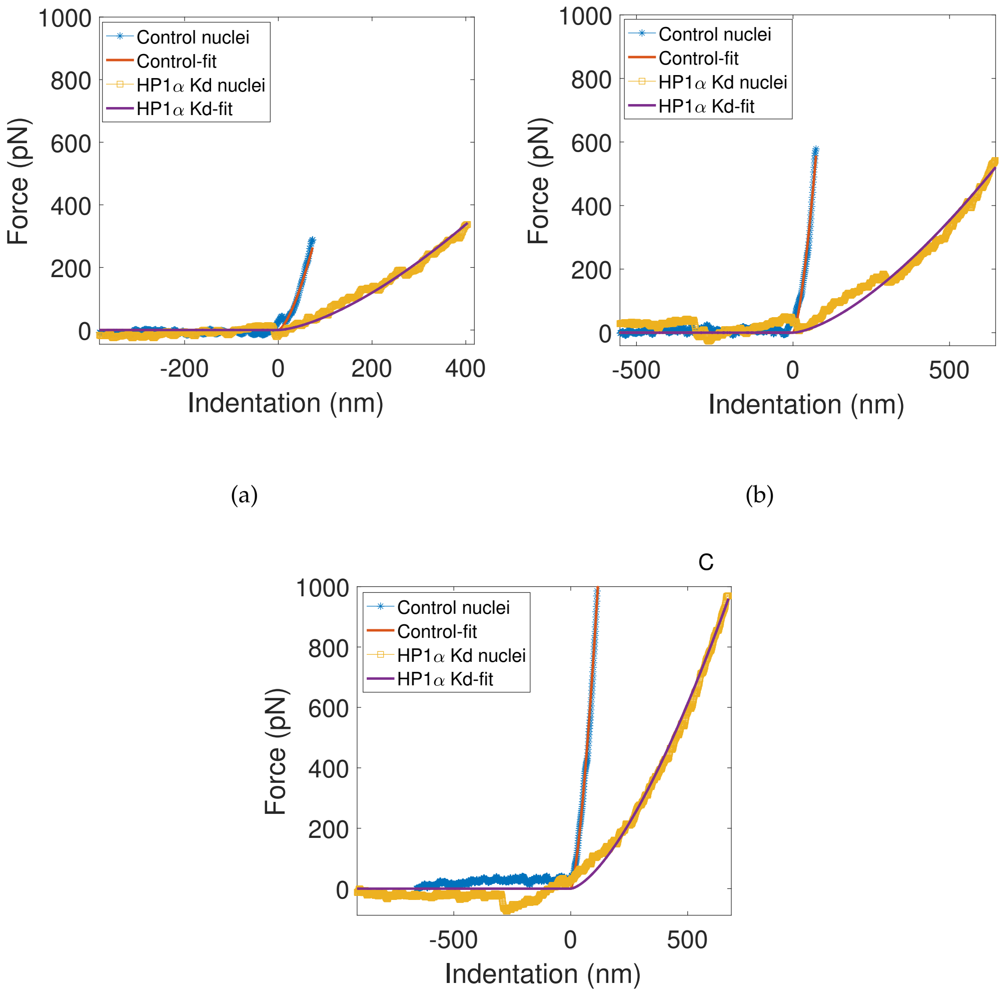

(a) (b)

(c)

FIGURE 5.8: Hertzian curve fitting on three different sweeps from zero to maximum force of (a) 300 pN, (b) 500 pN and (c) 1 nN for Control and HP1αKD nuclei.

The indentation and the retraction curves were similar, suggesting that the response was highly reversible and hence can be considered to be consistent with largely elastic behaviour.

5.4.2 HP1α knock-down results in softer nuclei as determined by AFM force measurements

A clear difference can be observed in the $F - D$ curve recorded for the control and for the HP1α KD nuclei as shown in the combined $F - D$ curves in Fig. 5.9. The magnitude of the D for HP1α KD nuclei is about an order of magnitude higher than for control nuclei signifying that the HP1α KD nuclei are comparatively softer in response to this type of local deformation.

Indentations performed by higher nN-scale forces are likely to induce damage and may have an effect on the measured modulus and were not pursued. Measuring forces below $\sim$ 30 pN was not possible in these AFM experiments due to the thermal fluctuations of the AFM cantilever in the liquid, setting a limit below which applied forces could not be measured and the absolute indentation becomes impossible to assess. To have an absolute estimate of indentation at forces below 30 pN, OT were additionally implemented.

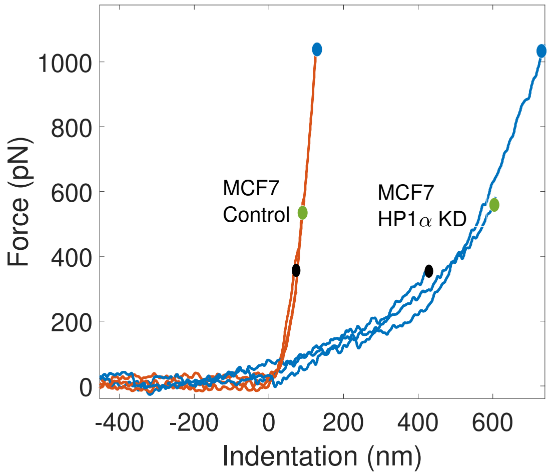

FIGURE 5.9: Combined AFM indentation plots showing three sweeps that were applied between zero and maximum forces of 300 pN (*black* circle), 500 pN (*green* circle) and 1000 pN (*blue* circle) on MCF7 control and HP1α KD nuclei.

A force map has also been obtained on control and HP1αKD nuclei, where the slope image (Fig. 5.10) in the force map gives a qualitative insight about the effective stiffness. It can be seen that the HP1αKD nucleus appears to be less heterogeneous as compared to control (more distributed patches). Secondly, the HP1αKD nuclei edges appears to be softer (darker shade) than the control nuclei.

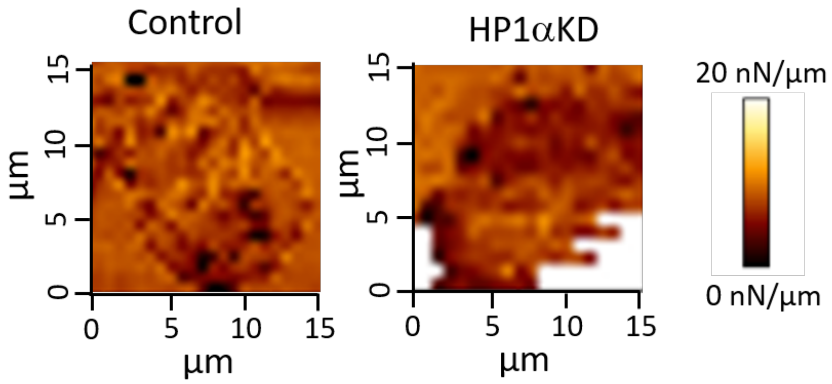

FIGURE 5.10: Force map showing slope (effective stiffness) of Control and HP1αKD nuclei

5.4.3 OT Indentation experiments on MCF-7 nuclei

To measure deformations at low forces, OT were used to perform indentation by laterally (from the side, parallel to the surface) and longitudinally (from the top, perpendicular to the surface, as in an AFM experiment) moving the MCF7 nuclei against optically trapped micro-beads and measuring the bead displacement (BD) as shown in Fig. 5.11. When the trapped bead is pushed into the nuclei, the apparent Young's modulus can be estimated using the Hertzian contact model as described in Materials and Methods. The same size bead (2 μm diameter) and the same deformation rate (0.5 μm/s) as applied in the AFM measurements were used, in order for the experiments to be as comparable as possible. It should be noted however that owing to the extreme sensitivity of the OT, experimental data will be obtained in a regime where the AFM experiment will be unable to determine if contact has yet been made, and owing to this a large offset is expected in the putative zero displacement point in the two experiments.

Fig. 5.11 shows the sweeping, sinusoidal movement of the stage during experiments where the region B is extracted to deduce Young's modulus. This procedure was described meticulously in sections 4.2.2.1 and 4.3.1 of chapter 4, where indentation was performed on whole cells. To investigate potential anisotropy in the mechanical properties of the nuclear periphery, nuclei were indented both laterally and

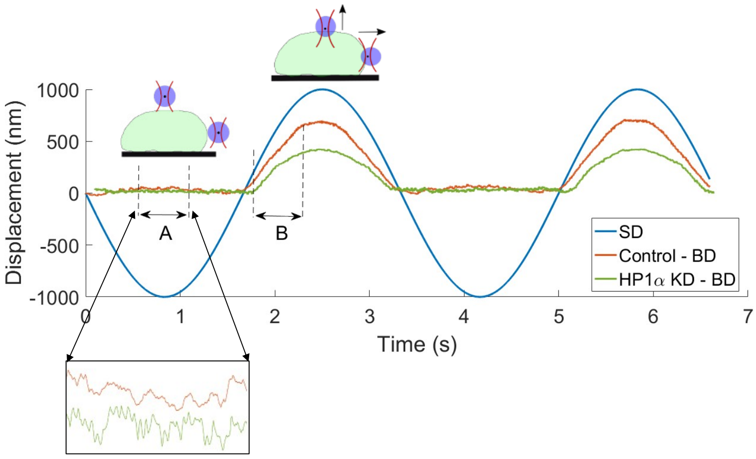

FIGURE 5.11: *SD* and *BD*. *SD* is represented by the *blue* curve. MCF7 control and HP1α KD nuclei *BD* are represented by *red* and *green* curve respectively. Trap stiffness is calculated from interval A, where the bead is freely diffusing in the optical trap. The *D* on the nuclei is extracted by linearly fitting the region of interval B.

longitudinally in relation to the surface. Nuclei having a semi-spherical shape (as opposed to substantially spread on the surface to which they are attached) are able to be indented laterally as shown in Fig. 5.1(b). This lateral indentation avoids potential laser-induced local heating that is present for longitudinal indentation, when the laser passes through the nuclei (Peterman, Gittes, and Schmidt, 2003).

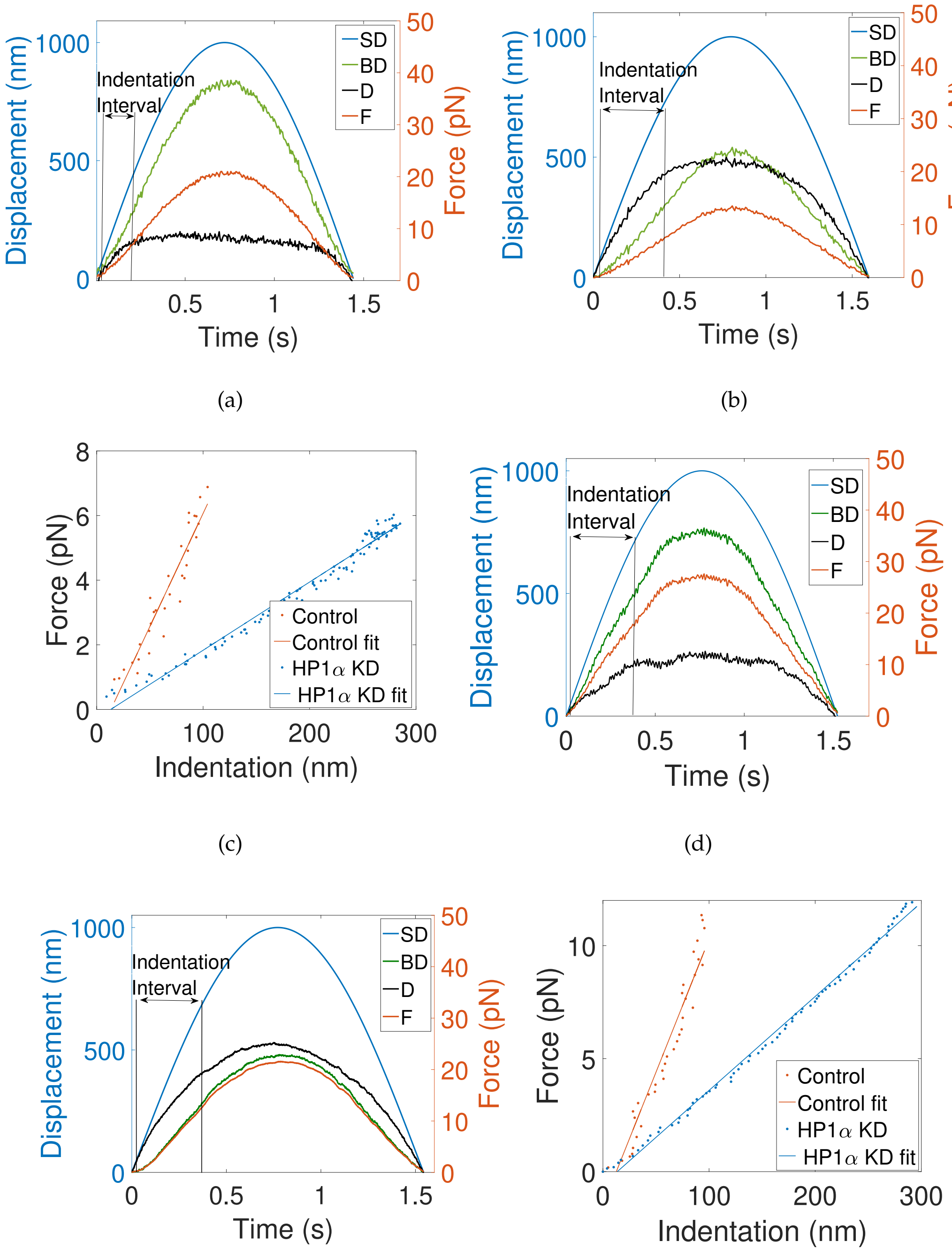

(a) (b) (c) (d) (e) (f)

FIGURE 5.12: **Longitudinal** (from the top) indentation: (a) and (b) represents the measured *BD* (*green*), calculated *F* (*red*) and *D* (*black*) during the indentation interval, when the bead interacts with MCF7 control and HP1αKD nuclei respectively. (c) $F - D$ curves extracted from the indentation interval. **Lateral** (from the side) indentation: (d) and (e) represents the measured *BD* (*green*), calculated *F* (*red*) and *D* (*black*) during the indentation interval, when the bead interacts with MCF7 control and HP1αKD nuclei respectively. (f) $F - D$ curves extracted from the indentation interval.

5.4.4 HP1α knock-down results in softer nuclei as determined by OT

From the temporal sequences for the indentation intervals shown in Figs. 5.12(a), 5.12(b), 5.12(d) and 5.12(e), $F - D$ curves similar to AFM were obtained (compare Figs. 5.12(c) and 5.12(f) with Fig 5.9). Consistent with the AFM experiments, the MCF7 nuclei with HP1α KD have greater indentation compared to the control nuclei for the same applied force. The slope of the $F - D$ plot is used to estimate Young's modulus using equation 4.10. Using the OT method, we can clearly distinguish forces as low as 1 pN, which allows a more accurate estimate of mechanical properties in the range from 1 to 10 pN in comparison with AFM experiments. Table 5.1 gives the maximum indentation for both types of nucleus using lateral and longitudinal indentation methods (uncertainty indicates standard deviation). The average indentation for the two indentation methods is similar, giving confidence in both methods and showing that there is probably little effect of any anisotropy in this setting. The periphery of the MCF7 control nuclei have smaller indentations compared to HP1α KD nuclei, suggesting that reduced expression of HP1α makes the nuclei softer to local low-strain indentations.

TABLE 5.1: Comparison of indentation methods from maximum force applied by OT

Method of Indentation	Control nuclei	HP1α KD
Longitudinal (nm)	105 ± 31	359 ± 137
Lateral (nm)	123 ± 61	351 ± 79

5.4.5 Comparison of force-indentation plot and elastic modulus using OT and AFM

AFM provides insight into the mechanical properties of the nuclei at larger forces (∼1 nN) than used for OT. However, OT gives better measurements of the absolute indentation for lower forces (∼10 pN) at which AFM measurements are limited by the thermal noise of the cantilever in liquid. In Fig. 5.13, it can be seen that the cantilever noise is around (50 ± 30) pN (uncertainty indicates standard deviation), which is roughly the maximum force exerted in our OT setup. The AFM data has been arbitrary shifted in x-direction to qualitatively show that OT detects contact with nuclei earlier than AFM, which is illustrated in the schematic figure shown later in Fig.

5.17(b).

The distributions of results from the repeated elastic modulus measurements for the MCF7 control and HP1α KD nuclei obtained using AFM and OT are shown in Fig. 5.14 in box plot distributions. For OT, experiments were carried out on 22 nuclei (lateral indentation) and 12 nuclei (longitudinal indentation). For AFM, experiments were conducted on 17 nuclei from both MCF7 control and HP1α KD cells. A difference in the elastic modulus of the nuclear periphery between control and HP1α KD can be observed using either AFM or OT ($p < 0.0001$). Fig.5.14(b) shows the Young's modulus obtained for a maximum force of 0.5 nN. Similar AFM experiments were carried out for a maximum force of 0.3 nN and 1 nN (Appendix Fig. C.5). These results are consistent with previous studies on the differences of nuclei mechanics extracted from benign (MCF-10A) and malignant (MCF-7) cells Li and Lim, 2010 .

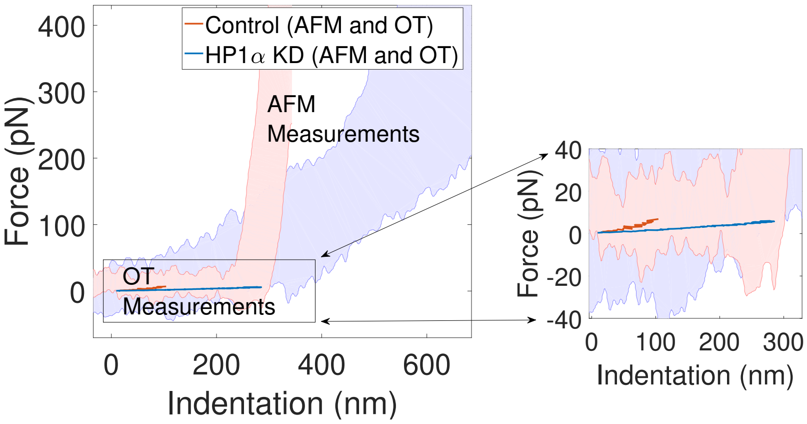

FIGURE 5.13: Comparison of the noise in the force indentation plots for control and HP1α KD nuclei using AFM and OT. The AFM data has been arbitrary shifted to show that OT detects contact earlier than AFM.

The apparent Young's moduli measured for the control nuclei have a larger spread of values, signifying that the structure of the MCF7 control nuclei are more mechanically heterogeneous in nature compared to the HP1α KD. For the same loading rate (0.5 μm/s), the apparent elastic moduli determined using OT ((164 ± 8) Pa (lateral) and (168 ± 12) Pa (longitudinal) for the control, (40 ± 3) Pa (lateral) and (54 ± 5) Pa (longitudinal) for the HP1αKD) are much smaller than AFM values ((22.23 ± 2.12) kPa for the control, (2.13 ± 0.24) kPa for the HP1αKD). Here, uncertainties indicate standard errors in the mean. A similar difference in moduli measured by AFM and

OT has been reported for MC3T3-E1 osteoblasts and MLO-Y4 osteocyte cells isolated from fetal chicken calvariae (Nawaz et al., 2012; Bacabac et al., 2008) and for breast cancer cell lines (Coceano et al., 2015) and has been discussed at the beginning of this chapter. The difference is mainly due to the vast difference in the magnitude of the forces applied as shown in Fig. 5.13. The OT is capable of measuring an apparent modulus at an indentation length for which AFM is unable to conclusively report that contact has been made (Fig.5.17(b)).

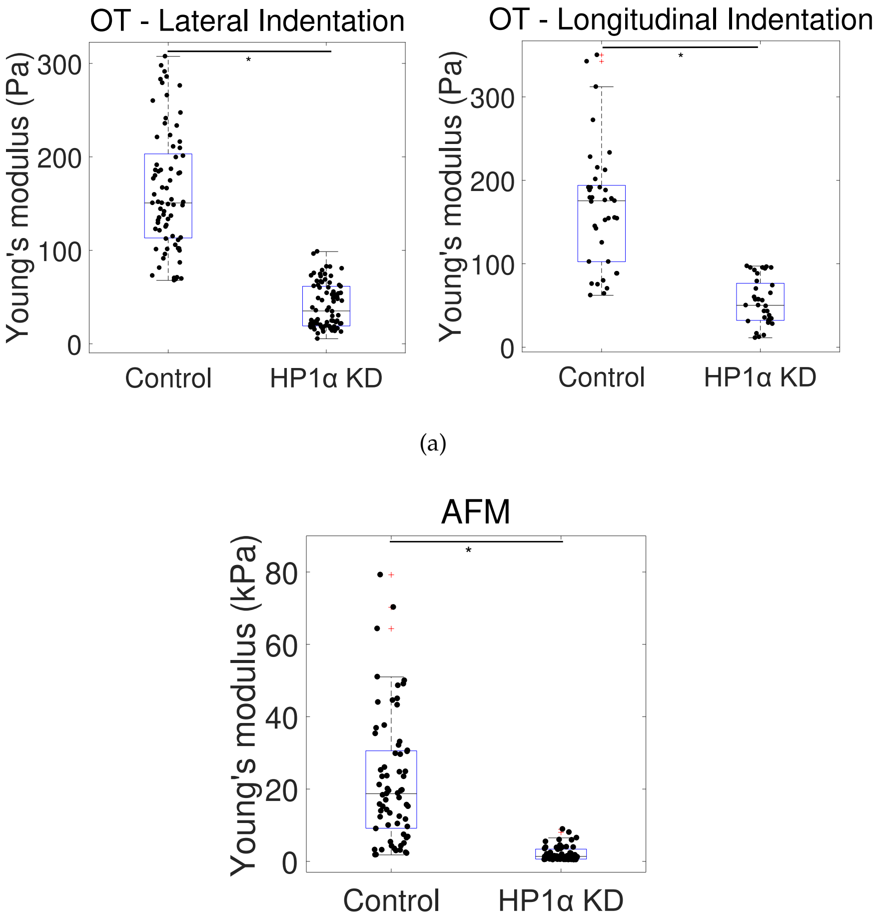

(a)

(b)

FIGURE 5.14: Box plot representation of Young's modulus values measured using OT and AFM (*$p < 0.0001$). (a) Young's modulus obtained for lateral (from the side) and longitudinal (from the top) indentation using OT (n = 73 (control - lateral indentation), 64 (HP1α KD - lateral indentation), 38 (control - longitudinal indentation), 32 (HP1α KD - longitudinal indentation)). (b) Young's modulus obtained using AFM data for a maximum force of 0.5 nN (n = 67 (control), 64 (HP1α KD)). The 'n' indicates total number of indentations performed to obtain modulus values.

5.4.6 MA deformation experiments on MCF-7 nuclei

In contrast to OT and AFM, where the nuclei are deformed locally, MA experiments deform the nuclei globally as it is aspirated into the pipette. Two models (solid and viscoelastic) as described in section 2.4.1 of chapter 2 are used to quantify the mechanical properties of nuclei. The solid model relies on an optical microscope image to analyse the total aspirated length as shown in Fig. 5.15 (Bottom image). The second model is developed for viscoelastic particles, where a change in current at time ΔT (when the nucleus is being aspirated) is used to determine the mechanical properties as shown in Fig. 5.15 (Top figure).

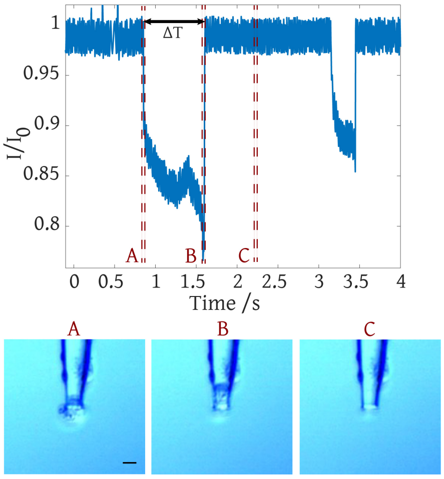

FIGURE 5.15: Example of an experimental current trace showing two aspiration events, and (Bottom) the corresponding video frames for the first event where frame **A** is the first frame of aspiration, frame **B** is the last frame of aspiration, and frame **C** is when no aspiration is occurring. Scale bar : 5mum

5.4.7 Nuclei from HP1α knock-down and control cells have similar bulk properties as determined by micropipette experiments

Micropipette measurements are different in nature from OT and AFM because the test involves deformation of the whole nucleus as opposed to the local deformations of the outer regions of the nuclei that are imposed by OT and AFM. Much greater forces and strains are applied, and the applied deformation includes both the bulk of the chromatin interior and the response of lamins. In contrast, only a small area of the outer region of the nucleus is locally deformed when using a micron-sized indentor bead, so that the results obtained for effective Young's modulus from micropipette (Fig. 5.16) are not expected to be directly comparable to OT and AFM data. The values obtained in Fig. 5.16 can be seen to lie between those obtained using OT and AFM in Fig. 5.14. The apparent Young's moduli obtained using the solid model are similar ((1.56 ± 0.10) kPa for the control, (1.95 ± 0.10) kPa for the HP1α KD), but slightly larger ($p < 0.05$) for the nuclei extracted from the HP1α KD cells. Similarly, results from the viscoelastic model indicate that the control nuclei are less stiff ((220 ± 90) Pa compared with (690 ± 180) Pa) with lower effective viscosity ((7 ± 3) Pa s compared with (22 ± 6) Pa s) than the HP1α KD nuclei as shown in Fig 5.16(c). Here, uncertainties indicate standard errors in the mean.

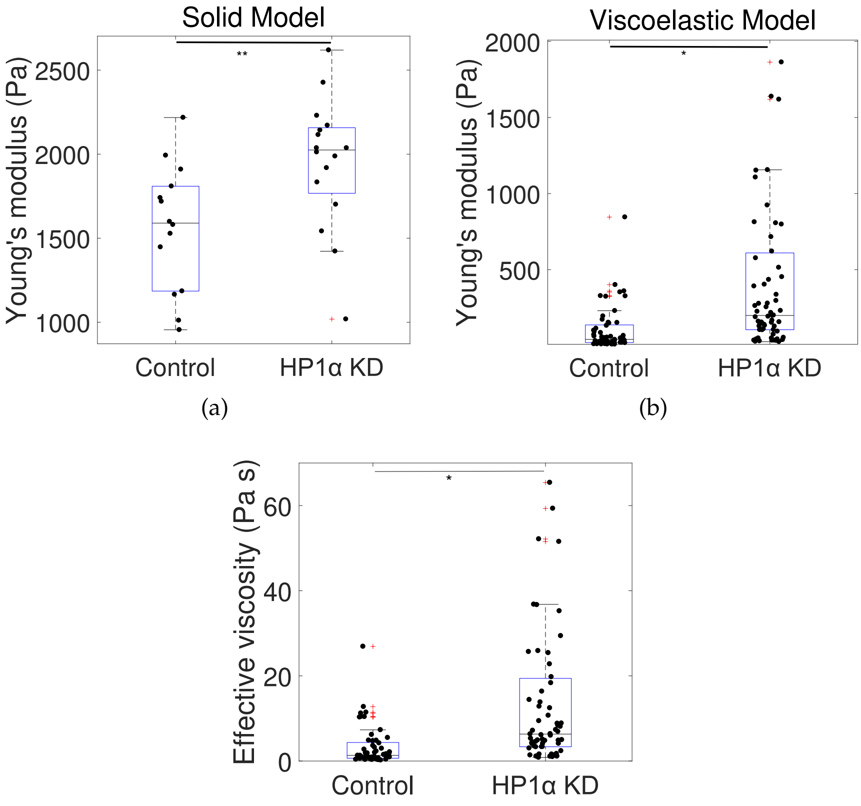

(a) (b)

(c)

FIGURE 5.16: Effective Young's modulus and effective viscosity from microaspiration experiments. (a) Values obtained using the solid model (Eq. 2.28, $^{**}p < 0.01$) ($n = 14$ (control), 16 (KD)). (b) Values obtained using the viscoelastic model (Eq. 2.30, $^{*}p < 0.05$) ($n = 61$ (control), 67 (KD). (c) Comparison of Effective viscosity for the viscoelastic model for control and HP1α KD whole MCF7 cells ($^{*}p < 0.05$)).

A likely explanation for this difference involves deformation of the bulk, and it is possible that the bulk mechanical properties of HP1α KD nuclei are a little higher than those for control nuclei (in contrast to the results for the local indentation of the outer regions). It is also likely that lamins are playing a role in these high strain experiments (Stephens et al., 2017a). Indeed, previous work concluded that while chromatin affects the mechanical response of nuclei at short extensions (< 3 μm, or 30% strain), the lamina has a significant affect at larger extensions Stephens et al., 2018; Stephens et al., 2017a.

It is worth revisiting the two models used to obtain the data shown in Fig. 5.16 for the micropipette experiments, both of which give values that are intermediate between the AFM and OT results. Data obtained using the solid model are greater and closer to the AFM values. This may be because the solid model only analyses small initial deformations that may be less affected by the bulk properties of the nuclei. In contrast, the viscoelastic model uses the entire duration of the deformation and incorporates stress relaxation. Moreover, the solid model may be slightly high due to the geometric factors in equation 2.28, as explained by Aoki et al. (Aoki et al., 1997). The differences in the extracted parameters (both between the two models and with the other techniques) demonstrate that attention must be paid to the details of the analysis method, and not just the experimental technique, when comparing absolute measurements of bioparticles. It is therefore appropriate to designate the data presented in Fig. 5.16 as 'effective' parameters. Nevertheless, the comparison between particle types is not so reliant on modelling assumptions.

5.5 Conclusion

In this chapter, we have studied the mechanical properties of nuclei isolated from MCF7 cells with constitutive KD of HP1α expression using three mechanical measurement techniques which deform the nuclei in very different ways. They probe the outer regions of the nucleus ($\sim$ 100 nm) with forces on scales of 10 pN (OT) or 1 nN (AFM); and alternatively the bulk properties with whole-of-nucleus deformations (micropipette). While OT and AFM both locally probe the nuclear periphery, AFM experiments were carried out at higher forces compared to OT and care must be taken when interpreting the absolute indentation (Bacabac et al., 2008). Absolute values of

Young's modulus obtained using these three techniques are not in close agreement, as might be expected (Wu et al., 2018). This highlights that mechanical measurements carried out on nuclei are difficult because they are viscoelastic and heterogeneous.

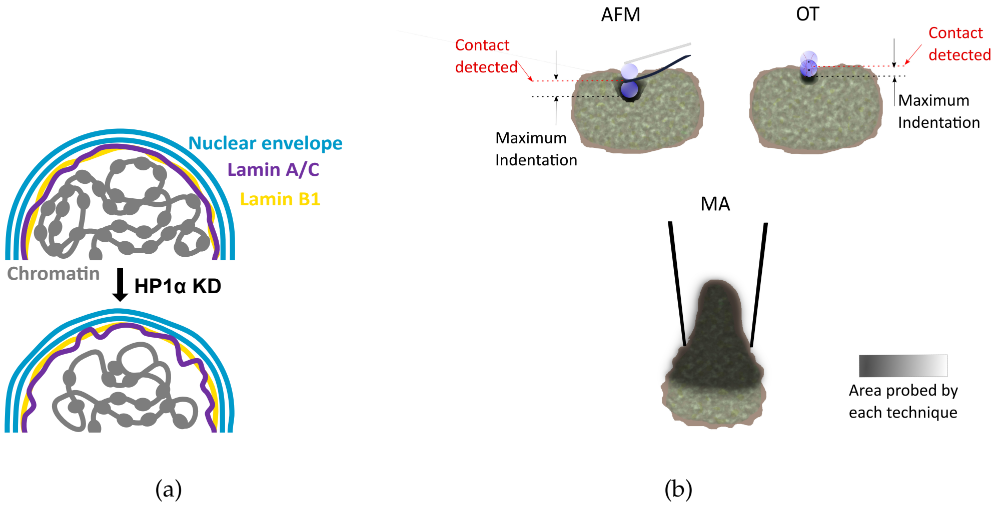

(a) (b)

FIGURE 5.17: (a) Schematic diagram showing the disruption to the nuclear periphery when HP1α expression is reduced. Loss of HP1α disturbs the organisation of heterochromatin, disrupting its tethering to the nuclear lamina and causing a change in the dynamics of the lamina. These changes result in a nucleus with a more malleable shell. (b) Schematic showing the difference in contact point using AFM and OT (local deformation) and larger area probed using MA (global deformation).

Despite the inherent approximations of the analysis, data from indentation techniques (AFM and OT) demonstrate that there is a significant decrease in the apparent Young's modulus of the MCF7 HP1α KD cells compared to control nuclei, reflecting the altered organisation of the peripheral heterochromatin and changes in Lamin A/C dynamics observed in these nuclei. The reduced variation of mechanical values for HP1α KD nuclei is consistent with the more homogeneous chromatin organisation and disruption of the peripheral heterochromatin in HP1α KD nuclei (Fig. 5.17(a)). In contrast, the bulk moduli obtained by micropipette experiments show little difference, with the nuclear interior and stretched lamin networks potentially playing a larger role.

More specifically, the disruption to the heterochromatin upon HP1α KD correlates with the reduced elastic modulus of the periphery of the HP1α KD nuclei. Considering the higher magnitude of force applied by AFM compared with OT, it is likely that the higher apparent magnitude of the moduli originates from engaging more of the adjacent lamina shell in the more extreme local deformation. In contrast, OT is mostly probing the extremities of the nucleus (Fig. 5.17(b)) and is capable of reporting absolute indentations at much lower forces (Fig. 5.13).

Chapter 6

Interaction of milk fat globule membrane with *Lactobacillus fermentus* strains (1485 and 1487) using Optical Tweezers

This chapter reports on a side project performed in collaboration with Dr. Caroline Thum, Agresearch. Caroline and their group were interested in understanding the outer cell membrane properties of two bacterial strains (Lactobacillus fermentum strains - 1487 and 1485) and their interactions with milk fat globule membrane (MFGM) using optical tweezers in our group. The difference in bacterial cell surface properties of these two strains and its effects on intestinal epithelial barrier integrity has already been studied by their group (Sengupta et al., 2015). The primary aim of this project was to measure the adhesion force between bacterial strains and MFGM using OT, inspired from the methodologies conducted by Jiménez-Flores et al., 2010.

6.1 Introduction

Milk fat is secreted from the mammary gland in milk fat globules composed of a triacylglycerol core covered by a tri-layer membrane and the milk fat globule membrane (MFGM) (Kosmerl et al., 2021; Zhang et al., 2020).

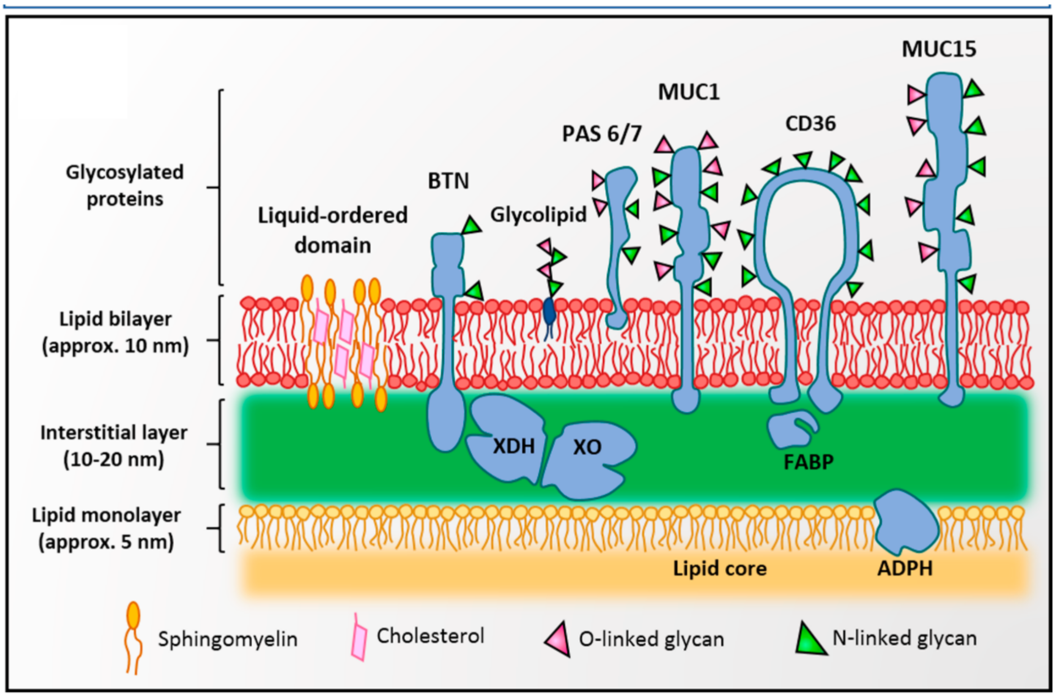

FIGURE 6.1: The structure of the milk fat globule membrane (MFGM) where the different layers and their general compositions are depicted. Figure extracted from Kosmer et al. (Kosmerl et al., 2021).

Part of dietary MFGM was shown to resist digestion, but its effect in the large intestine is not fully understood. It has been reported that MFGM can interact with probiotic bacteria forming a physicochemical barrier, improving resistance to digestion. Similarly, the MFGM has also been used in food to inhibit bacterial and viral binding to the intestinal mucosa. Limited information is known about the selectivity, if any, of MFGM adhesion to beneficial and opportunistic bacteria in the large intestine. The results of this investigation will provide insights into the functional characteristics of the MFGM, as well as highlighting the importance of selective bacterial interaction with milk components for the potential development of functional food with relevance to human health. The main goal of this experiment was to compare the force of bacterial adhesion to MFGM using OT. This information can help us gain insight into the probiotic properties or health benefits of 1485 and 1487 bacterial strains. It has been hypothesised that the MFGM's strongly and selectively bind to opportunistic intestinal bacteria.

Materials and Methods

Isolation of milk fat globules

Raw bovine milk samples were collected from Massey University Dairy Farm 4 (Palmerston North, NZ). Milk samples collected from each animal (n = 5) were used as biological replicates and analysed in triplicate. All milk samples were collected into sterile tubes and processed fresh to minimise the problems associated with refrigeration (for example, damage to the MFGM surface). To normalise the difference in globule number and individual variation, an equal amount of cream (approximately 0.3 gm) containing the MFGM was separated from each animal within a group (e.g. fresh and mastitis). In brief, 15 ml of whole milk was centrifuged at 3000 rpm at 25 °C for 15 min to separate cream and skim milk.

6.1.1 Bacterial strains and growth condition

The bacteria evaluated in this study were two strains of *Lactobacillus fermentus*, AGR-1485 and AGR1487. The two bacterial strains used were isolated from saliva swabs of adult human volunteers as previously described (Anderson, Cookson et al. 2010). Ethical approval from the New Zealand Health and Disability Committee was not required due to the non-invasive nature of the sampling and the healthy status of the volunteers. Written consent for collection and use of the samples for research purposes was obtained from the volunteers. AGR1485 was isolated from a healthy individual and AGR1487 was isolated from a then apparently healthy individual who was later diagnosed with inflammatory bowel disease (IBD). All bacterial strains were grown in MRS broth (Difco, Detroit, MI) at 37 °C. For all experiments, cultures were inoculated 2:100 (v/v) in MRS medium (5 mL) and allowed to grow for 24 hrs. The bacteria were washed twice with 1X PBS buffer by centrifuging at 2000 rpm for 5 min.

6.1.2 Optical Tweezers setup

Experiments were carried out as described in the sections 2.2 of chapter 2 and 4.2.2 of chapter 4. The experiments were carried out at two different temperatures (21 °C and 37 °C). Physiological condition (37 °C) was maintained using a home-built Peltier setup as described in section 4.2.3.1 of chapter 4.

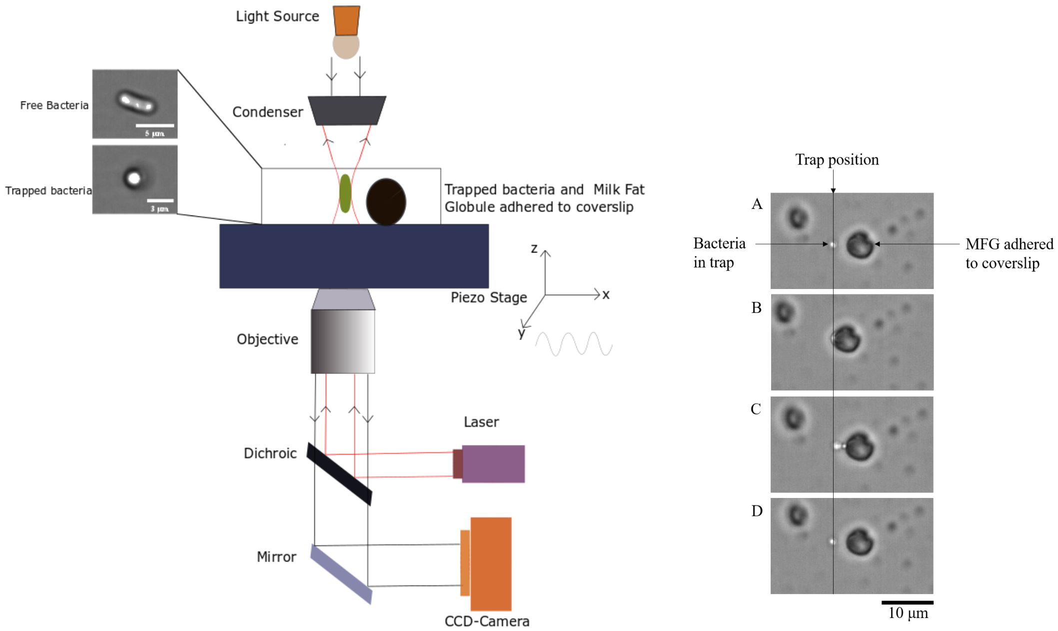

(a) (b)

FIGURE 6.2: Adhesion force experiments and analysis. (a) Schematic setup for the binding force measurements. (b) Image sequence of force measurement procedure. [A] Bacteria in trap and MFGM adhered to the coverslip are few microns apart. The black line shows the position of the trap which is fixed. [B] MFGM is brought into in contact with bacteria by using a piezo stage. [C] Attachment has occurred and the bacterium is being pulled from the MFGM by adjusting the laser power until we can see the elongation. [D] Bacteria has detached from the MFGM.

6.1.3 Investigation of bacterial adhesion to milk fat globules

Firstly, a mixture of 50 μL of diluted cream (1:100 v/v in PBS), 50 μL of bacterial strain preparation (1:200 v/v in PBS), and 10μL of MFGM were pippeted into a welled microscope slide and sealed with a coverslip. The slides were left for 15 minutes with the coverslip facing up, allowing the MFGM to rise towards the top and adhere to the coverslip. The slides were turned upside down and were then placed in the piezo stage. Experiments were initially carried out at room temperature (21 °C). A single bacterium was found and trapped in the OT. The rod- shaped bacteria was aligned by the laser with their long axes perpendicular to the coverslip. The trapped bacterium appears like a dot when trapped and viewed 'end-on' as shown in the figure 6.2(a) .

In the moving piezo stage, the MFGM, which is adhered to the coverslip, was moved towards the trapped bacterium. The bacteria and MFGM were left in contact for approximately 1-2 minutes. To see if binding occurred, the stage was moved slowly

(0.5 μm/s) away. The bacterium becomes clearly elongated if significant adhesion has taken place 6.2(b). There were many failed attempts before binding occurred. Multiple attachment attempts at different positions on the surface of the MFGM were carried out and if no binding occurred, different pairs of bacteria and MFGM were chosen. Once binding occurred, the trap strength was slowly increased by increasing the laser power and the stage was moved slowly in steps of 0.5 μm/s, observing if detachment of the bacteria and MFGM occurs. The laser power was increased in steps of 30 mW to find the laser power where the trap was strong enough to pull the MFGM from the bacteria and detachment occurred. The experiment was performed within approximately 5 min once attachment between MFGM and the bacterium occurred. With multiple trials, the adhesion was found to be a function of time and separation. This procedure of measuring the right laser power for bacteria detachment from MFGM was performed multiple times.

6.1.4 Force Measurement procedure

After obtaining the laser power required for detachment, we measured the equivalent trap strength using the Stokes-drag method (Neuman and Block, 2004). In short, the trapped bacteria was moved approximately 20 μm away from the MFGM. The stage was then set into a sinusoidal motion with a set frequency of 80 Hz for *L. fermentus* 1485 and 90 Hz for *L. fermentus* 1487 (80 Hz oscillation frequency was not sufficient for the 1487 strain to escape out of the trap). The amplitude was increased slowly until the bacteria just escaped from the trap. After determining the amplitude (A) at the bacteria escape point, the maximum drag velocity could be extracted using the equation :

$$v = 6\pi f A \tag{6.1}$$

The drag force is calculated using this velocity considering the bacterium is a straight, slender cylindrical rod with length greater than width. The drag force is given by (Jiménez-Flores et al., 2010) as:

$$F = \frac{2\pi\eta l v}{ln(1/r) - 0.81} \tag{6.2}$$

where η is the viscosity of PBS (0.001 Pa.s Yeom, Kang, and Lee, 2014), l is the length ((5 ± 3) μm) and r is the radius ((0.325 ± 0.2) μm) of the bacteria.

6.2 Results and Discussions

Relationship between exerted Force and Laser Power

Using the Stokes law, the force exerted on the bacteria as a function of laser power was measured. The force exerted on the trapped bacteria is directly related to the laser power. The relationship was found to be linear as shown in Figs. 6.3(a) and 6.3(b) for 21 °C and 37 °C respectively. To remove the bacteria from the trap as the power was increased from 0.2 W to 2 W, the amplitude also had to be increased as shown in equation 6.1 and 6.2 from 10 μm to 70 μm respectively (frequency is constant) i.e, with increasing laser power, more shaking (increasing amplitude of oscillation) is required to remove the bacteria out of the trap and this hydrodynamic friction generates the force.

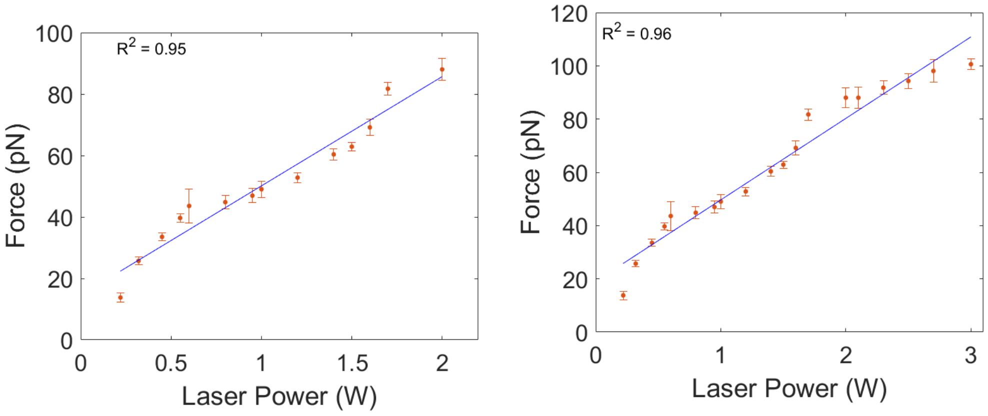

(a) (b)

FIGURE 6.3: Measured force generated by the drag force on a trapped bacteria as a function of laser power for experiments that were carried out at (a) 21 °C and (b) 37 °C. Error bar represents standard error in the mean.

6.2.1 Comparison of adhesion force between 1485 and 1487 bacterial strains

Measurement of adhesion force for AGR1485 (n=10) and AGR1487 (n=11) strains with MFGM was conducted at both room temperature (21 °C) and physiological temperature (37 °C). Fig. 6.4 shows box plot distribution comparing adhesion forces for the two strains performed at (21 °C) (Fig.6.4(b)) and (37 °C) (Fig.6.4(b)). At 21 °C, the values of adhesion forces were measured to be (34 ± 2) pN (for AGR1485) and (66 ± 2) pN (for AGR1487) whereas at 37 °C, the values of adhesion forces were (47 ± 7) pN (for 1485) and (66 ± 9) pN (for 1487) Paired t-test shows a significant difference between the two bacteria types ($p < 0.001$). The error represents SE.

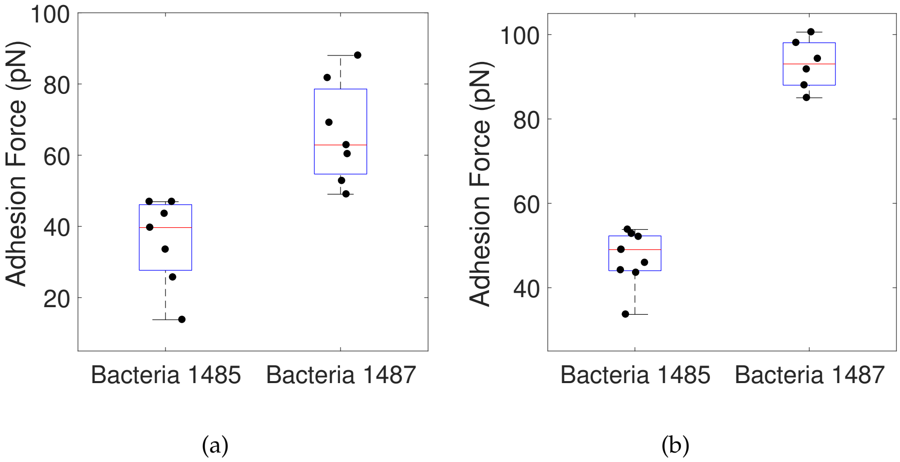

(a)

(b)

FIGURE 6.4: Adhesion force comparison for 1485 and 1487 bacterial strain for experiments carried out at (a) 21 °C and (b) 37 °C. A paired t-test shows significant difference ($p < 0.001$).

Using Stokes Drag equation, we can calculate the force exerted on a trapped bacterium as the laser power is changed and therefore measure the force of bacterial adhesion. The adhesion measurement has a significant dependence on time of contact and separation. We observed that once a bond is formed between MFGM and bacteria, experiments should be done within approximately 5 minutes. One reason for this is that the bacteria may orient toward the MFGM and OT may not be able to trap the bacteria. Therefore, a practical criterion of 5 minutes was chosen for bond formation to occur for both types of bacteria. This was also observed when measuring adhesion forces for eukaryotic cells using trapped spherical beads (Khalili and Ahmad, 2015).

6.3 Conclusion

This study developed a method to measure the relative differences in the the interaction force between two Lactobacillus strains and MFGM. Results suggest that L. fermentus AGR1487 strongly interacts with MFGM compared to AGR1485. The different force interactions observed between MFGM and the Lactobacillus strains indicate that differences in the components on the surface of MFGM or/and bacteria may mediate bacterial-MFGM interactions. However, further studies will need to be undertaken to identify the components on the surface that are responsible for this interaction and to confirm that other beneficial and opportunistic bacteria bind differently to MFGM.

Chapter 7

Summary and Future Work

7.1 Scope of thesis

The general aim of the thesis was to explore the various possible ways to test the mechanical properties of different biological and viscoelastic systems. There are several biophysical techniques available as discussed in Chapter 1, which can be used to study the viscoelastic properties of the system. Each of them has its own pros and cons. Hence, choosing the right technique is of major importance when experimenting on biological systems. Most of the research probing such systems to date has used a single technique to understand the mechanical properties. There are only a handful of research articles where multiple techniques are used on the same system. This thesis investigates the mechanical properties of MCF7 breast cancer cells and their isolated nuclei using OT, AFM, and MA. Using multiple techniques gives an insight into different responses on different lengths and time scales, which is an added advantage compared to a single technique approach. Adhesion forces between bacterial strains and MFGM were also investigated as a side project using an OT technique.

7.2 Summary

Chapter 1 sets the scene for the background and introduction to rheology, microrheology, and cell mechanics. A comparison of different techniques used to probe cells are discussed in this chapter.

Chapter 2 introduces to the biophysical methods used in this thesis. Multiple particle tracking is demonstrated using a CCD camera with a standard glycerol water solution. Calibration of OT in Milli-Q water was carried out using equipartation and power spectrum methods using a QPD. AFM was discussed for force measurements and the use of MA to aspirate and extract the elasticity of bioparticles was described using solid and viscoelastic models.

Chapter 3 focuses on a model complex or viscoelastic fluid (PEO solution) as this is one most important systems to be familiar with to help with in understanding the mechanical properties of cells. Bulk rheology of PEO is compared with passive microrheology which shows a reasonable overlap in the measured modulus values. Active microrheology is carried out using an OT technique where the probe particles are driven by an externally oscillating stage. Calibration of OT in a viscoelastic environment is achieved, which is a prerequisite for extracting viscoelatic moduli using an active microrheology technique.

Chapter 4 is dedicated to understanding the mechanical properties of MCF7 breast cancer cells from control and HP1α depleted cells using an OT technique. This is achieved in two different approaches. Firstly, OT are used to indent cells and measure elasticity, similar to AFM measurements. The elastic modulus distribution showed that control cells ((117±38) Pa) were stiffer compared to HP1αKD cells ((63±27) Pa). Secondly, membrane tethers are pulled out from the cell surface using OT and used to measure the membrane tension of control cells, HP1αKD cells, and cell shed vesicles. Membrane tension values [vesicles ((0.9±0.1) N/m) < HP1αKD cells ((2.7±0.4) N/m) < control cells ((3.8±0.9) N/m)] showed that the cell shed vesicles and HP1αKD cells have reduced membrane tension compared to control MCF7 cells.

Chapter 5 investigates further the mechanical properties of MCF7 cells by isolating the nuclei and performing mechanical measurements using AFM, OT, and MA techniques. This chapter highlights the application of multiple techniques to isolated control and HP1αKD nuclei. For the same loading rate (0.5 μm/s), the apparent elastic moduli determined using OT ((164 ± 8) Pa (lateral) and (168 ± 12) Pa (longitudinal) for the control, (40 ± 3) Pa (lateral) and (54 ± 5) Pa (longitudinal) for the HP1αKD) are much smaller than AFM values ((22.23 ± 2.12) kPa for the control, (2.13 ± 0.24) kPa for the HP1αKD). However, MA results showed the opposite trend in elasticity values. The apparent Young's moduli obtained using the solid model are similar ((1.56 ± 0.10) kPa for the control, (1.95 ± 0.10) kPa for the HP1α KD), but slightly larger ($p < 0.05$) for the nuclei extracted from the HP1α KD cells. Similarly, results from the viscoelastic model indicate that the control nuclei are less stiff ((220 ± 90) Pa compared with (690 ± 180) Pa) with lower effective viscosity ((7 ± 3) Pa s compared with (22 ± 6) Pa s) than the HP1α KD nuclei. One of the possible reasons is due to the stretching of lamins at long extensions as described in the literature (Stephens et al., 2017a; Dahl et al., 2004). Confocal microscopy imaging, SEM and immunoblot analysis reveals that a disruption of the heterochromatin upon HP1αKD correlates with reduced elastic modulus of the periphery of the HP1αKD nuclei.

Chapter 6 describes the use of OT in measuring differences in adhesion forces between two bacterial strains (AGR1485 and AGR1487) with MFGM at 21 °C and 37 °C. At both temperatures, the results show that AGR1487 more strongly interacts with MFG compared to AGR1485 bacterial strains. At 37 °C, the adhesion force was stronger compared to experiments conducted at 21 °C.

7.3 Future Work

7.3.1 Microrheology experiments

Using PEO, passive microrheology has been explored thoroughly. Since the rigorous foundations of achieving modulus values using active microrheology are laid down in detail, future experiments could be performed at different concentrations and compared with passive microrheology and bulk rheology. This method can also be further applicable in understanding the mechanical properties of living cells which are viscoelastic in nature. One way of performing this is by attaching micro beads to cells which can be used to track or apply forces on membranes by moving the trapped beads at different frequencies using an oscillating piezo stage (active microrheology using OT). This method might provide additional insight into the coupling of membrane, cytoskeleton and nuclear dynamics in different types of cells.

7.3.2 Biophysical techniques measurements

7.3.2.1 Optical Tweezers experiments

The indentation measurements reported herein were carried out using sinusoidal piezo stage oscillations. Future work could be performed using triangular waveforms which can provide a smoother linear variation in time compared to sinusiodal waveforms. Measurements on cells and nuclei were carried out at room temperature, however, future experiments could be performed at physiological temperatures. Room temperature suppresses the activity of the cell cytoskeleton and nuclear protein structures to an extent.

Pulling membrane tethers were performed on control and HP1αKD cells. This technique could be extended to isolated nuclei which can directly provide insight to nuclear membrane tension and its relation to HP1α and lamina proteins inside the nucleus. Pulling a membrane tether to different lengths and analyzing the relaxation time scales can provide insight into the diffusion of lipids at different tether lengths.

To understand the interaction between MFGM and bacterial strains better, the surface properties of bacteria and MFG as a function of temperature needs to be explored.

7.3.2.2 AFM and MA experiments

Similarly, both AFM and MA experiments could be carried out at physiological temperatures. As both the AFM and MA measurements were carried out on nuclei, future work could be extended to whole cells and could be used to compare with OT experiments.

7.3.3 Biological experiments

As reported in the literature, chromatin and lamins determine two different mechanical response regimes of the nucleus, which is also evident from MA experiments at larger deformation. Future experiments can also be targeted at depleting lamins along with HP1α proteins and looking at mechanical responses at long extensions.

Chapter 8

Published and to be published work

1. Depletion of HP1α alters the mechanical properties of MCF7 nuclei.
   Susav Pradhan, Raoul Solomon, Ankita Gangotra, Gleb E Yakubov, Geoff R Willmott, Catherine P Whitby, Tracy K Hale, Martin AK Williams.
   In: *Biophysical Journal*. Received 23 September 2020, Accepted 14 May 2021. In Press, Journal Pre-proof.

2. Applications of Microrheology to Food Systems.
   Susav Pradhan, Catherine P. Whitby, Martin A.K. Williams.
   In: *Encyclopedia of Food Chemistry*, Academic Press, 2019, Pages 130-133, ISBN 9780128140451.

3. Membrane tether dynamics of HP1α depleted MCF7 cells.
   to be submitted.

4. Interactions of milk fat globule with L. fermentus AGR1487 and AGR1485 using optical tweezers reveal novel probiotic properties.
   to be submitted.

Appendix A

Application of microrheology to food and biological systems

Food colloidal systems such as emulsions, foams, and gels are typical complex systems consisting of multiple components and multiple phases in various stages of organization. The mechanical properties associated with complex structures with multiple characteristic lengths and timescales are of major importance for food scientists. Their macroscopic properties, for example, stability and texture, are closely related to their structure and mechanical properties at the microlevel.

The majority of foods are emulsions such as milk, sauces, butter, and margarine. Foods such as yogurt and cheese are soft solids in highly viscoelastic states. Food emulsions and gels exhibit a great diversity of rheological characteristics, ranging from low-viscosity Newtonian liquids (e.g., milk), to viscoelastic materials, exhibiting both a viscous and an elastic response to stress (e.g., salad dressings, cream). These foods are inhomogeneous solutions that drip and splatter when poured, rather than flowing steadily. They show complex time-dependent responses to mechanical stress at the micrometer scale. Their flow behavior is complicated by the presence of nanometre and micrometre-sized structures formed by proteins, polysaccharides, and lipids.

In recent years, significant progress has been made in the development of techniques to study and characterize the structure and dynamics of complex fluids at the microscopic level and this field of study is known as 'microrheology'. Microrheology is the collective name for a relatively new set of techniques that seek to probe the mechanical properties of soft materials over increasing ranges of time and distance, spanning molecular to macroscopic (Pradhan, Whitby, and Williams, 2018) . They have steadily become more visible in the food science literature as illustrated in figure A.1.

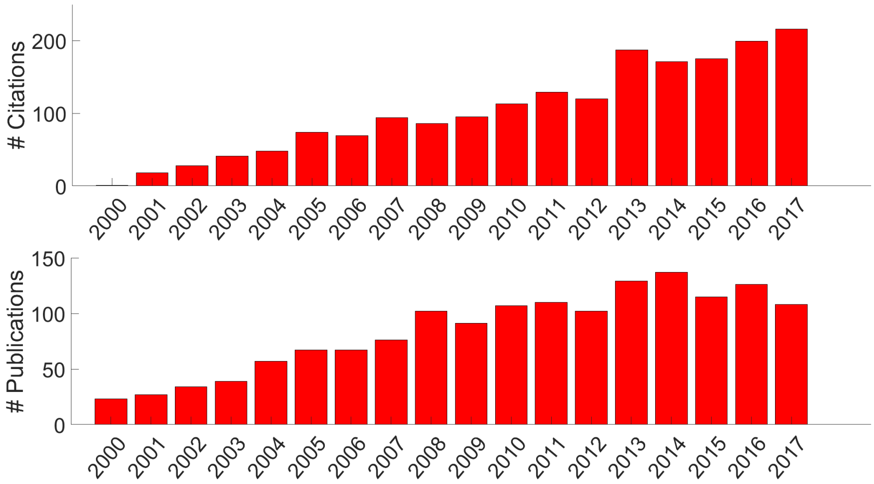

FIGURE A.1: The number of publications since 2000 with "food" and microrheology" listed as keywords and the number of times these publications have been cited. Data from Web of Science, December, 2017.

Microrheology techniques have been used extensively in food science. Moschakis et al. (Moschakis, Murray, and Dickinson, 2006) showed that microrheology can be used as a probe in food colloid studies. They used Multiple Particle Tracking (MPT) to study the structural organization of caseinate-stabilized emulsions containing xanthan (Moschakis, Murray, and Dickinson, 2006) and the gelation of casein proteins (Moschakis, Murray, and Dickinson, 2010). Gelation is a widespread phenomenon occurring in food materials. During gelation, the motion of the embedded tracer particle becomes strongly constrained or trapped, due to the heterogeneity, such as gelation of acid milk gels (Cucheval et al., 2009). The MSD of casein micelles aggregates obtained by diffusive wave spectroscopy (DWS) were compared with the MSD from multiple particle tracking (MPT), with and without k-casein coating. The DWS method was used to understand the microrheology of acid milk gels at short timescales ($10^{-6} s$).

In table A.1 , the most recent articles in which microrheology was used to study food systems are summarized.

TABLE A.1: Microrheology in food systems.

Area of Research	**Method of Rheology**	**Experimental Technique**	**Investigated System**	**Description**	**References**
Viscoelastic Gels and Polymers	Active Microrheology	OT	Collagen Gels	Local shear modulus probed of type I Collagen Gels.	(Velegol and Lanni, 2001a)
				Probing mechanical properties during self-assembly of collagen.	(Shayegan and Forde, 2014)
		Magnetic Nanorods	PF1 gel	Alternating Magnetic Fields to probe magnetic and viscous torques.	(Brasovs et al., 2015)
		AFM & OT	Gelatin	Explore the microscopic response of presheared gelatin from the linear to the nonlinear regime and observe the yielding at the microscale.	(Wilking and Mason, 2008)
				Probing surfaces of swollen gelatin using AFM.	(Benmouna and Johannsmann, 2004)

		OT	Mucus	Mobility of nanoparticles in mucus mesh on different scales.	(Kirch et al., 2012)
				Review of the biochemistry that governs mucus rheology.	(Lai et al., 2009)
	Passive Microrheology	DWS	Pectin	Semi-flexible polysaccharide gels were formed and probed.	(Vincent et al., 2007)
		MPT	Gellan Gum	Probing the effect of a constant applied shear during gelation of aqueous gellan gum.	(Caggioni et al., 2007)
		MPT	β-Glucans	Understanding the sol-gel transition of aqueous barley beta-glucan solutions which undergo gelation with ageing.	(Moschakis, Lazaridou, and Biliaderis, 2012)
		MPT	Wheat gliadin	Probing the microstructural and micromechanical heterogeneities of wheat gliadin suspensions.	(Xu et al., 2002)

		MPT	β-lacto-globulin	Diffusion of fluorescent-labeled dextran in β-lag solutions were investigated.	(Balakrishnan, Durand, and Nicolai, 2011)
				Probing the sol-gel transition in solvent-induced $\vert\beta$-lag gels at room temperature and pH 7.	(Corrigan and Donald, 2009)
		MPT	Gastro-intestinal mucus	The barrier properties of gastrointestinal mucus on particle transport were explored.	(Crater and Carrier, 2010)
				Understanding the colloidal behavior of emulsions stabilized with sodium caseinate (Na-Cas), and interactions in the gastrointestinal environment.	(Macierzanka et al., 2012)
		TPM	Guar Gels	A new method to probe viscoelastic media, based on cross-correlation of two particles, using Guar gels as the model system.	(Crocker et al., 2000)

		DWS	Poly vinyl alcohol gels	The motion of probe particles in aqueous solutions of linear and branched poly(vinyl alcohol) (PVA) and in chemically cross-linked PVA gels has been studied.	(Narita et al., 2001)
Colloidal Systems	Active Micro-rheology	OT	Sodium caseinate-stabilized emulsion droplets	Interaction between a pair of sodium caseinate-stabilized emulsion droplets.	(Griffiths et al., 2016)
	Passive Microrheology	MPT and DWS	Casein acid milk gel	Kinetics of gelation probed.	(Moschakis, Murray, and Dickinson, 2010)
				Heterogenity probed with and without pectin.	(Cucheval et al., 2009)
		MPT	Caseinate-stabilized emulsion	Probing phase separation of caseinated stabilised emulsions containing xanthan.	(Moschakis, Murray, and Dickinson, 2006)
		DWS	Caseinated emulsion	Probing the effect of temperature on sodium caseinated emulsions.	(Eliot, Horne, and Dickinson, 2005)

		DWS	Lutein emulsion	The impact of chitosan on microrheological properties of Stabilised Lutein emulsions probed.	(Xu et al., 2016)
		DWS	β-carotene emulsion	The impact of lactoferrin- chlorogenic acid and Epigallocatechin-3-gallate on the physicochemical properties of β-carotene emulsions.	(Liu et al., 2016)
		DWS	β-lactoglobulin emulsion	Change in phase behaviour by β-lactoglobulin emulsions by varying the long and short attractive interactions.	(Blijdenstein et al., 2003)
				Probing the phase behaviour and mechanical properties stabilised by β-lactoglobutin emulsions and flocculated by the dextran in presence of sucrose.	(Blijdenstein et al., 2004)

Interfaces & Multiphase systems	Active Microrheology	OT	β-lactoglobulin protein	Investigating the β-lactoglobulin adsorbed at a decane-water interface.	(Lee et al., 2010)
				Investigating the mechanical properties of layers of the β-lactoglobulin during their formation at the air-water interface.	(Lee et al., 2011)
		AFM	β-lactoglobulin Fibrils	Correlate the intricate structure of β-lactoglobulin fibril-laden interfaces with their macroscopic adsorption kinetics and viscoelasticity.	(Jordens et al., 2014)
		Magnetic Beads	Microgels	Probing microgels at water-oil interface using magnetic beads.	(Huang et al., 2016)
		OT	Lysozyme protein Layer	Probing the mechanical evolution of layers of protein lysozyme adsorbed at the air-water interface.	(Allan et al., 2014)

Appendix B

Piezo stage and camera Information

B.1 Piezoelectric stage Information

- Stage: PI P-517.3CD (PI).
- Resolution: 3nm.
- Travel: 100 microns.
- Active axis : X,Y,Z.

B.2 Camera Information

- Camera: Andor Neo sCMOS.
- Frame Rate: 100 fps Rolling Shutter - 2560 x 2160 (full frame) & 1,639 fps Rolling Shutter - 128 x 128 ROI.
- Pixels/μm for different microscope objective magnification using Andor Neo sCMOS:

TABLE B.1: Pixels/micrometer conversion.

Setting	**Magnification**	**Pixels/micrometer**	**Error**
20x1	20	3.1	±0.05
20x1.5	30	4.7	±0.07
40x1	40	6.1	±0.09
40x1.5	60	9.3	±0.2
60x1	60	9.2	±0.1
60x1.5	90	13.9	±0.2

B.3 MA setup description table

TABLE B.2: List of hardware modifications and additions for the MA apparatus.

Component	Product	Specifications	Functionality
PXIe Chassis	Express Chassis (PXIe-1071, National Instruments)	4-slot PXIe chassis.	Basic frame for hosting the DAQ and SMU with a processor, separate from main computer.
Processor	Windows/Real-Time Processor (PXIe-8821, National Instruments)	Dual core processor, 2.6 GHz, Intel i3, Windows 10 64-bit and LabVIEW Real-Time operating systems.	Processor for operating the DAQ, SMU, pressure sensor and piezos.
Electrometer (SMU)	Source Measuring Unit (PXIe-4139, National Instruments)	Single channel, 60 V, 10 A source range, 100 fA measurement sensitivity.	Applying voltage between electrodes and measuring current.
Electrometer Adapter	Triax SMU Adapter (SA-413T, National Instruments)	2 triaxial connections and 2 screw terminals.	Connecting triaxial cables to the SMU.
DAQ Card	Multifunction I/O Device (PXIe- 6289, National Instruments)	4 analogue outputs and 32 analogue inputs.	Data acquisition card to interface between the hardware and software components.
Fast Z Piezo (Z+)	Nanocube (P-753.3CD, PI)	Single direction, 38 μm range, 0.2 nm resolution, 1.4-2.9 kHz frequency response.	Additional, fast movement in Z direction.
Fast Z Piezo Servo	Nanocube Piezo Controller (E-625.CR, PI)	Single channel, -30 to 130 V output and -2 to 12 V input voltage.	Controlling the Z+ piezo.
Pressure Sensor	Microfluidic Flow Control System (MFCS-EZ, Fluigent)	2 channels, -800 to 0 mbar and -69 to 0 mbar range, -0.24 mbar and -0.02 mbar resolution, respectively.	Controlling the pressure applied through the pipette.
Pressure Pump	Vacuum Pump (MFCS-EZ Accessory, Fluigent)	-1000 to 0 mbar.	Applying negative pressure.
Pressure Reservoir	Fluiwell (Fluigent)	Custom made for PCR tubes.	Collecting the aspirated fluid.
Horizontal Microscope Objective	Infinity Corrected Long Working distance Objective (100X, Mitutoyo)	13 mm working distance.	Magnifying on horizontal microscope.
Horizontal Microscope Camera	CMOS USB Camera (DCC3240C, Thor Labs)	Global shutter, USB 3.0, 41 frames per second.	For vertical view of the pipette.
Inverted Microscope	CMOS USB Camera, 20X Objective (DCC1645C, Thorlabs)	Rolling shutter, 25 frames per second.	For inverted view of the sample bed.
Sample Holder	Built in-house.	5 ml volume custom built cuboidal glass enclosure.	Electrolyte bath in which the sample substrate is placed.

Appendix C

Additional Nuclei Images

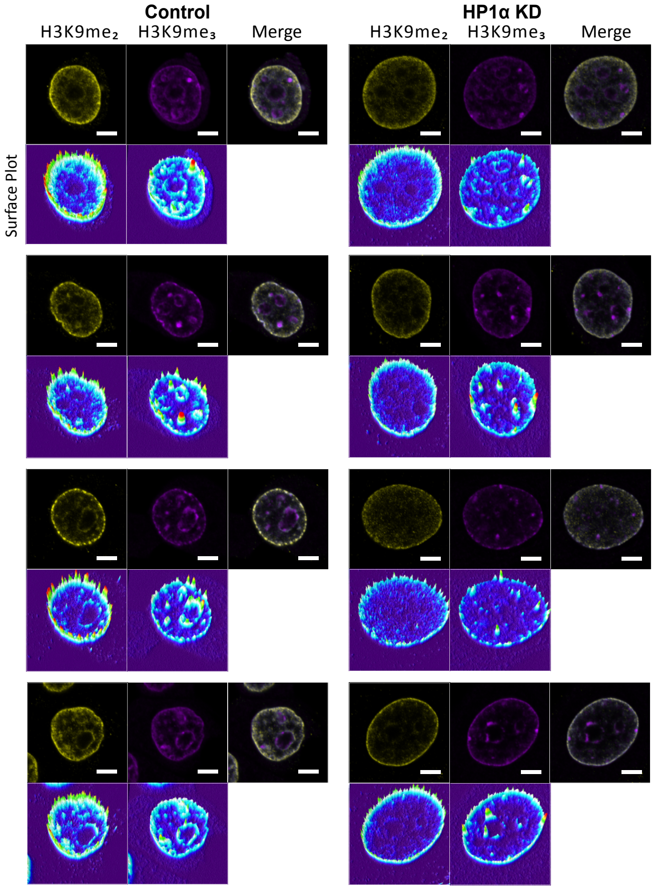

FIGURE C.1: Immunofluorescence confocal microscopy images of MCF7 control and MCF7 HP1α KD cells stained with antibodies against H3K9me2 (*yellow*) and H3K9me3 (*magenta*). Fluorescense surface plots of the medial slices through the nuclei demonstrate the intensity of antibody staining. Scale bars - 5 μm.

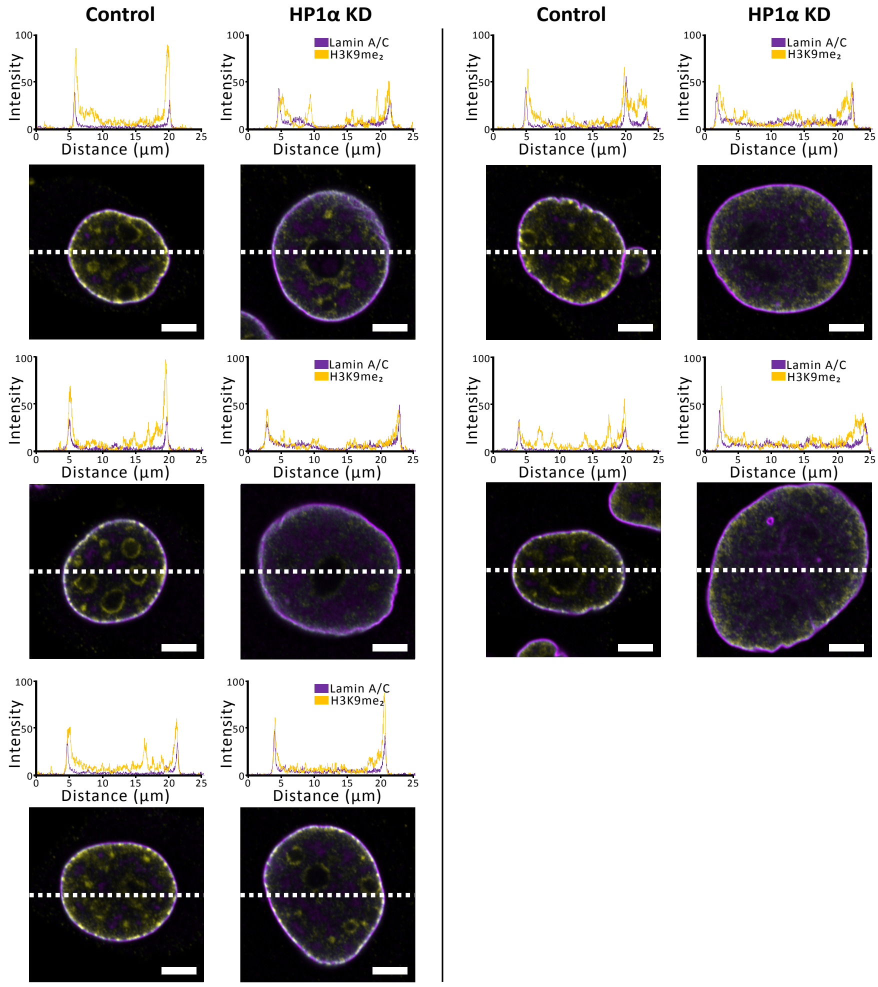

FIGURE C.2: Confocal microscopy medial sections of individual nuclei from MCF7 control and MCF7 HP1α KD cells stained with antibodies against Lamin A/C (*magenta*) and H3K9me2 (*yellow*). Above each medial slice are line plot profiles of fluorescence intensity (percentage of grey value saturation). Scale bars - 5 μm.

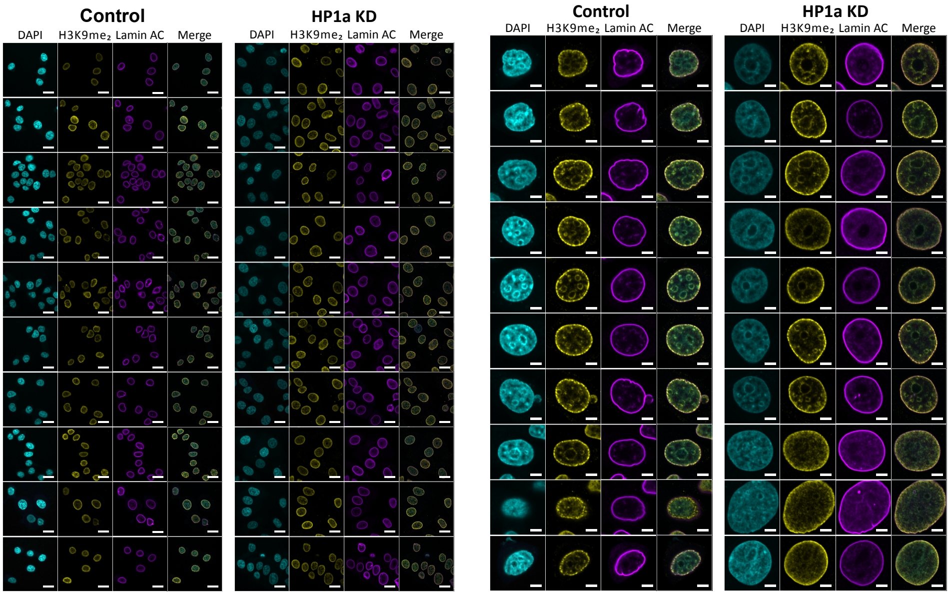

(a) (b)

FIGURE C.3: Confocal microscopy medial sections of MCF7 control and MCF7 HP1α KD cells stained with DAPI to detect DNA (*cyan*) and antibodies against H3K9me2 (*yellow*) and Lamin A/C (*magenta*). (a) Scale bars - 20 μm. (b) Scale bars - 5 μm.

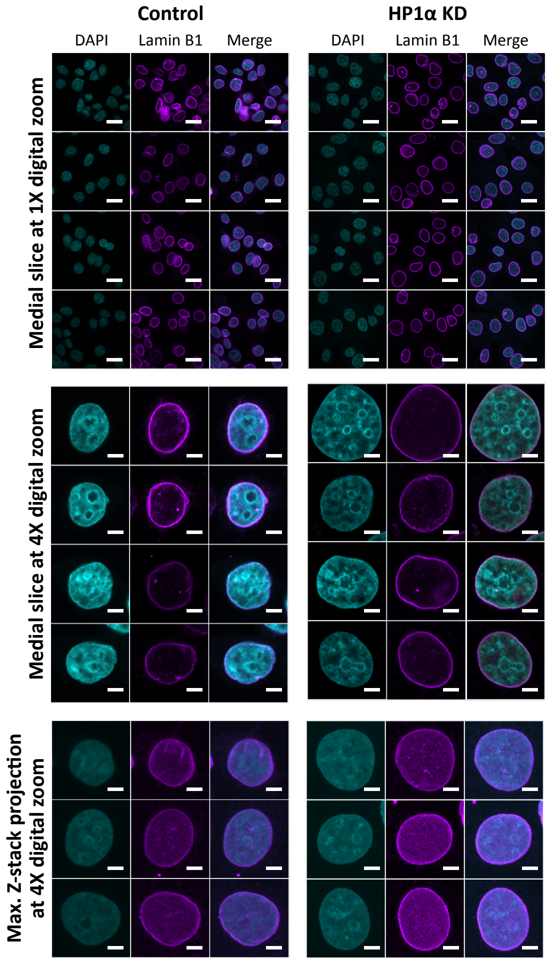

FIGURE C.4: Confocal microscopy images from MCF7 control and MCF7 HP1α KD cells stained with DAPI to detect DNA (*cyan*) and an antibody against Lamin B1 (*magenta*). Top panel, medial slices, scale bars - 20 μm. Middle panel, medial slices at 4x zoom, scale bar - 5 μm. Bottom panel, maximum projection of Z-stacks at 4x zoom, scale bar - 5 μm.

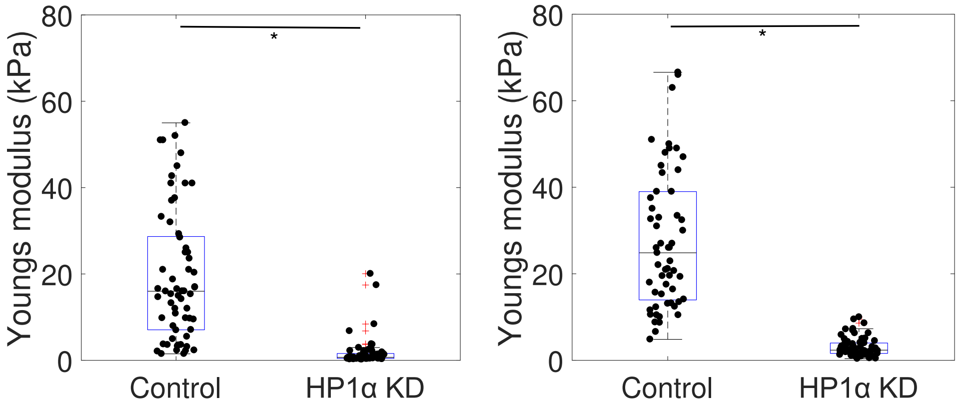

(a)

(b)

FIGURE C.5: Apparent Youngs modulus obtained using AFM data for maximum force of (a) 0.3N and (b) 1nN. $*p < 0.0001$ (two sample t-test).

Appendix D

Statement of Contribution and DRC16 forms

- All the optical tweezers associated experiments and analysis in the entire thesis were performed solely by me.
- I was an active participant in AFM experiments (carried out at the University of Queensland, Australia) and the analysis of the data was carried out by me.
- I was an active participant in MA experiments (carried out at the University of Auckland), and I helped with the analysis of data.
- 'Biological experiments' in chapters 4 and 5, such as cell pass-aging, confocal microscopy, and blots, were carried out by Raoul Solomon and Tracy Hale; however, I was an active participant, for example performing nucleus extraction myself.
- Biological experiments reported in chapter 6 such as handling bacterial strains was carried out by Caroline Thum; however, isolation of MFG and mechanical measurements were carried out by me.

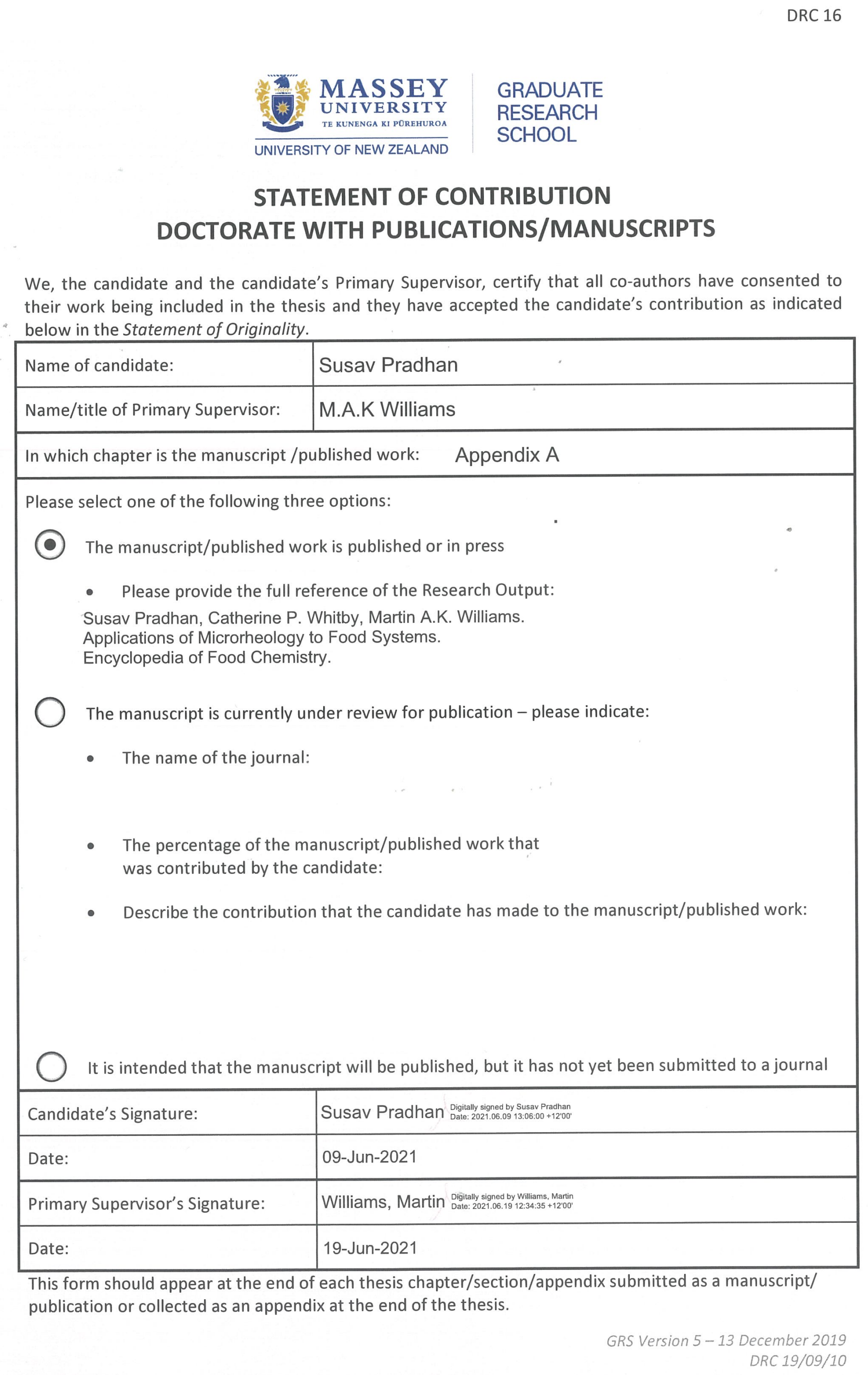

DRC 16

MASSEY UNIVERSITY
TE KUNENGA KI PŪREHUROA
UNIVERSITY OF NEW ZEALAND

GRADUATE
RESEARCH
SCHOOL

STATEMENT OF CONTRIBUTION
DOCTORATE WITH PUBLICATIONS/MANUSCRIPTS

We, the candidate and the candidate's Primary Supervisor, certify that all co-authors have consented to their work being included in the thesis and they have accepted the candidate's contribution as indicated below in the *Statement of Originality*.

Name of candidate:	Susav Pradhan
Name/title of Primary Supervisor:	M.A.K Williams

In which chapter is the manuscript /published work: Appendix A

Please select one of the following three options:

● The manuscript/published work is published or in press

- Please provide the full reference of the Research Output:

Susav Pradhan, Catherine P. Whitby, Martin A.K. Williams.
Applications of Microrheology to Food Systems.
Encyclopedia of Food Chemistry.

○ The manuscript is currently under review for publication – please indicate:

- The name of the journal:
- The percentage of the manuscript/published work that was contributed by the candidate:
- Describe the contribution that the candidate has made to the manuscript/published work:

○ It is intended that the manuscript will be published, but it has not yet been submitted to a journal

Candidate's Signature:	Susav Pradhan Digitally signed by Susav Pradhan Date: 2021.06.09 13:06:00 +12'00'
Date:	09-Jun-2021
Primary Supervisor's Signature:	Williams, Martin Digitally signed by Williams, Martin Date: 2021.06.19 12:34:35 +12'00'
Date:	19-Jun-2021

This form should appear at the end of each thesis chapter/section/appendix submitted as a manuscript/publication or collected as an appendix at the end of the thesis.

GRS Version 5 – 13 December 2019
DRC 19/09/10

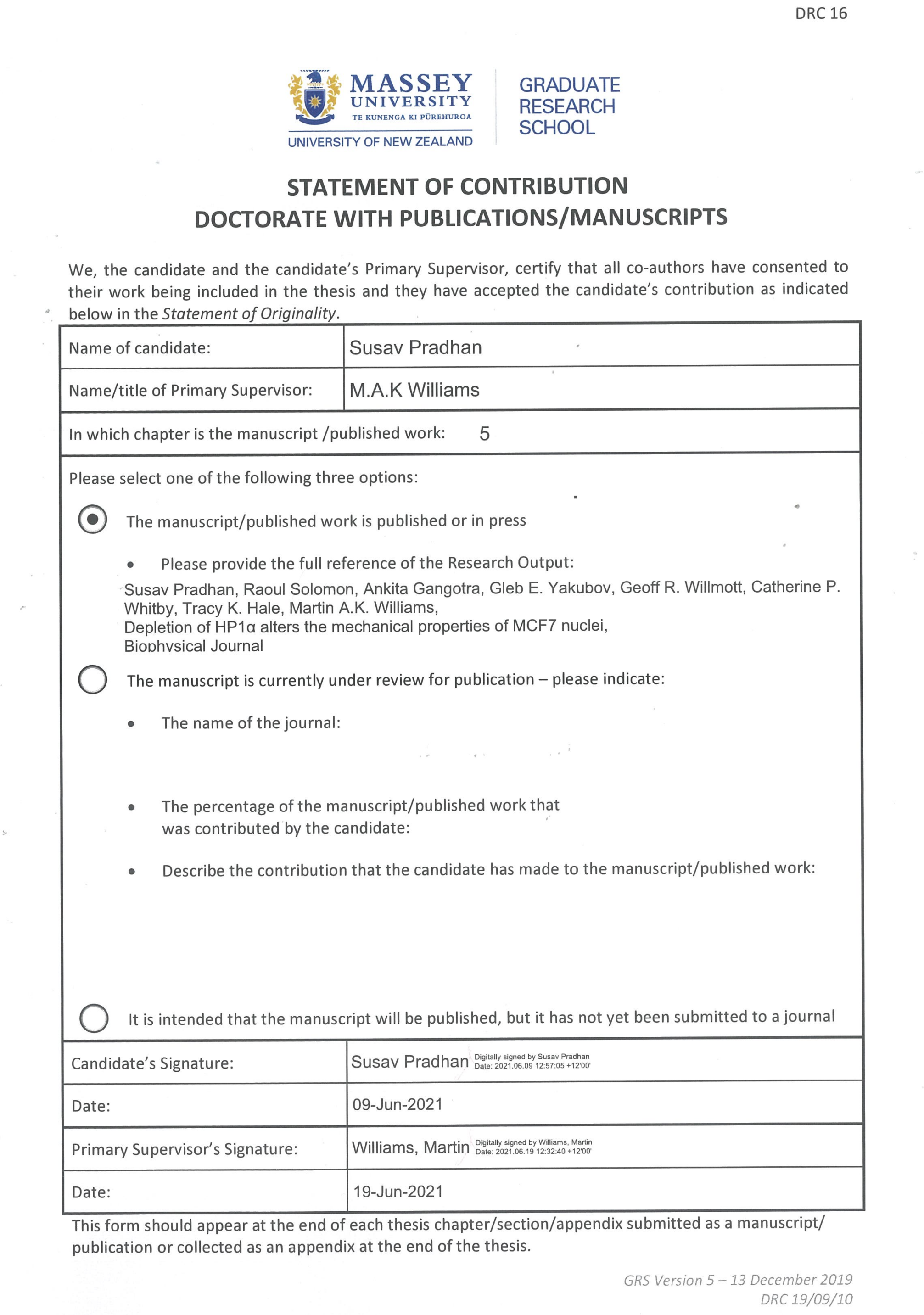

DRC 16

MASSEY UNIVERSITY
TE KUNENGA KI PŪREHUROA
UNIVERSITY OF NEW ZEALAND

GRADUATE RESEARCH SCHOOL

STATEMENT OF CONTRIBUTION
DOCTORATE WITH PUBLICATIONS/MANUSCRIPTS

We, the candidate and the candidate's Primary Supervisor, certify that all co-authors have consented to their work being included in the thesis and they have accepted the candidate's contribution as indicated below in the *Statement of Originality*.

Name of candidate:	Susav Pradhan
Name/title of Primary Supervisor:	M.A.K Williams

In which chapter is the manuscript /published work: 5

Please select one of the following three options:

● The manuscript/published work is published or in press

- Please provide the full reference of the Research Output:

Susav Pradhan, Raoul Solomon, Ankita Gangotra, Gleb E. Yakubov, Geoff R. Willmott, Catherine P. Whitby, Tracy K. Hale, Martin A.K. Williams,
Depletion of HP1α alters the mechanical properties of MCF7 nuclei,
Biophysical Journal

○ The manuscript is currently under review for publication – please indicate:

- The name of the journal:
- The percentage of the manuscript/published work that was contributed by the candidate:
- Describe the contribution that the candidate has made to the manuscript/published work:

○ It is intended that the manuscript will be published, but it has not yet been submitted to a journal

Candidate's Signature:	Susav Pradhan Digitally signed by Susav Pradhan Date: 2021.06.09 12:57:05 +12'00'
Date:	09-Jun-2021
Primary Supervisor's Signature:	Williams, Martin Digitally signed by Williams, Martin Date: 2021.06.19 12:32:40 +12'00'
Date:	19-Jun-2021

This form should appear at the end of each thesis chapter/section/appendix submitted as a manuscript/ publication or collected as an appendix at the end of the thesis.

GRS Version 5 – 13 December 2019
DRC 19/09/10

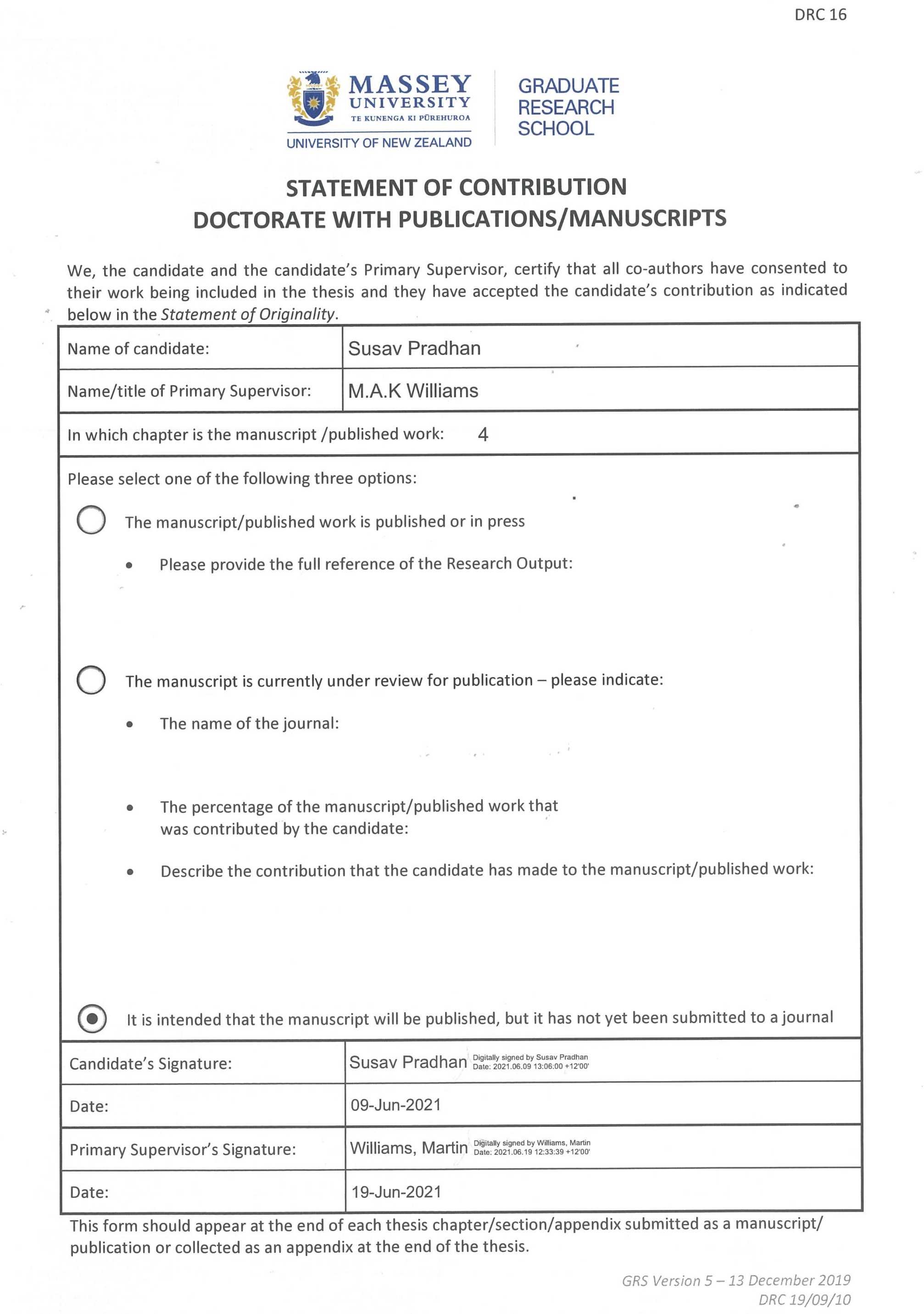

DRC 16

MASSEY UNIVERSITY
TE KUNENGA KI PŪREHUROA
UNIVERSITY OF NEW ZEALAND
GRADUATE RESEARCH SCHOOL

STATEMENT OF CONTRIBUTION
DOCTORATE WITH PUBLICATIONS/MANUSCRIPTS

We, the candidate and the candidate's Primary Supervisor, certify that all co-authors have consented to their work being included in the thesis and they have accepted the candidate's contribution as indicated below in the *Statement of Originality*.

Name of candidate:	Susav Pradhan
Name/title of Primary Supervisor:	M.A.K Williams

In which chapter is the manuscript /published work: 4

Please select one of the following three options:

○ The manuscript/published work is published or in press

- Please provide the full reference of the Research Output:

○ The manuscript is currently under review for publication – please indicate:

- The name of the journal:
- The percentage of the manuscript/published work that was contributed by the candidate:
- Describe the contribution that the candidate has made to the manuscript/published work:

● It is intended that the manuscript will be published, but it has not yet been submitted to a journal

Candidate's Signature:	Susav Pradhan Digitally signed by Susav Pradhan Date: 2021.06.09 13:06:00 +12'00'
Date:	09-Jun-2021
Primary Supervisor's Signature:	Williams, Martin Digitally signed by Williams, Martin Date: 2021.06.19 12:33:39 +12'00'
Date:	19-Jun-2021

This form should appear at the end of each thesis chapter/section/appendix submitted as a manuscript/publication or collected as an appendix at the end of the thesis.

GRS Version 5 – 13 December 2019
DRC 19/09/10

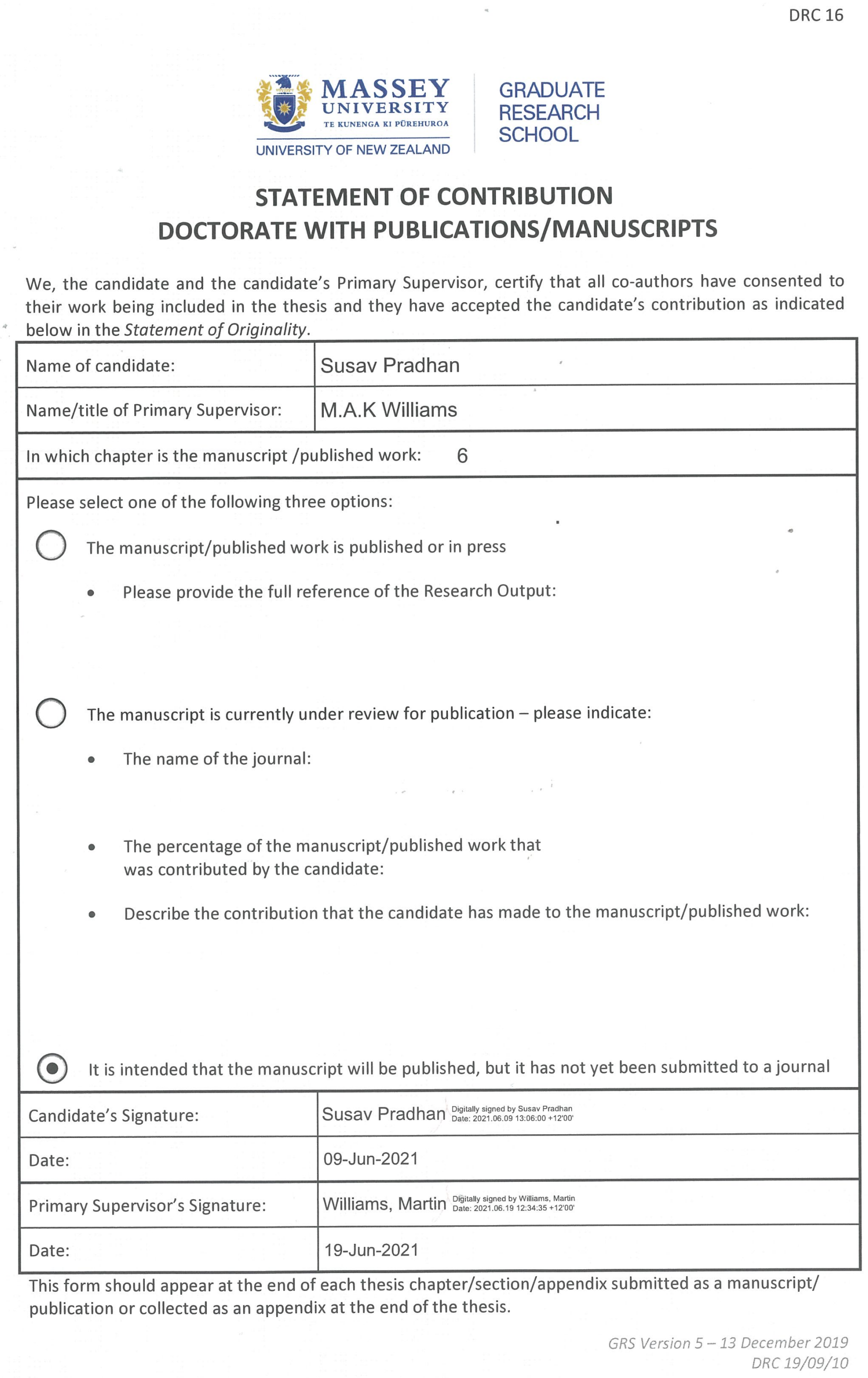

DRC 16

MASSEY UNIVERSITY
TE KUNENGA KI PŪREHUROA
UNIVERSITY OF NEW ZEALAND

GRADUATE
RESEARCH
SCHOOL

STATEMENT OF CONTRIBUTION
DOCTORATE WITH PUBLICATIONS/MANUSCRIPTS

We, the candidate and the candidate's Primary Supervisor, certify that all co-authors have consented to their work being included in the thesis and they have accepted the candidate's contribution as indicated below in the *Statement of Originality*.

Name of candidate:	Susav Pradhan
Name/title of Primary Supervisor:	M.A.K Williams
In which chapter is the manuscript /published work: 6	

Please select one of the following three options:

○ The manuscript/published work is published or in press

- Please provide the full reference of the Research Output:

○ The manuscript is currently under review for publication – please indicate:

- The name of the journal:
- The percentage of the manuscript/published work that was contributed by the candidate:
- Describe the contribution that the candidate has made to the manuscript/published work:

● It is intended that the manuscript will be published, but it has not yet been submitted to a journal

Candidate's Signature:	Susav Pradhan Digitally signed by Susav Pradhan Date: 2021.06.09 13:06:00 +12'00'
Date:	09-Jun-2021
Primary Supervisor's Signature:	Williams, Martin Digitally signed by Williams, Martin Date: 2021.06.19 12:34:35 +12'00'
Date:	19-Jun-2021

This form should appear at the end of each thesis chapter/section/appendix submitted as a manuscript/publication or collected as an appendix at the end of the thesis.

GRS Version 5 – 13 December 2019
DRC 19/09/10

Bibliography

Alberts, Bruce (2008). "Molecular Biology of the Cell". In: *The Yale Journal of Biology and Medicine*. ISSN: 03011526. DOI: 10.1024/0301-1526.32.1.54.

Allan, D. B. et al. (2014). "Linear and nonlinear microrheology of lysozyme layers forming at the air-water interface". In: *Soft Matter* 10.36, pp. 7051–7060. ISSN: 1744-683X. DOI: 10.1039/c4sm00484a. URL: <GotoISI>://WOS:000341025700019.

Aoki, Takahira et al. (1997). "The pipette aspiration applied to the local stiffness measurement of soft tissues". In: *Annals of Biomedical Engineering*. ISSN: 00906964. DOI: 10.1007/BF02684197.

Arbore, Claudia et al. (2019). *Probing force in living cells with optical tweezers: from single-molecule mechanics to cell mechanotransduction*. DOI: 10.1007/s12551-019-00599-y.

Ashkin, A. (1992). "Forces of a single-beam gradient laser trap on a dielectric sphere in the ray optics regime". In: *Biophysical Journal*. ISSN: 00063495. DOI: 10.1016/S0006-3495(92)81860-X.

— (1999). "Optical Trapping and Manipulation of Neutral Particles Using Lasers". In: *Optics and Photonics News*. ISSN: 1047-6938. DOI: 10.1364/OPN.10.5.000041.

Bacabac, Rommel G. et al. (2008). "Round versus flat: Bone cell morphology, elasticity, and mechanosensing". In: *Journal of Biomechanics*. ISSN: 00219290. DOI: 10.1016/j.jbiomech.2008.01.031.

Balakrishnan, G., D. Durand, and T. Nicolai (2011). "Particle Diffusion in Globular Protein Gels in Relation to the Gel Structure". In: *Biomacromolecules* 12.2, pp. 450–456. ISSN: 1525-7797. DOI: 10.1021/bm101238r. URL: <GotoISI>://WOS:000287175700021.

Benmouna, F. and D. Johannsmann (2004). "Viscoelasticity of gelatin surfaces probed by AFM noise analysis". In: *Langmuir* 20.1, pp. 188–193. ISSN: 0743-7463. DOI: 10.1021/la0355794. URL: <GotoISI>://WOS:000187754400033.

Berg-Sørensen, Kirstine and Henrik Flyvbjerg (2004). “Power spectrum analysis for optical tweezers”. In: *Review of Scientific Instruments*. ISSN: 00346748. DOI: `10.1063/1.1645654`.

Blijdenstein, T. B. J. et al. (2003). “Control of strength and stability of emulsion gels by a combination of long- and short-range interactions”. In: *Langmuir* 19.17, pp. 6657–6663. ISSN: 0743-7463. DOI: `10.1021/la0342969`. URL: `<GotoISI>://WOS:000184768600019`.

Blijdenstein, T. B. J. et al. (2004). “Dextran-induced depletion flocculation in oil-in-water emulsions in the presence of sucrose”. In: *Food Hydrocolloids* 18.5, pp. 857–863. ISSN: 0268-005X. DOI: `10.1016/j.foodhyd.2004.01.003`. URL: `<GotoISI>://WOS:000222666200015`.

Bonilla, M. R. et al. (2015). “Interpreting atomic force microscopy nanoindentation of hierarchical biological materials using multi-regime analysis”. In: *Soft Matter*. ISSN: 17446848. DOI: `10.1039/c4sm02440k`.

“TWO - The structure of the cell membrane” (1970). In: *Division of Labor in Cells (Second Edition)*. Ed. by GEOFFREY H. Bourne. Second Edition. Academic Press, pp. 12 – 35. ISBN: 978-0-12-119259-4. DOI: `https://doi.org/10.1016/B978-0-12-119259-4.50006-6`. URL: `http://www.sciencedirect.com/science/article/pii/B9780121192594500066`.

Brasovs, A. et al. (2015). “Magnetic microrods as a tool for microrheology”. In: *Soft Matter* 11.13, pp. 2563–2569. ISSN: 1744-683X. DOI: `10.1039/c4sm02454k`. URL: `<GotoISI>://WOS:000351551800004`.

Bustin, Michael and Tom Misteli (2016). *Nongenetic functions of the genome*. DOI: `10.1126/science.aad6933`.

Caggioni, M. et al. (2007). “Rheology and microrheology of a microstructured fluid: The gellan gum case”. In: *Journal of Rheology* 51.5, pp. 851–865. ISSN: 0148-6055. DOI: `10.1122/1.2751385`. URL: `<GotoISI>://WOS:000249386300005`.

Campillo, Clément et al. (2013). “Unexpected membrane dynamics unveiled by membrane nanotube extrusion”. In: *Biophysical Journal*. ISSN: 15420086. DOI: `10.1016/j.bpj.2013.01.051`.

Chaikin P. M.; Lubensky, T. C. (1995). “Principles of condensed matter physics | |”. In: vol. 10.1017/CBO9780511813467. ISBN: 9780511813467. DOI: `10.1017/CBO9780511813467`. URL: `http://gen.lib.rus.ec/scimag/index.php?s=10.1017/CBO9780511813467`.

Chen, Jinju (2014). *Nanobiomechanics of living cells: A review*. DOI: `10.1098/rsfs.2013.0055`.

Cicuta, Pietro and Athene M. Donald (2007a). "Microrheology: a review of the method and applications". In: *Soft Matter*. ISSN: 1744-683X. DOI: `10.1039/b706004c`.

— (2007b). "Microrheology: A review of the method and applications". In: *Soft Matter*. ISSN: 17446848. DOI: `10.1039/b706004c`.

Coceano, Giovanna et al. (2015). "Investigation into local cell mechanics by atomic force microscopy mapping and optical tweezer vertical indentation". In: *Nanotechnology* 27.6, p. 065102.

Contreras, A, M C Gutierrez, and T K Hale (2010). "Differential Expression Patterns of the Heterochromatin Proteins HP1 alpha and HP1 beta in Different Tumor Types". In: *Modern Pathology* 23, 385A–385A.

Corrigan, A. M. and A. M. Donald (2009). "Passive Microrheology of Solvent-Induced Fibrillar Protein Networks". In: *Langmuir* 25.15, pp. 8599–8605. ISSN: 0743-7463. DOI: `10.1021/la804208q`. URL: `<GotoISI>://WOS:000268231500041`.

Crater, J. S. and R. L. Carrier (2010). "Barrier Properties of Gastrointestinal Mucus to Nanoparticle Transport". In: *Macromolecular Bioscience* 10.12, pp. 1473–1483. ISSN: 1616-5187. DOI: `10.1002/mabi.201000137`. URL: `<GotoISI>://WOS:000285313000010`.

Crocker, J. C. et al. (2000). "Two-point microrheology of inhomogeneous soft materials". In: *Physical Review Letters* 85.4, pp. 888–891. ISSN: 0031-9007. DOI: `10.1103/PhysRevLett.85.888`. URL: `<GotoISI>://WOS:000088311800052`.

Crocker, John C. and David G. Grier (1996). "Methods of digital video microscopy for colloidal studies". In: *Journal of Colloid and Interface Science*. ISSN: 00219797. DOI: `10.1006/jcis.1996.0217`.

Cucheval, Aurélie S.B. et al. (2009). "Multiple particle tracking investigations of acid milk gels using tracer particles with designed surface chemistries and comparison with diffusing wave spectroscopy studies". In: *Langmuir*. ISSN: 07437463. DOI: `10.1021/la901424w`.

Dahl, K N et al. (2005). "Power-law rheology of isolated nuclei with deformation mapping of nuclear substructures". eng. In: *Biophys J* 89.4, pp. 2855–2864. DOI: `10.1529/biophysj.105.062554`. URL: `http://www.ncbi.nlm.nih.gov/pubmed/16055543`.

Dahl, Kris Noel, Alexandre J.S. Ribeiro, and Jan Lammerding (2008). *Nuclear shape, mechanics, and mechanotransduction*. DOI: 10.1161/CIRCRESAHA.108.173989.

Dahl, Kris Noel et al. (2004). "The nuclear envelope lamina network has elasticity and a compressibility limit suggestive of a molecular shock absorber". In: *Journal of cell science* 117.20, pp. 4779–4786.

Dai, Jianwu and Michael P. Sheetz (Jan. 1997). "Chapter 9 Cell Membrane Mechanics". In: *Methods in Cell Biology* 55.C, pp. 157–171. ISSN: 0091679X. DOI: 10.1016/S0091-679X(08)60407-0.

— (1999). "Membrane tether formation from blebbing cells". In: *Biophysical Journal*. ISSN: 00063495. DOI: 10.1016/S0006-3495(99)77168-7.

Dasgupta, B R et al. (2002). "Microrheology of polyethylene oxide using diffusing wave spectroscopy and single scattering". In: *Phys Rev E Stat Nonlin Soft Matter Phys*. ISSN: 1063-651X. DOI: 10.1103/PhysRevE.65.051505.

Datar, Anagha et al. (2015). "Dynamics of membrane tethers reveal novel aspects of cytoskeleton-membrane interactions in axons". In: *Biophysical Journal*. ISSN: 15420086. DOI: 10.1016/j.bpj.2014.11.3480.

Dechat, T et al. (2008). "Nuclear lamins: major factors in the structural organization and function of the nucleus and chromatin". In: *Genes Dev* 22.7, pp. 832–853. DOI: 10.1101/gad.1652708. URL: https://www.ncbi.nlm.nih.gov/pubmed/18381888.

Deguchi, Shinji et al. (2005). "Flow-induced hardening of endothelial nucleus as an intracellular stress-bearing organelle". In: *Journal of Biomechanics*. ISSN: 00219290. DOI: 10.1016/j.jbiomech.2005.06.003.

Denais, Celine and Jan Lammerding (2014). "Nuclear mechanics in cancer". In: *Advances in Experimental Medicine and Biology*. ISSN: 00652598. DOI: 10.1007/978-1-4899-8032-8{_}20.

Drury, Jeanie L. and Micah Dembo (1999). "Hydrodynamics of micropipette aspiration". In: *Biophysical Journal*. ISSN: 00063495. DOI: 10.1016/S0006-3495(99)77183-3.

Dubey, Sushil et al. (2020). "The axonal actin-spectrin lattice acts as a tension buffering shock absorber". In: *eLife*. ISSN: 2050084X. DOI: 10.7554/eLife.51772.

Dufrêne, Y. F. (2001). *Application of atomic force microscopy to microbial surfaces: From reconstituted cell surface layers to living cells*. DOI: 10.1016/S0968-4328(99)00106-7.

Dufresne, Eric R. and David G. Grier (1998). “Optical tweezer arrays and optical substrates created with diffractive optics”. In: *Review of Scientific Instruments*. ISSN: 00346748. DOI: 10.1063/1.1148883.

Eliot, C., D. S. Horne, and E. Dickinson (2005). “Understanding temperature-sensitive caseinate emulsions: new information from diffusing wave spectroscopy”. In: *Food Hydrocolloids* 19.2, pp. 279–287. ISSN: 0268-005X. DOI: 10.1016/j.foodhyd.2004.06.005. URL: <GotoISI>://WOS:000225867300011.

Evans, E. and A. Yeung (1994). “Hidden dynamics in rapid changes of bilayer shape”. In: *Chemistry and Physics of Lipids*. ISSN: 00093084. DOI: 10.1016/0009-3084(94)90173-2.

Falleroni, Fabio, Vincent Torre, and Dan Cojoc (2018). “Cell mechanotransduction with piconewton forces applied by optical tweezers”. In: *Frontiers in Cellular Neuroscience*. ISSN: 16625102. DOI: 10.3389/fncel.2018.00130.

Fischer, Mario and Kirstine Berg-Sørensen (2007). “Calibration of trapping force and response function of optical tweezers in viscoelastic media”. In: *Journal of Optics A: Pure and Applied Optics*. ISSN: 14644258. DOI: 10.1088/1464-4258/9/8/S18.

Fischer, Mario et al. (2010). *Active-passive calibration of optical tweezers in viscoelastic media*. DOI: 10.1063/1.3280222.

Fischer-Cripps, A. C. (1999). “The Hertzian contact surface”. In: *Journal of Materials Science*. ISSN: 00222461. DOI: 10.1023/A:1004490230078.

Furusawa, T et al. (2015). “Chromatin decompaction by the nucleosomal binding protein HMGN5 impairs nuclear sturdiness”. In: *Nat Commun* 6, p. 6138. DOI: 10.1038/ncomms7138. URL: https://www.ncbi.nlm.nih.gov/pubmed/25609380.

G, G. F.F. (1896). “Hertz’s miscellaneous papers”. In: *Nature*. ISSN: 00280836. DOI: 10.1038/055006f0.

Gangotra, Ankita (2019). *Microaspiration: Development Applications - A Tool to Study the Mechanical Properties of Soft Particles*. URL: https://researchspace.auckland.ac.nz/handle/2292/49238.

Gangotra, Ankita and Geoff R Willmott (2019). “Mechanical properties of bovine erythrocytes derived from ion current measurements using micropipettes”. In: *Bioelectrochemistry* 128, pp. 204–210.

Grewal, S I and S Jia (2007). "Heterochromatin revisited". In: *Nat Rev Genet* 8.1, pp. 35–46. URL: `http://www.ncbi.nlm.nih.gov/entrez/query.fcgi?cmd=Retrieve&db=PubMed&dopt=Citation&list_uids=17173056`.

Griffiths, M. R. et al. (2016). "Measuring the interaction between a pair of emulsion droplets using dual-trap optical tweezers". In: *Rsc Advances* 6.18, pp. 14538–14546. ISSN: 2046-2069. DOI: `10.1039/c5ra25073k`. URL: `<GotoISI>://WOS:000369658100015`.

Guck, Jochen et al. (2001). "The optical stretcher: A novel laser tool to micromanipulate cells". In: *Biophysical Journal*. ISSN: 00063495. DOI: `10.1016/S0006-3495(01)75740-2`.

Guevorkian, Karine et al. (2010). "Aspiration of biological viscoelastic drops". In: *Physical Review Letters* 104.21, p. 218101.

Guilak, Farshid, John R. Tedrow, and Rainer Burgkart (2000). "Viscoelastic properties of the cell nucleus". In: *Biochemical and Biophysical Research Communications*. ISSN: 0006291X. DOI: `10.1006/bbrc.2000.2360`.

Guz, Nataliia et al. (2014). "If Cell Mechanics Can Be Described by Elastic Modulus: Study of Different Models and Probes Used in Indentation Experiments". In: *Biophysical Journal*. ISSN: 15420086. DOI: `10.1016/j.bpj.2014.06.033`.

Hansma, PK et al. (1989). "The scanning ion-conductance microscope". In: *Science* 243.4891, pp. 641–643.

Harr, J C et al. (2015). "Directed targeting of chromatin to the nuclear lamina is mediated by chromatin state and A-type lamins". In: *J Cell Biol* 208.1, pp. 33–52. DOI: `10.1083/jcb.201405110`. URL: `https://www.ncbi.nlm.nih.gov/pubmed/25559185`.

Hayashi, Kozaburo and Mayumi Iwata (2015). "Stiffness of cancer cells measured with an AFM indentation method". In: *Journal of the Mechanical Behavior of Biomedical Materials*. ISSN: 18780180. DOI: `10.1016/j.jmbbm.2015.04.030`.

Hertz, Heinrich (1882). "Ueber die Berührung fester elastischer Körper". In: *Journal fur die Reine und Angewandte Mathematik*. ISSN: 14355345. DOI: `10.1515/crll.1882.92.156`.

Higgins, M. J. et al. (2006). "Noninvasive determination of optical lever sensitivity in atomic force microscopy". In: *Review of Scientific Instruments*. ISSN: 00346748. DOI: `10.1063/1.2162455`.

Hobson, Chad M et al. (2020). "Correlating nuclear morphology and external force with combined atomic force microscopy and light sheet imaging separates roles of chromatin and lamin A/C in nuclear mechanics". In: *Molecular biology of the cell* 31.16, pp. 1788–1801.

Hochmuth, Robert M (2000). "Micropipette aspiration of living cells". In: *Journal of biomechanics* 33.1, pp. 15–22.

Hochmuth, Robert M. et al. (1996). "Deformation and flow of membrane into tethers extracted from neuronal growth cones". In: *Biophysical Journal*. ISSN: 00063495. DOI: `10.1016/S0006-3495(96)79577-2`.

Holaska, J M, K L Wilson, and M Mansharamani (2002). "The nuclear envelope, lamins and nuclear assembly". In: *Curr Opin Cell Biol* 14.3, pp. 357–364. DOI: `10.1016/s0955-0674(02)00329-0`. URL: `https://www.ncbi.nlm.nih.gov/pubmed/12067659`.

Hu, Jingjie et al. (2018). "An investigation of the viscoelastic properties and the actin cytoskeletal structure of triple negative breast cancer cells". In: *Journal of the Mechanical Behavior of Biomedical Materials*. ISSN: 18780180. DOI: `10.1016/j.jmbbm.2018.05.038`.

Huang, Feiran et al. (2013). "Real-time particle tracking for studying intracellular trafficking of pharmaceutical nanocarriers". In: *Methods in Molecular Biology*. ISSN: 10643745. DOI: `10.1007/978-1-62703-336-7{\_}20`.

Huang, S. L. et al. (2016). "Microgels at the Water/Oil Interface: In Situ Observation of Structural Aging and Two-Dimensional Magnetic Bead Microrheology". In: *Langmuir* 32.3, pp. 712–722. ISSN: 0743-7463. DOI: `10.1021/acs.langmuir.5b01438`. URL: `<GotoISI>://WOS:000368950600009`.

Ito, Hiroaki and Makoto Kaneko (2020). *On-chip cell manipulation and applications to deformability measurements*. DOI: `10.1186/s40648-020-0154-x`.

Janssen, A, S U Colmenares, and G H Karpen (2018). "Heterochromatin: Guardian of the Genome". In: *Annu Rev Cell Devel Biol* 34, pp. 265–288. DOI: `10.1146/annurev-cellbio-100617-062653`. URL: `https://www.ncbi.nlm.nih.gov/pubmed/30044650`.

Jiménez-Flores, Rafael et al. (2010). “Characterization of lactobacillus reuteri interaction with milk fat globule membrane components in dairy products”. In: *Journal of Agricultural and Food Chemistry*. ISSN: 00218561. DOI: 10.1021/jf904381s.

Jordens, S. et al. (2014). “Bridging the Gap between the Nanostructural Organization and Macroscopic Interfacial Rheology of Amyloid Fibrils at Liquid Interfaces”. In: *Langmuir* 30.33, pp. 10090–10097. ISSN: 0743-7463. DOI: 10.1021/la5020658. URL: <GotoISI>://WOS:000340993200027.

Kamble, Harshad et al. (2016). *Cell stretching devices as research tools: Engineering and biological considerations*. DOI: 10.1039/c6lc00607h.

Kapoor, P, B D Lavoie, and L Frappier (2005). “EBP2 plays a key role in Epstein-Barr virus mitotic segregation and is regulated by aurora family kinases”. In: *Mol Cell Biol* 25.12, pp. 4934–4945. DOI: 10.1128/MCB.25.12.4934-4945.2005. URL: https://www.ncbi.nlm.nih.gov/pubmed/15923612.

Katira, Parag, Roger T. Bonnecaze, and Muhammad H. Zaman (2013). “Modeling the Mechanics of Cancer: Effect of Changes in Cellular and Extra-Cellular Mechanical Properties”. In: *Frontiers in Oncology*. ISSN: 2234-943X. DOI: 10.3389/fonc.2013.00145.

Khalili, Amelia Ahmad and Mohd Ridzuan Ahmad (2015). *A Review of cell adhesion studies for biomedical and biological applications*. DOI: 10.3390/ijms160818149.

Khatau, Shyam B. et al. (2012). “The distinct roles of the nucleus and nucleus-cytoskeleton connections in three-dimensional cell migration”. In: *Scientific Reports*. ISSN: 20452322. DOI: 10.1038/srep00488.

Kind, Jop et al. (2013). “Single-cell dynamics of genome-nuclear lamina interactions”. In: *Cell*. ISSN: 00928674. DOI: 10.1016/j.cell.2013.02.028.

Kirch, J. et al. (2012). “Optical tweezers reveal relationship between microstructure and nanoparticle penetration of pulmonary mucus”. In: *Proceedings of the National Academy of Sciences of the United States of America* 109.45, pp. 18355–18360. ISSN: 0027-8424. DOI: 10.1073/pnas.1214066109. URL: <GotoISI>://WOS:000311156700035.

Kirschmann, D A et al. (2000). “Down-regulation of HP1Hsalpha expression is associated with the metastatic phenotype in breast cancer”. In: *Cancer Res* 60.13, pp. 3359–3363. URL: http://www.ncbi.nlm.nih.gov/entrez/query.fcgi?cmd=Retrieve&db=PubMed&dopt=Citation&list_uids=10910038.

Kochin, Vitaly et al. (2014). "Interphase phosphorylation of lamin A". In: *Journal of Cell Science*. ISSN: 14779137. DOI: 10.1242/jcs.141820.

Kosmerl, Erica et al. (2021). *Improving human health with milk fat globule membrane, lactic acid bacteria, and bifidobacteria*. DOI: 10.3390/microorganisms9020341.

Kourmouli, N et al. (2001). "Binding of heterochromatin protein 1 to the nuclear envelope is regulated by a soluble form of tubulin". In: *J Biol Chem* 276.16, pp. 13007–13014. DOI: 10.1074/jbc.M007135200. URL: https://www.ncbi.nlm.nih.gov/pubmed/11278332.

Kumar, Y, D Sengupta, and W Bickmore (2020). "Recent advances in the spatial organization of the mammalian genome". In: *J Biosci* 45. URL: https://www.ncbi.nlm.nih.gov/pubmed/31965996.

Lai, S. K. et al. (2009). "Micro- and macrorheology of mucus". In: *Advanced Drug Delivery Reviews* 61.2, pp. 86–100. ISSN: 0169-409X. DOI: 10.1016/j.addr.2008.09.012. URL: <GotoISI>://WOS:000264451100003.

Lammerding, J et al. (2006). "Lamins A and C but not lamin B1 regulate nuclear mechanics". In: *J Biol Chem* 281.35, pp. 25768–25780. DOI: 10.1074/jbc.M513511200. URL: https://www.ncbi.nlm.nih.gov/pubmed/16825190.

Larson, R G (1999). *The Structure and Rheology of Complex Fluids*. ISBN: 019512197X. DOI: 10.1029/2006EO230009.

Lee, M. H. et al. (2010). "Combined Passive and Active Microrheology Study of Protein-Layer Formation at an Air-Water Interface". In: *Langmuir* 26.4, pp. 2650–2658. ISSN: 0743-7463. DOI: 10.1021/la902881f. URL: <GotoISI>://WOS:000274342200069.

Lee, M. H. et al. (2011). "Brownian dynamics of colloidal probes during protein-layer formation at an oil-water interface". In: *Soft Matter* 7.17, pp. 7635–7642. ISSN: 1744-683X. DOI: 10.1039/c1sm05235g. URL: <GotoISI>://WOS:000294014200007.

Levenson, Anait S. and V. Craig Jordan (1997). *MCF-7: The first hormone-responsive breast cancer cell line*.

Li, Qingsen and Chwee Teck Lim (2010). "Structure–Mechanical Property Changes in Nucleus arising from Breast Cancer". In: DOI: 10.1007/8415{_}2010{_}19.

Liu, F. G. et al. (2016). "Utilization of interfacial engineering to improve physicochemical stability of beta-carotene emulsions: Multilayer coatings formed using protein and protein-polyphenol conjugates". In: *Food Chemistry* 205, pp. 129–139. ISSN:

0308-8146. DOI: 10.1016/j.foodchem.2016.02.155. URL: <GotoISI>://WOS:000372355000018.

Loosemore, Victoria E. and Nancy R. Forde (2017). "Effects of finite and discrete sampling and blur on microrheology experiments". In: *Opt. Express* 25.25, pp. 31239–31252. DOI: 10.1364/OE.25.031239. URL: http://www.opticsexpress.org/abstract.cfm?URI=oe-25-25-31239.

Macierzanka, A. et al. (2012). "Enzymatically Structured Emulsions in Simulated Gastrointestinal Environment: Impact on Interfacial Proteolysis and Diffusion in Intestinal Mucus". In: *Langmuir* 28.50, pp. 17349–17362. ISSN: 0743-7463. DOI: 10.1021/la302194q. URL: <GotoISI>://WOS:000312434200016.

MacKintosh, F.C. C and C.F. F Schmidt (1999). "Microrheology". In: *Current Opinion in Colloid & Interface Science*. ISSN: 13590294. DOI: 10.1016/S1359-0294(99)90010-9.

Maniotis, Andrew J., Christopher S. Chen, and Donald E. Ingber (1997). "Demonstration of mechanical connections between integrins, cytoskeletal filaments, and nucleoplasm that stabilize nuclear structure". In: *Proceedings of the National Academy of Sciences of the United States of America*. ISSN: 00278424. DOI: 10.1073/pnas.94.3.849.

Mas, Josep et al. (2013). "Quantitative determination of optical trapping strength and viscoelastic moduli inside living cells". In: *Physical Biology*. ISSN: 14783967. DOI: 10.1088/1478-3975/10/4/046006.

Mason, T. G. (2000). "Estimating the viscoelastic moduli of complex fluids using the generalized Stokes-Einstein equation". In: *Rheologica Acta*. ISSN: 00354511. DOI: 10.1007/s003970000094.

Mason, T. G. and D. A. Weitz (1995). "Optical measurements of frequency-dependent linear viscoelastic moduli of complex fluids". In: *Physical Review Letters*. ISSN: 00319007. DOI: 10.1103/PhysRevLett.74.1250.

Moeendarbary, Emad and Andrew R. Harris (2014). "Cell mechanics: Principles, practices, and prospects". In: *Wiley Interdisciplinary Reviews: Systems Biology and Medicine*. ISSN: 1939005X. DOI: 10.1002/wsbm.1275.

Moschakis, T., A. Lazaridou, and C. G. Biliaderis (2012). "Using particle tracking to probe the local dynamics of barley beta-glucan solutions upon gelation". In: *Journal* *of Colloid and Interface Science* 375, pp. 50–59. ISSN: 0021-9797. DOI: `10.1016/j.jcis.2012.02.048`. URL: `<GotoISI>://WOS:000302760900007`.

Moschakis, Thomas, Brent S. Murray, and Eric Dickinson (2006). "Particle tracking using confocal microscopy to probe the microrheology in a phase-separating emulsion containing nonadsorbing polysaccharide". In: *Langmuir*. ISSN: 07437463. DOI: `10.1021/la0533258`.

— (2010). "On the kinetics of acid sodium caseinate gelation using particle tracking to probe the microrheology". In: *Journal of Colloid and Interface Science*. ISSN: 00219797. DOI: `10.1016/j.jcis.2010.02.005`.

Müller, Daniel J. et al. (2020). *Atomic Force Microscopy-Based Force Spectroscopy and Multiparametric Imaging of Biomolecular and Cellular Systems*. DOI: `10.1021/acs.chemrev.0c00617`.

Narita, T. et al. (2001). "Microrheology of poly(vinyl alcohol) aqueous solutions and chemically cross-linked gels". In: *Macromolecules* 34.23, pp. 8224–8231. ISSN: 0024-9297. DOI: `10.1021/ma010890i`. URL: `<GotoISI>://WOS:000171981500042`.

Nawaz, Schanila et al. (2012). "Cell Visco-Elasticity Measured with AFM and Optical Trapping at Sub-Micrometer Deformations". In: *PLoS ONE*. ISSN: 19326203. DOI: `10.1371/journal.pone.0045297`.

Needham, D. and R. M. Hochmuth (1990). "Rapid flow of passive neutrophils into a 4 μm pipet and measurement of cytoplasmic viscosity". In: *Journal of Biomechanical Engineering*. ISSN: 15288951. DOI: `10.1115/1.2891184`.

Neuman, Keir C. and Steven M. Block (2004). *Optical trapping*. DOI: `10.1063/1.1785844`.

Norwood, L E et al. (2006). "A requirement for dimerization of HP1Hsalpha in suppression of breast cancer invasion". eng. In: *J Biol Chem* 281.27, pp. 18668–18676. URL: `http://www.ncbi.nlm.nih.gov/entrez/query.fcgi?cmd=Retrieve&db=PubMed&dopt=Citation&list_uids=16648629`.

Pajerowski, J D et al. (2007). "Physical plasticity of the nucleus in stem cell differentiation". eng. In: *Proceedings of the National Academy of Sciences of the United States of America* 104.40, pp. 15619–15624. DOI: `10.1073/pnas.0702576104`. URL: `http://www.ncbi.nlm.nih.gov/pubmed/17893336`.

Peterman, Erwin J.G., Frederick Gittes, and Christoph F. Schmidt (2003). "Laser-induced heating in optical traps". In: *Biophysical Journal*. ISSN: 00063495. DOI: 10.1016/S0006-3495(03)74946-7.

Pimenta-Lopes, Carolina et al. (2019). "Concurrent atomic force spectroscopy". In: *Communications Physics*. ISSN: 23993650. DOI: 10.1038/s42005-019-0192-y.

Poleshko, A et al. (2013). "The human protein PRR14 tethers heterochromatin to the nuclear lamina during interphase and mitotic exit". eng. In: *Cell reports* 5.2, pp. 292–301. DOI: 10.1016/j.celrep.2013.09.024. URL: http://www.ncbi.nlm.nih.gov/pubmed/24209742.

Polioudaki, H et al. (2001). "Histones H3/H4 form a tight complex with the inner nuclear membrane protein LBR and heterochromatin protein 1". In: *EMBO Rep* 2.10, pp. 920–925. URL: http://www.ncbi.nlm.nih.gov/entrez/query.fcgi?cmd=Retrieve&db=PubMed&dopt=Citation&list_uids=11571267.

Pombo, A and N Dillon (2015). "Three-dimensional genome architecture: players and mechanisms". In: *Nat Rev Mol Cell Biol* 16.4, pp. 245–257. DOI: 10.1038/nrm3965. URL: https://www.ncbi.nlm.nih.gov/pubmed/25757416.

Popov, Valentin L (2017). *Contact Mechanics and Friction - Hertz force*. ISBN: 978-3-642-10802-0.

Pradhan, Whitby, and Williams (Jan. 2018). "Applications of Microrheology to Food Systems". In:

Puig-De-Morales, Marina et al. (2001). "Measurement of cell microrheology by magnetic twisting cytometry with frequency domain demodulation". In: *Journal of Applied Physiology*. ISSN: 87507587. DOI: 10.1152/jappl.2001.91.3.1152.

Rasband, W.S. (2014). *ImageJ, U.S. National Institutes of Health, Bethesda, Maryland, USA*.

Raucher, Drazen and Michael P. Sheetz (1999). "Characteristics of a membrane reservoir buffering membrane tension". In: *Biophysical Journal*. ISSN: 00063495. DOI: 10.1016/S0006-3495(99)77040-2.

Rogers, Salman S et al. (2007). "Precise particle tracking against a complicated background: polynomial fitting with Gaussian weight". In: *Physical Biology* 4.3, p. 220. URL: http://stacks.iop.org/1478-3975/4/i=3/a=008.

Rowat, A. C. et al. (2005). "Characterization of the elastic properties of the nuclear envelope". In: *Journal of the Royal Society Interface*. ISSN: 17425662. DOI: `10.1098/rsif.2004.0022`.

Ryan, D P and D J Tremethick (2018). "The interplay between H2A.Z and H3K9 methylation in regulating HP1alpha binding to linker histone-containing chromatin". In: *Nucleic Acids Res* 46.18, pp. 9353–9366. DOI: `10.1093/nar/gky632`. URL: `https://www.ncbi.nlm.nih.gov/pubmed/30007360`.

Segur, J. B. and Helen E. Oderstar (1951). "Viscosity of Glycerol and Its Aqueous Solutions". In: *Industrial and Engineering Chemistry*. ISSN: 00197866. DOI: `10.1021/ie50501a040`.

Sengupta, Ranjita et al. (2015). "Lactobacillus fermentum AGR1487 cell surface structures and supernatant increase paracellular permeability through different pathways". In: *MicrobiologyOpen*. ISSN: 20458827. DOI: `10.1002/mbo3.260`.

Shayegan, M. and N. R. Forde (2014). "Microrheological Characterization of Collagen Systems: From Molecular Solutions to Fibrillar Gels (vol 8, e70590, 2013)". In: *Plos One* 9.7. ISSN: 1932-6203. DOI: `10.1371/journal.pone.0102938`. URL: `<GotoISI>://WOS:000339418300109`.

Shimi, T et al. (2008). "The A- and B-type nuclear lamin networks: microdomains involved in chromatin organization and transcription". In: *Genes Dev* 22.24, pp. 3409–3421. DOI: `10.1101/gad.1735208`. URL: `https://www.ncbi.nlm.nih.gov/pubmed/19141474`.

Shojaei-Baghini, Ehsan, Yi Zheng, and Yu Sun (2013). "Automated micropipette aspiration of single cells". In: *Annals of Biomedical Engineering*. ISSN: 00906964. DOI: `10.1007/s10439-013-0791-9`.

Smith, Benjamin A. et al. (2005). "Probing the viscoelastic behavior of cultured airway smooth muscle cells with atomic force microscopy: Stiffening induced by contractile agonist". In: *Biophysical Journal*. ISSN: 00063495. DOI: `10.1529/biophysj.104.046649`.

Solovei, I et al. (2013). "LBR and lamin A/C sequentially tether peripheral heterochromatin and inversely regulate differentiation". eng. In: *Cell* 152.3, pp. 584–598. DOI: `10.1016/j.cell.2013.01.009`. URL: `http://www.ncbi.nlm.nih.gov/pubmed/23374351`.

Stephens, A D et al. (2017a). “Chromatin and lamin A determine two different mechanical response regimes of the cell nucleus”. In: *Mol Biol Cell* 28.14, pp. 1984–1996. DOI: `10.1091/mbc.E16-09-0653`. URL: `https://www.ncbi.nlm.nih.gov/pubmed/28057760`.

Stephens, A D et al. (2018). “Chromatin histone modifications and rigidity affect nuclear morphology independent of lamins”. In: *Mol Biol Cell* 29.2, pp. 220–233. DOI: `10.1091/mbc.E17-06-0410`. URL: `https://www.ncbi.nlm.nih.gov/pubmed/29142071`.

Stephens, Andrew D et al. (2017b). “Chromatin and lamin A determine two different mechanical response regimes of the cell nucleus”. In: *Molecular biology of the cell* 28.14, pp. 1984–1996.

Suresh, Subra (2007). “Biomechanics and biophysics of cancer cells”. In: *Acta Materialia*. ISSN: 13596454. DOI: `10.1016/j.actamat.2007.04.022`.

Swift, J et al. (2013). “Nuclear lamin-A scales with tissue stiffness and enhances matrix-directed differentiation”. In: *Science* 341.6149, p. 1240104. DOI: `10.1126/science.1240104`. URL: `https://www.ncbi.nlm.nih.gov/pubmed/23990565`.

Tassieri, M. (2016). *Microrheology with optical tweezers: Principles and applications*. ISBN: 9789814669191. DOI: `10.4032/9789814669191`.

Torre, Lindsey A. et al. (2015). “Global cancer statistics, 2012”. In: *CA: A Cancer Journal for Clinicians*. ISSN: 1542-4863. DOI: `10.3322/caac.21262`.

Tretiakova, M S et al. (2014). “Heterochromatin protein 1 expression is reduced in human thyroid malignancy”. eng. In: *Laboratory investigation; a journal of technical methods and pathology* 94.7, pp. 788–795. DOI: `10.1038/labinvest.2014.68`. URL: `http://www.ncbi.nlm.nih.gov/pubmed/24840329`.

Unal, Mustafa et al. (2014). *Micro and Nano-Scale Technologies for Cell Mechanics*. DOI: `10.5772/59379`.

Valentine, M. T., L. E. Dewalt, and H. D. Ou-Yang (1996). “Forces on a colloidal particle in a polymer solution: A study using optical tweezers”. In: *Journal of Physics Condensed Matter*. ISSN: 09538984. DOI: `10.1088/0953-8984/8/47/048`.

Van Vliet, K. J., G. Bao, and S. Suresh (2003). “The biomechanics toolbox: Experimental approaches for living cells and biomolecules”. In: *Acta Materialia*. ISSN: 13596454. DOI: `10.1016/j.actamat.2003.09.001`.

Vanapalli, Siva A., Michel H.G. Duits, and Frieder Mugele (2009). "Microfluidics as a functional tool for cell mechanics". In: *Biomicrofluidics*. DOI: `10.1063/1.3067820`.

Vaziri, A., H. Lee, and M. R. Kaazempur Mofrad (2006). "Deformation of the cell nucleus under indentation: Mechanics and mechanisms". In: *Journal of Materials Research*. ISSN: 08842914. DOI: `10.1557/jmr.2006.0262`.

Vaziri, Ashkan and Mohammad R Kaazempur Mofrad (2007). "Mechanics and deformation of the nucleus in micropipette aspiration experiment". In: *Journal of biomechanics* 40.9, pp. 2053–2062.

Velegol, D. and F. Lanni (2001a). "Cell traction forces on soft biomaterials. I. Microrheology of Type I collagen gels". In: *Biophysical Journal* 81.3, pp. 1786–1792. ISSN: 0006-3495. URL: `<GotoISI>://WOS:000170600800051`.

Velegol, Darrell and Frederick Lanni (2001b). "Cell traction forces on soft biomaterials. I. Microrheology of Type I collagen gels". In: *Biophysical Journal*. ISSN: 00063495. DOI: `10.1016/S0006-3495(01)75829-8`.

Verstraeten, Valerie L.R.M. and Jan Lammerding (2008). "Experimental techniques for study of chromatin mechanics in intact nuclei and living cells". In: *Chromosome Research*. ISSN: 09673849. DOI: `10.1007/s10577-008-1232-8`.

Vincent, R. R. et al. (2007). "Microrheological studies reveal semiflexible networks in gels of a ubiquitous cell wall polysaccharide". In: *Physical Review E* 76.3. ISSN: 1539-3755. DOI: `10.1103/PhysRevE.76.031909`. URL: `<GotoISI>://WOS:000249785800089`.

Vinogradova, Olga I. et al. (2001). "Dynamic effects on force measurements. I. Viscous drag on the atomic force microscope cantilever". In: *Review of Scientific Instruments*. ISSN: 00346748. DOI: `10.1063/1.1366630`.

Waigh, T. A. (2005a). "Microrheology of complex fluids". In: *Reports on Progress in Physics*. ISSN: 00344885. DOI: `10.1088/0034-4885/68/3/R04`.

Waigh, T A (2005b). "Microrheology of complex fluids". In: *Reports on Progress in Physics* 68.3, p. 685. URL: `http://stacks.iop.org/0034-4885/68/i=3/a=R04`.

Waugh, R. and E. A. Evans (1979). "Thermoelasticity of red blood cell membrane". In: *Biophysical Journal*. ISSN: 00063495. DOI: `10.1016/S0006-3495(79)85239-X`.

Wilking, J. N. and T. G. Mason (2008). "Optically driven nonlinear microrheology of gelatin". In: *Physical Review E* 77.5. ISSN: 1539-3755. DOI: `10.1103/PhysRevE.77.055101`. URL: `<GotoISI>://WOS:000256885500001`.

Wu, Pei Hsun et al. (2018). "A comparison of methods to assess cell mechanical properties". In: *Nature Methods*. ISSN: 15487105. DOI: 10.1038/s41592-018-0015-1.

Xu, D. X. et al. (2016). "Physicochemical stability, microrheological properties and microstructure of lutein emulsions stabilized by multilayer membranes consisting of whey protein isolate, flaxseed gum and chitosan". In: *Food Chemistry* 202, pp. 156–164. ISSN: 0308-8146. DOI: 10.1016/j.foodchem.2016.01.052. URL: <GotoISI>://WOS:000370810000022.

Xu, J. Y. et al. (2002). "Microheterogeneity and microrheology of wheat gliadin suspensions studied by multiple-particle tracking". In: *Biomacromolecules* 3.1, pp. 92–99. ISSN: 1525-7797. DOI: 10.1021/bm015586b. URL: <GotoISI>://WOS:000174256500013.

Xu, Wenwei et al. (2012). "Cell Stiffness Is a Biomarker of the Metastatic Potential of Ovarian Cancer Cells". In: *PLoS ONE*. ISSN: 19326203. DOI: 10.1371/journal.pone.0046609.

Yakubov, Gleb E. et al. (2016). "Mapping nano-scale mechanical heterogeneity of primary plant cell walls". In: *Journal of Experimental Botany*. ISSN: 14602431. DOI: 10.1093/jxb/erw117.

Yang, Tie, Francesca Bragheri, and Paolo Minzioni (2016). "A comprehensive review of optical stretcher for cell mechanical characterization at single-cell level". In: *Micromachines*. ISSN: 2072666X. DOI: 10.3390/mi7050090.

Yeom, Eunseop, Yang Jun Kang, and Sang Joon Lee (2014). "Changes in velocity profile according to blood viscosity in a microchannel". In: *Biomicrofluidics*. ISSN: 19321058. DOI: 10.1063/1.4883275.

Yousafzai, Muhammad S. et al. (2016). "Substrate-dependent cell elasticity measured by optical tweezers indentation". In: *Optics and Lasers in Engineering*. ISSN: 01438166. DOI: 10.1016/j.optlaseng.2015.02.008.

Zhang, Lili et al. (2020). "Milk Fat Globule Membrane Protects Lactobacillus rhamnosus GG from Bile Stress by Regulating Exopolysaccharide Production and Biofilm Formation". In: *Journal of Agricultural and Food Chemistry*. ISSN: 15205118. DOI: 10.1021/acs.jafc.0c02267.

Zhang, Yuejin et al. (2017). "Interfacing 3D magnetic twisting cytometry with confocal fluorescence microscopy to image force responses in living cells". In: *Nature Protocols*. ISSN: 17502799. DOI: 10.1038/nprot.2017.042.

Zhou, Z. L. et al. (2014). "Accurate measurement of stiffness of leukemia cells and leukocytes using an optical trap by a rate-jump method". In: *RSC Advances*. ISSN: 20462069. DOI: `10.1039/c3ra45835k`.